Quantum magnetic imaging for DNA biophysical measurements

Zeeshawn Kazi

A dissertation
submitted in partial fulfillment of the
requirements for the degree of

Doctor of Philosophy

University of Washington

2023

Reading Committee:

Kai-Mei Fu, Chair

Paul Wiggins

Samu Taulu

Program Authorized to Offer Degree:
Physics

University of Washington

Abstract

Quantum magnetic imaging for DNA biophysical measurements

Zeeshawn Kazi

Chair of the Supervisory Committee:
Kai-Mei Fu
Departments of Physics & Electrical and Computer Engineering

An outstanding challenge in biophysics is sensing the relative bio-mechanical orientation of single-molecule biological systems. Prior approaches used to study single-molecule biophysics rely on attaching fluorescent or otherwise optically detectable probes to bio-mechanical systems, and inferring the underlying bio-dynamics from the imaged position of the probe. This approach is limited as distinct bio-mechanical configurations may result in the same imaged position dependence of the probe. Additionally, if a flourescent probe is chosen, measurements can only be performed for time scales on the order of seconds due to photobleaching. In this thesis, a new imaging modality is developed that relies on ferromagnetic probes of bio-mechanical orientation. Because a ferromagnet has an unchanging magnetic moment, imaging the re-orientation of a ferromagnetic probe attached to a single-molecule bio-mechanical system can directly provide information about bio-mechanical orientation. Additionally, a ferromagnetic probe will never photobleach, enabling long-time scale orientation tracking.

A high-sensitivity magnetic imaging platform based on the diamond nitrogen-vacancy (NV) center is developed to image the ferromagnetic probe moment direction. The NV center is a quantum defect whose electron spin has long spin coherence times, spin-coupled optical transitions and is photostable, allowing for optical probing of the ground state spin transitions, which couple strongly to external fields including magnetic field. Additionally, NV sensors can be fabricated near the surface of the biocompatible solid-state diamond host

material, and can operate at room temperature under ambient conditions.

This thesis details significant progress in the application of the diamond NV quantum sensor to study single-molecule DNA bio-mechanical orientation. A wide-field vector magnetic field imaging platform based on a near-surface ensemble of diamond NV defects is constructed. This wide-field magnetic imager enables nanotesla scale magnetic sensitivity with optical-diffraction-limited spatial resolution. Single DNA molecules are attached to ferromagnetic nanoparticles at one end and the diamond sensor at the other. DNA biophysical quantities are measured by imaging the ferromagnetic particle orientation. The sensor fabrication, optical and microwave measurement system, fundamental and practical sensitivity limitations are presented. Two types of magnetic moment orientation imaging are advanced: dynamic magnetic orientation sensing and static magnetic orientation sensing.

In the dynamic imaging modality, a novel quantum control technique for high sensitivity dynamic imaging is developed and applied to image the dynamic reorientation of a DNA-tethered ferromagnetic particle for the first time. In the state-of-the-art diamond sensor constructed for this bio-mechanical orientation sensing platform, microscopic inhomogeneities due to diamond crystal strain were found to limit magnetic sensitivity and magnetic particle imaging frame rate. A novel quantum protocol was developed which exploits the symmetry of the NV defect ground state structure to mitigate the contribution of microscopic inhomogeneities in non-magnetic fields, and double the contribution of magnetic fields to the imaging signal. A DNA-tethered ferromagnetic particle was reoriented by an applied fluid flow, and the quantum control protocol enabled imaging of this reorientation at video rates. This proof-of-principle experiment is a concrete demonstration of unbleaching, high-frame-rate dynamic bio-mechanical orientation tracking using ferromagnetic particles.

In the static imaging modality, the quantum imaging platform is used to directly probe the bend stiffness of nuclesome-scale DNA fragments. In previous experiments, the bend stiffness of short, nucleosome-scale DNA molecules appears to disagree with the standard polymer bending model which is compatible with longer DNA length scales. However, prior experiments have relied on either indirect inference measurements or measurements

of ensembles of DNA molecules to quantify short-DNA bending. In this thesis, DNA-tethered ferromagnetic probes are used in a magnetic tweezer assay to construct a nano-mechanical torque balance that can directly measure the bend stiffness of individual DNA molecules. The quantum imaging platform is used to measure the ferromagnetic probe moment direction and applied magnetic tweezer field direction simultaneously. Deviations between the probe moment vector and the applied field vector provide a measure of the torque exerted by the DNA molecule on the ferromagnetic probe. The direct measurement of the bend stiffness of individual DNA molecules is performed for a first time.

This collection of work represents a significant development in quantum-enabled bio-sensing to address fundamental questions in biophysics and inspires further biophysical measurements and quantum sensor development.

TABLE OF CONTENTS

LIST OF FIGURES

Figure Number Page

ACKNOWLEDGMENTS

Like a large stream fed by smaller inlets, this thesis is the sum total of the effort of many individuals.

First, I would like to thank my primary advisor Kai-Mei Fu. In our time working together I've been lucky to partially absorb many of the qualities I value in them like their thoughtfulness, deep and penetrating understanding, attention to detail, enthusiastic vigor, resilience, organization, punctuality and confidence. They have had the single greatest influence on me as a scientist and I feel very grateful I had the opportunity to work so closely with them over these years.

Thanks to my secondary advisor Paul Wiggins. I have learned so much from Paul about DNA, microscopy, views from 30,000 feet, getting down to brass tacks, and turning bugs into features. Paul's mantra that 99.9% of all single-molecule biophysics experimental data is junk has been one of the most validating things I've heard in my time at UW. I'm grateful to have had his attention with all aspects of my work and have benefited greatly from his lighthearted humor and discerning eye.

Thanks also to Samu Taulu for his continued warmth and openness that stoked my enthusiasm about technologies yet to come, and for sharing learnings from his deep experience in magnetoencephalography.

I thank the rest of my supervisory committee and other professors I've benefited from in my time at UW: Subhadeep Gupta, Armita Nourmohammad, Wendy Thomas, Miguel Morales, Steve Sharpe and Ann Nelson.

I've been extremely blessed to have worked with and been inspired by many amazing researchers at UW in many different areas:

In the Quantum Defect lab: Christian Pederson, Vasilieos Niaouris, Xingyi Wang, Nick Yama, Srivatsa Chakravarthi, Maria Viitaniemi, Emma Schmidgall, Mike Gould, Xiayu Lin-

peng, Alan Logan, Ed Kleinsasser, Ethan Hansen, Tommy Nguyen, Ruhee Nirodi, Shivangi Shree, Chris Zimmermann, Asher Han, Isaiah Kim, Nick Brunelle, Lilli Thiel, Chris Moore, Kendall Crane and Thalya Paleologu,

in the Wiggins lab: Isaac Shelby, Dean Huang, Teresa Lo, James Choi, Joey Turnbull, Colin LaMont, Julie Cass and Sarah Mangiameli,

in the QT3 lab: Max Parsons, Adam Cox, Willow Strey, Faizan Samad, and Enrique Garcia,

as well as Tahiyat Rahman, Xinxin Tang, Debby Tran, Myles McKay, Brianna McKay, Liudmila Zhukas, Paul Malinowski, Dake Zhou, Brynn MacCoy, Lupita Tovar, Bethlee Lindor, Nicel Mohamed-Hinds, Michael Sanchez, Lingnan Shen, Hae Lim, Joss Ayres-Sims, and many others.

In this stream of life I've been given I'm indebted to my family. Thanks to all four of my grandparents who now live through the ones they've touched. Thanks to my mom Shehnaz for blessing me with lighthearted humor and the strength to make it through and my dad Phiroze who smiles down on all I do. Thanks to my siblings Nida Obatake and Zerreen Kazi for shaping the person I've become. In recent years this family has extended significantly, and I thank David Obatake for his continued support and Zaid Obatake for being one of the brightest lights in my life.

Thanks to my extended family: Babbu Mama, for much more than I can write here, Suhail, Sufyan, Samia, Ferheen, Azra, Safa, Bilal, and so many more.

Thanks to my Colorado family: one of my biggest cheerleaders Mama Angela Gurule, Savier Salazar, Elijah Cruz, Jade, Damien, Evi, Penelope, Xian and Sami.

Thanks to my friends from all throughout my life for everything: my oldest friends Yeshar Hadi, Kenny Chan, Alex Shung, and Stephen Chen, as well as Maryam Hadi, Vinh Tran, Van Vu, Victor Tran, Vincent Tran, Andy Kwong, Michael Seo, Vinh Nguyen, Hector Mendoza, Olivia Troyan, Brian Walsh, Vanessa Barbosa, Allen Zhou, Ruben Miranda-Juarez, Princess Julia Diya Lee, Emma Bunnell, and many more.

This work and my life in general are only possible with the support and love from my

best friend, my life partner, my wife Akaxia Cruz. She is the biggest inspiration for me as a scientist and as a compassionate human being. I'm forever indebted to her and look forward to continuing our adventures together as our lives unfold.

Finally, I would like to acknowledge myself. During the course of this work I have grown substantially in all aspects. I can see how quickly the fruits of this growth have propagated outward: in this thesis, in my daily life, and far beyond.

DEDICATION

May it be that the innovations, ideas, relationships and scientific discoveries cultivated in this work serve for the welfare, safety, peace and freedom of all beings everywhere.

For as long as space endures
And for as long as living beings remain
Until then may I too abide
To dispel the misery of the world
-Shantideva

Chapter 1

INTRODUCTION

1.1 Background

Sensing is a fundamental process in which one physical quantity is transduced into another and provides the basis for all empirical studies of the universe. Sensor development expands the measurement space and allows scientists to access quantities previously unaccessible. Quantum sensing leverages the strong external field coupling of quantum objects for unprecedented sensitivity to physical quantities such as temperature, electric field, and magnetic field, enabling novel quantum sensing modalities that extend the space of measurement.

Classical sensing utilizes the known response of a probe to an external field in order to measure changes in the external field. Quantum sensing is fundamentally the same but leverages the unprecedented ability to control individual and coherent ensembles of quantum objects and read out their coupling to external fields.

Typical quantum sensing utilizes a two-level-system comprising states $|0\rangle$ and $|1\rangle$ with energy difference E modulated by an external field V, $E = E(V)$ [3]. The external field coupling parameter is defined as $\gamma = \partial^q E/\partial^q V$ with $q = 1$ in the case of a linear response. Measured changes of E are related to the desired quantity V by γ. Quantum sensing relies on high-fidelity state initialization, coherent manipulation, and read-out of the state population in order to measure external fields, which can be accomplished in a variety of platforms as discussed in Chapter 2.

Quantum sensing is especially suited for magnetometry, which classically measures the deflection of a probe magnet to measure an external magnetic field. In the case of quantum magnetic field sensing, a probe magnet that can now be used is an individual or ensemble of electron spins. The response of a spin $\vec{\mathbf{S}}$ to a relatively-weak magnetic field $\vec{B}$ is dubbed the Zeeman effect [4] and is given by $\Delta E = \gamma\vec{\mathbf{S}} \cdot \vec{B}$ where γ is the gyromagnetic ratio of

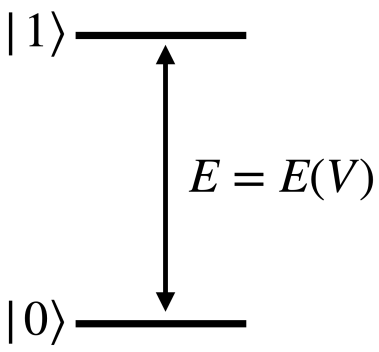

Figure 1.1: **Two-level-system for quantum sensing.** A quantum system with energy levels $|0\rangle$ and $|1\rangle$ couples to an external field V that modulates the energy difference $E(V)$. By measuring $E(V)$, V can be sensed.

the spin. By measuring the splitting of ground-state spin levels, the magnetic field can be measured.

A well-studied platform for quantum magnetometry is the electron spin associated with the negatively-charged nitrogen-vacancy (NV) defect in diamond. The NV defect has long spin coherence times and spin-coupled optical transitions, which enables optical detection of the ground state energy level splittings, and thus optical magnetometry at room-temperature under ambient conditions. This combination of characteristics, along with its solid-state, bio-compatible host material, make the NV center particularly well suited for use in biological contexts. By fabricating a near-surface high-density ensemble of these defects, a wide-field magnetic imaging platform with high-sensitivity and optical-diffraction-limited spatial resolution is constructed.

An established method of studying single-molecule biological systems involves probes attached to otherwise-invisible biosystems, and inferring the underlying biodynamics from the visible dynamics of the probe. For polymers, one such method is called a tethered-particle-motion (TPM) assay, which images an optically detectable probe tethered by a polymer to a surface. Imaging the probe position over time can measure trap stiffness, polymer length and other biophysical parameters associated with the polymer. In this

thesis, the TPM assay is expanded by using a single DNA molecule to tether a ferromagnetic particle to a diamond quantum sensor. NV defects in the diamond are used to image the DNA-tethered probe magnetic moment orientation and infer the bio-mechanical orientation of the DNA molecule.

This thesis advances both dynamic and static magnetic particle moment orientation sensing. Dynamic orientation sensing of an unbleachable ferromagnetic probe attached to a single-molecule system enables long-time-scale bio-mechanical orientation tracking. However, even in a state-of-the-art diamond quantum sensor, micron-scale sensor inhomogeneities were found to limit the sensitivity and time-resolution of the orientation imaging measurements. A novel, necessary quantum control protocol was developed and a proof-of-principle experiment imaging the reorientation of a DNA-tethered ferromagnetic particle was performed. These results demonstrate the viability of dynamic imaging of ferromagnetic probes to image DNA bio-mechanical orientation, as well as opening access to other bio-mechanical systems in which dynamic orientation tracking can illuminate underlying bio-dynamics.

A limit of the dynamic particle moment imaging platform is probe orientation along a necessary applied magnetic field. Leveraging this applied field as a tool, the next project utilized the applied external magnetic field to form a nano-mechanical torque balance with ferromagnetic nanoparticles attached to DNA molecules. In this magnetic tweezer assay, the bending of single DNA molecules was directly imaged as a deflection between the probe magnetic moment vector and applied magnetic field vector. Both static vectors were imaged simultaneously using the wide-field quantum imaging platform. Using this novel experimental scheme, the direct measurement of the bend stiffness of nucleosome-scale DNA molecules was performed. The bending of DNA molecules longer than the nucleosome scale was found to be consistent with prior measurements of bend stiffness, building to the ability to probe the bending of sub-nucleosome scale DNA molecules.

1.2 Overview of thesis

This thesis begins with an overview of the operating principles for diamond NV magnetometry and fundamental and practical sensitivity limits in Chapter 2. Chapter 3 introduces

the challenge and potential discoveries in single-molecule DNA orientation sensing, and motivates the use of magnetic particle probes for bio-mechanical orientation measurements. Next, the diamond-based magnetic particle imaging (magPI) platform for bio-mechanical sensing is introduced. The magPI platform's development, operation, and applications are explored in Chapter 4. Then, a novel quantum control scheme to enable dynamic magnetic field imaging using the magPI platform is detailed in Chapter 5, along with a proof-of-principle demonstrating dynamic bio-mechanical orientation tracking. Chapter 6 details a nano-mechanical torque balance used to probe single-molecule DNA bend stiffness using magPI in a magnetic tweezer assay. Chapter 7 summarizes the thesis and presents an outlook about further directions for the magPI platform and quantum magnetic imaging for biological applications.

Chapter 2

QUANTUM MAGNETIC FIELD SENSING

2.1 Introduction

In this chapter, the principles of magnetic sensing using diamond nitrogen-vacancy (NV) defects is presented in detail. Then various other quantum magnetometry platforms are introduced and compared to the diamond NV platform, including superconducting quantum interference devices (SQUIDs), atomic vapor cells (AVCs), and other solid-state defects.

2.2 Diamond nitrogen-vacancy centers

The nitrogen-vacancy (NV) center is a point defect in diamond comprised of a substitutional nitrogen atom and adjacent vacancy with C_{3v} point group symmetry [5]. In the negatively-charged configuration, six electrons are associated with the NV center: one from each of the adjacent carbon atoms, one from the lattice, and two from the nitrogen. Four sp^3 atomic orbitals are occupied, and the two unpaired electrons compose the NV electron spin $S = 1$, with quantization axis along the NV symmetry axis $\vec{z}_{NV}$ [6]. The electronic states are a linear combination of the four orbital states: the ground state manifold is an orbital-singlet spin-triplet $^3A_2$ state, the electronic excited state is an orbital-doublet spin-triplet ^3E state, and there are two metastable singlet states: orbital-doublet spin-singlet ^1E and orbital-singlet spin-singlet $^1A_1$ states[5]. The $^3A_2$ and ^3E manifolds can be effectively described by three sub-levels labeled by electronic spin projection along the NV symmetry axis with quantum number m_s as seen in Figure 2.1(a). Optical excitation from the $^3A_2$ results in cycling transitions with the ^3E manifold. These transitions exhibit spin dependence due to an inter-system-crossing (ISC) that preferentially decays from $|m_s = \pm 1\rangle$ excited states through the singlet manifold with ZPL at 1042 nm down to the $^3A_2$ states, resulting in fluorescence intensity contrast between the $^3A_2$ sub-levels [7]. Thus, the $^3A_2$ Hamiltonian and its coupling to external fields can be optically probed, providing a platform for quantum

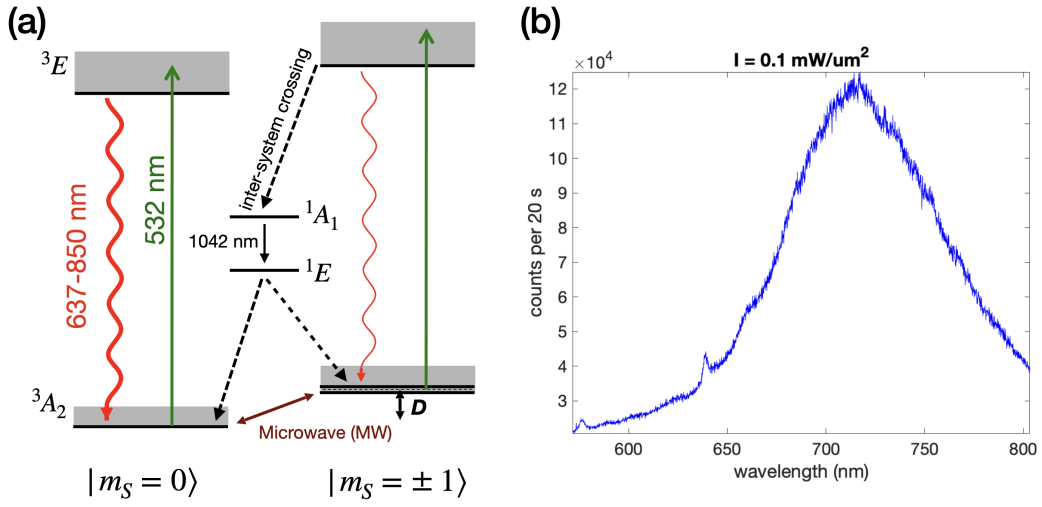

Figure 2.1: **NV$^-$ energy level diagram and photoluminescence spectrum.** (a) The NV electronic energy levels reside deep in the band gap of diamond. In the absence of magnetic field, the ground state $|0\rangle$ and $|\pm1\rangle$ electron spin levels are split by the zero-field-splitting D. A cycling optical transition is present for both spin levels. An inter-system-crossing through singlet states couples more strongly to the $|\pm1\rangle$ spin levels, enabling spin initialization to the $|0\rangle$ electron spin state with off-resonant optical excitation. Microwave excitation rotates the spin to the $|\pm1\rangle$ states. (b) Room temperature photoluminescence spectrum of an ensemble of NVs. A sharp peak is observed at the 637 nm ZPL and the phonon-sideband is present up to approximately 850 nm.

sensing.

2.2.1 $^3A_2$ Hamiltonian

The $^3A_2$ Hamiltonian is given by the sum of the ground state $\hat{H}_{gs}$, Zeeman $\hat{H}_{Zeeman}$, and lattice strain $\hat{H}_{strain}$ interactions,

$$\frac{\hat{H}}{h} = \hat{H}_{gs} + \hat{H}_{Zeeman} + \hat{H}_{strain}. \tag{2.1}$$

The ground state Hamiltonian comprises fine and hyperfine structure and is given by

$$\hat{H}_{gs} = \vec{\mathbf{S}} \cdot \hat{\mathbf{D}} \cdot \vec{\mathbf{S}} + \vec{\mathbf{S}} \cdot \hat{\mathbf{A}} \cdot \vec{\mathbf{I}} \tag{2.2}$$

where $\vec{\mathbf{S}}$ is the electron spin vector operator, $\hat{\mathbf{D}}$ is the fine structure tensor, $\hat{\mathbf{A}}$ is the hyperfine tensor and $\vec{\mathbf{I}}$ is the nuclear spin vector operator. The NV C_{3v} symmetry results in $\hat{\mathbf{D}}$, $\hat{\mathbf{A}}$ being diagonal in the NV reference frame. Taking the [111] NV symmetry axis as the z-direction, the ground state Hamiltonian becomes

$$\hat{H}_{gs} = D(T)\hat{S}_z^2 + A_\perp(\hat{S}_x\hat{I}_x + \hat{S}_y\hat{I}_y) + A_{||}\hat{S}_z\hat{I}_z, \tag{2.3}$$

where $D(T)$ is the temperature-dependent zero-field-splitting (ZFS) with $D(T = 300\text{K}) \approx$2.87 GHz and $\partial D/\partial T$ =-74.2 kHz/K near room temperature [8], and $A_{||}$=3.03 MHz and $A_\perp$=3.65 MHz for ^{15}NV [9]. Coupling to magnetic fields is described by the Zeeman interaction with

$$\hat{H}_{Zeeman} = \gamma_{NV}\vec{\mathbf{S}} \cdot \vec{B}, \tag{2.4}$$

where the NV gyromagnetic ratio $\gamma_{NV} = g\mu_B/h = 28$ MHz/mT, with g the electron g-factor $g \approx 2$ and μ_B the Bohr magneton [10]. Lattice strain appears with

$$\hat{H}_{strain} = M_z\hat{S}_z^2 + M_x(\hat{S}_z^2 - \hat{S}_y^2) + M_y(\hat{S}_x\hat{S}_y + \hat{S}_y\hat{S}_x) + N_x(\hat{S}_x\hat{S}_z + \hat{S}_z\hat{S}_x) + N_y(\hat{S}_y\hat{S}_z + \hat{S}_z\hat{S}_y), \tag{2.5}$$

where $\vec{M}$ and $\vec{N}$ are strain dependent coupling amplitudes [11].

2.2.2 Optical initialization and read-out

The $^3A_2$ and ^3E states are coupled by a 637 nm zero-phonon-line (ZPL) transition with phonon-sideband emission up to around 850 nm. This optical transition is spin-preserving and has a lifetime of approximately 13 ns [12]. The $|m_s = \pm 1\rangle$ excited state more strongly couples to the ISC decay pathway which enables optical initialization to the $|m_s = 0\rangle$ state and results in lower emitted photoluminescence (PL) intensity from the $|m_s = \pm 1\rangle$ optical transition [7]. Typical operation excites the NV spin with 532 nm laser excitation to a vibrational excited state, which quickly relaxes to the corresponding ^{3}E state, and then decays in general to a vibrational ground state level with the emission of a photon between 637-850 nm. A NV ensemble room-temperature PL spectrum is shown in Figure 2.1(b). In it a sharp peak is visible at the ZPL alongside the broad phonon-sideband. To determine the NV electron spin state, the entire photoluminesence spectrum is collected and imaged onto a photodetector or camera.

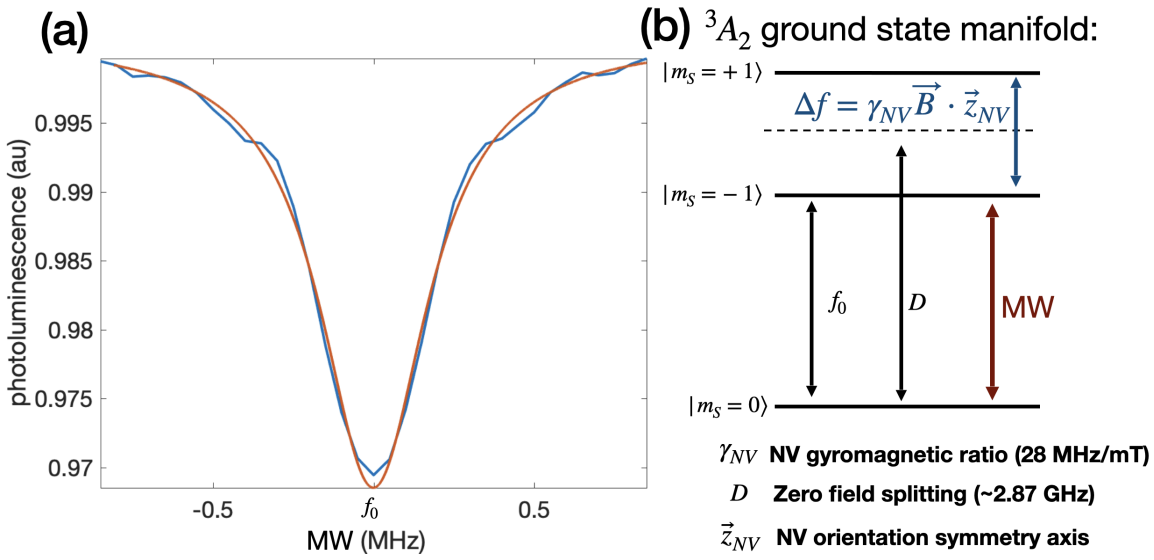

Figure 2.2: **NV$^-$ optically-detected-magnetic-resonance curve and $^3A_2$ ground state manifold.** (a) NV$^-$ photoluminescence is monitored as a function of applied microwave frequency. When the MW is on resonance with an NV ground state electron spin transition, a dip in emitted photoluminescence is observed at f_0. (b) NV ground state mainfold showing the resonant frequency between the $|0\rangle$ and $|-1\rangle$ spin levels f_0, zero-field-splitting D, MW driving range and Zeeman splitting between the $|\pm 1\rangle$ spin levels.

2.2.3 Optically detected magnetic resonance (ODMR) and applications

Using microwave (MW) excitation, the NV spin ground state can be coherently rotated. The spin-state after MW manipulation can be read-out using the spin-dependent PL intensity as discussed above. After initializing the spin-state with a green laser pulse, a resonant MW pulse is applied and the NV spins are rotated from the $|0\rangle$ to $|\pm1\rangle$ states. With a readout laser pulse, a dip in emitted PL is observed called optically detected magnetic resonance (ODMR). A typical ODMR dip is shown in Figure 2.2. The resonant frequencies $f_\pm$ of the ODMR dips are given by the eigenvalues of the total Hamiltonian $\hat{H}$:

$$f_\pm = D(T) \pm \gamma_{NV} \vec{z}_{NV} \cdot \vec{B} + f_{strain} \pm f_{HF}, \tag{2.6}$$

where $\vec{z}_{NV}$ is the NV symmetry axis, f_{strain} is the frequency shift due to strain, and f_{HF} is the frequency shift due to the hyperfine interaction. ODMR enables optical sensing of each quantity that shifts the eigenvalues of the NV spin Hamiltonian, including magnetic field, electric field (via strain), pressure (via strain) and temperature (via zero-field-splitting). Additionally, the nuclear spin of the nitrogen associated with the NV defect can be probed.

NV ODMR for magnetic field sensing

Under the influence of magnetic field, the NV electron spin resonances split according to the Zeeman effect. By measuring the change in ground-state energy levels via ODMR, solely the magnetic field along the NV symmetry axis can be measured:

$$\frac{f_+ - f_-}{2} = \gamma_{NV} \vec{z}_{NV} \cdot \vec{B}. \tag{2.7}$$

The NV resonances associated with the $|0\rangle \leftrightarrow |\pm1\rangle$ transitions split symmetrically about the ZFS. Thus, by measuring each resonance and subtracting, absolute magnetic field sensing with the influence of non-magnetic field explicitly removed is accomplished [13, 14]. This "double-quantum" approach to magnetic sensing will be discussed in detail in Chapter 5.

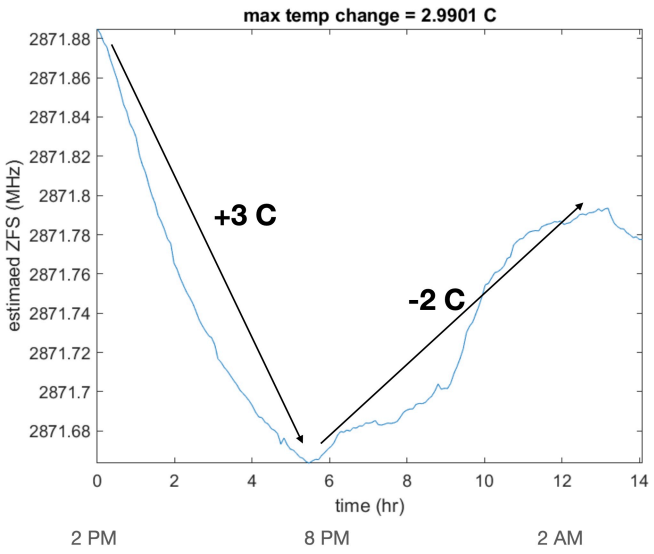

Figure 2.3: **Temperature sensing via ODMR.** The temperature-dependent NV zero-field splitting was probed over 14 hours. From 2PM to 8PM, 3 °C heating was observed, and from 8PM to 2AM 2 °C cooling was observed.

NV ODMR for temperature sensing

Conversely, adding each measured NV spin resonance enables sensing of non-magnetic quantities such as temperature:

$$\frac{f_+ + f_-}{2} = D(T) + f_{strain}. \tag{2.8}$$

An example of this is shown in Figure 2.3 where the NV ZFS $D(T)$ was probed over several hours to probe the potential effects of laser and MW induced heating in bio-orientation measurements. Assuming no change in local strain, temperature changes were computed using $\partial D/\partial T = -74$ kHz/K. While no significant laser or MW induced heating was observed, 3 degree warming was observed during the day while 2 degree cooling was observed overnight, consistent with daily ambient lab room temperature changes.

Application: ODMR hyperfine spectroscopy applied to NV formation study[1]

As seen in Equation 2.6, the hyperfine interaction between the NV electron spin and nitrogen nuclear spin can be probed by ODMR. Natural nitrogen exists as two isotopes, ^{14}N (98.9% abundance) with nuclear spin $I_{14N} = 1$ and ^{15}N (1.1% abundance) with nuclear spin $I_{15N} = 1/2$. When formed into NV, the ^{14}N (^{15}N) nuclear spin splits the ODMR resonances into triplets (doublets). Thus, by measuring high-resolution ODMR, the nitrogen isotope can be probed. When ^{15}N is implanted into a diamond sample and formed into NV, ODMR hyperfine spectroscopy can provide a read-out mechanism that illuminates the origin (either grown-in or implanted) of any given single NV.

This spectroscopy method is used to study the dominant effects of NV center optical instability for use in quantum networks. NV centers are a leading candidate for solid-state quantum networks due to the combination of long spin coherence times and spin-coupled optical transitions. Due to the high index of refraction of diamond, the majority of photons emitted by NVs are totally-internally-reflected inside the diamond. To mitigate the loss of emitted light, NVs can be coupled to photonic cavities that increase collection efficiency and Purcell enhance the ZPL emission [15]. For this, NVs must be formed near the surface of diamond to allow mode overlap between the NV emission and the photonic cavity mode. These near-surface single NVs are typically formed via nitrogen ion implantation and subsequent annealing. However, the optical spectral stability of shallow implanted NVs was shown to be compromised in Ref. [16].

To illuminate the dominant mechanism of the optical instability, two diamond samples A and B were prepared with identical nitrogen implantation energies by the Fu group [1]. For sample A, 85 keV ^{15}N was implanted at almost normal incidence, leading to NV depths of approximately 100 nm. For sample B, 85 keV ^{15}N was implanted at a shallow angle leading to NV depths of about 20 nm. Optical stability was characterized by a photoluminescence-

[1]This section is a part of work that has been published as:
Srivatsa Chakravarthi, Christian Pederson, **Zeeshawn Kazi**, Andrew Ivanov and Kai-Mei C. Fu 2021. Impact of surface and laser-induced noise on the spectral stability of implanted nitrogen-vacancy centers in diamond. Physical Review B, 104(8), p.085425.

https://doi.org/10.1103/PhysRevB.104.085425

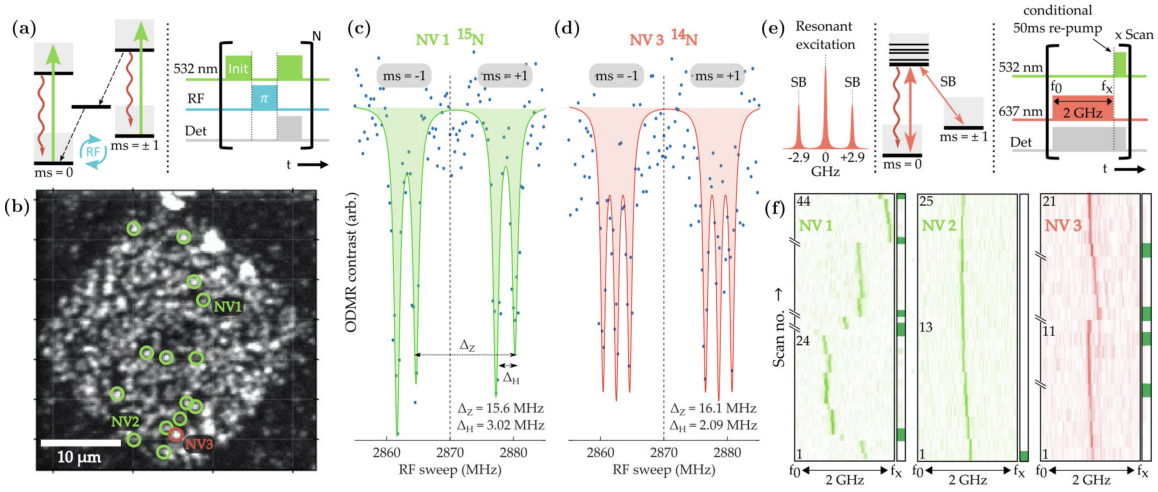

Figure 2.4: **Effect of NV formation mechanism on optical stability.** (a) Simplified NV energy level diagram and PODMR pulse sequence. (b) Confocal scan showing ^{15}N implantation region. Green circles are identified as NVs formed from implanted nitrogen while the red circle is an NV formed from in-grown nitrogen. (c) PODMR spectrum for NV1, and ^{15}NV and (d) NV3, a ^{14}NV. The number of dips observed in the PODMR spectrum illuminates the nitrogen nuclear spin and accordingly isotope, which illuminates the history of the NVs origin (either grown-in or implanted nitrogen). (e) Resonant optical excitation scheme to characterize optical stability of the target NVs. Optical sidebands separated by 2.9 GHz (close to NV ZFS) are added to counteract optical spin pumping. Upon detection of an NV$^-$ ionization event (indicated by disappearance of NV$^-$ PL), a 50 ms off-resonant green re-pump pulse is used to reset the NV charge state. (f) PLE scans as a function of time at 10.5 K for three NVs. Green re-pump pulses are labeled as a function of time by green rectangles along the right column. NV2 shows robust optical stability (narrow optical linewidth and low jitter) despite being an implanted NV. NV3 is an in-grown NV but demonstrates worse optical stability than NV2. Figure originally published in Ref. [1].

excitation (PLE) measurement of the emitter ZPL linewidth, and the origin (either from grown-in or implanted nitrogen) was determined by hyperfine spectroscopy via PODMR. The study found increased optical linewidth and thus decreased optical stability of emitters near the surface. Additionally, NVs formed by nitrogen implanted were observed to demonstrate a spread of behaviors, with both highly unstable and robust PLE signatures observed, see Figure 2.4. This study points to the diamond surface as significant source of defect charge state and spin instability.

2.3 Magnetic field sensitivity

As detailed in the prior section, ODMR of the NV ground states enables optical sensing of fields such as temperature, electric field and magnetic field. The potential sensitivity of this measurement can be explicitly quantified by identifying a noise model associated with the measurement readout. Here, the expression for shot-noise limited dc magnetic sensitivity will be derived. Then the quantum projection noise model will be considered.

2.3.1 Shot-noise limited sensitivity

With all magnetometry sensing techniques, a magnetic field signal is mapped to a difference in NV ground spin state populations. To optically detect this difference, NVs are excited and the emitted photoluminescence is collected. The intensity of the collected PL, or number of collected PL photons, provides information about the spin state of the NV. The noise on number of photons detected in this scheme is modeled by a Poisson distribution and is called Poisson noise or shot noise.

The light emitted by an NV under continuous excitation is collected by a photodetector or camera. Due to the random arrival time of the emitted photons at the detector, the probability of detected n photons is given by

$$P_n = \frac{\langle n \rangle^n}{n!} e^{-\langle n \rangle} \tag{2.9}$$

which is a Poission distribution with mean value n and variance n. The physical interpretation of this equation is that any NV optical detection experiment detecting n photons has an associated uncertainty $\sqrt{n}$.

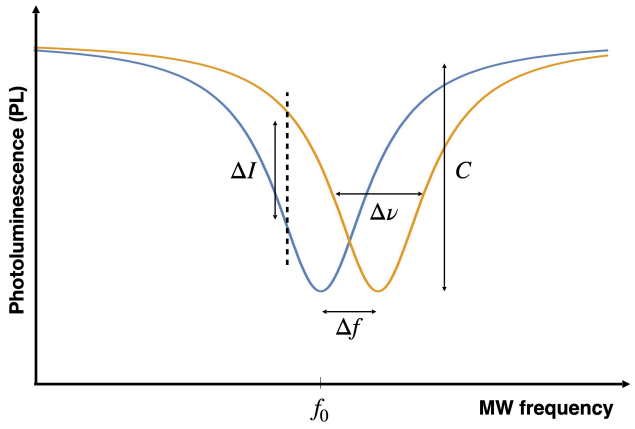

Figure 2.5: **Sensitivity from NV ODMR shift.** A resonance shift in NV ODMR results in a change in collected PL whose magnitude can be quantified using curve shape.

Using this noise model, the sensitivity of measuring quantities associated with ODMR curve shifts can be calculated. The limit of magnetic field detection δB is defined as the magnetic field signal that can be detected with signal-to-noise-ratio (SNR) equal to one. The PL signal S associated with a resonance frequency change Δf is

$$S = Nt\Delta I = Nt\frac{C}{\delta\nu}\Delta f \tag{2.10}$$

with N the photon collection rate, t the integration time, C the fractional optical contrast and $\delta\nu$ the FWHM linewidth. The Poisson noise associated with this measurement is $\sqrt{Nt}$. Thus, an SNR of one yields

$$\sqrt{Nt} = Nt\frac{C}{\delta\nu}\Delta f, \tag{2.11}$$

$$\Delta f = \frac{\delta\nu}{C}\frac{1}{\sqrt{Nt}}. \tag{2.12}$$

The NV electron gyromagnetic ratio γ_{NV} is 28 MHz/mT. Using the Zeeman relationship between change in resonance frequency and magnetic field, the limit of magnetic field detection δB is given by

$$\delta B = \frac{1}{\gamma_{NV}}\frac{\delta\nu}{C}\frac{1}{\sqrt{Nt}}. \tag{2.13}$$

The shot-noise limited sensitivity is defined as

$$\eta = \delta B\sqrt{t} = \frac{1}{\gamma_{NV}}\frac{\delta\nu}{C\sqrt{N}}. \tag{2.14}$$

The limit of FWHM linewidth $\delta\nu$ is given by the inhomogenous spin relaxation time T_2^* of the NV ground states as $\delta\nu_{min} = 1/\pi T_2^*$. With this,

$$\eta_{optimal} = \frac{1}{\gamma_{NV}}\frac{1}{C\sqrt{N}}\frac{1}{\pi T_2^*}. \tag{2.15}$$

The form of Equation 2.15 provides information about experimental parameters that lead to optimal sensitivity. The quantity η is proportional to the minimum detectable field δB, thus minimizing η results in the highest sensitivity. Practically, highest sensitivity conditions are achieved by maximizing T_2^* (thus minimizing FWHM linewidth $\delta\nu$), increasing optical contrast C, and increasing photon count rate N. These three quantities are highly interdependent and are also dependent on other aspects of the sensing platform such as quantum control protocol, sensor fabrication, MW and optical power requirements and NV density. These considerations point to a complex parameter space for magnetic sensing with NVs. Each aspect of the sensing platform must be considered for a specific target application and will be explored further in Section 2.5.

2.3.2 Quantum projection noise limit

The most fundamental limit to magnetic sensitivity is noise associated with quantum state projection. Quantum sensing schemes aim to detect a fractional probability amplitude p corresponding to the population of a quantum state. Instead of measuring p directly as would be for a classical measurement, the quantum measurement returns 0 or 1, with probabilities $1-p$ and p, respectively. The uncertainty in this measurement is then given by a binomial distribution [3]:

$$\sigma_p^2 = \frac{1}{M}p(1-p). \tag{2.16}$$

This uncertainty provides the quantum spin projection noise limit. In general, with M measurements, the noise scales as $1/\sqrt{M}$. In the specific case of quantum magnetometry, the spin-projection limited dc sensitivity is (up to a numerical factor of order 1):

$$\eta_{sp} \approx \frac{1}{\gamma}\frac{1}{\sqrt{NT_2}} \tag{2.17}$$

Sensing technique	CW ODMR	Pulsed ODMR	Ramsey	Spin echo
Field character	dc	dc	dc	ac
Compatible with frequency scan	Yes	Yes	No	No

Table 2.1: Magnetic sensing technique comparison

where M is the number of independent measurements (non-interacting spins) and T_2 is the coherence time [17].

In general, both the spin projection sensitivity limit and shot noise limit must be considered when evaluating sensitivity limits. In this thesis however, the spin projection limit equation 2.17 is approximately $10^6 - 7$ times lower than the shot noise limit equation 2.14 due to the low photon collection efficiency, further discussed in Section 2.5.

2.4 Quantum magnetic field sensing techniques

As detailed in the prior sections, ODMR of the NV ground state electron spin allows for optical readout of magnetic field. With this mechanism, a variety of sensing techniques can be explored for dc and ac magnetometry. These techniques and their strengths and drawbacks will be explored in this section.

2.4.1 Continuous-wave ODMR

The simplest magnetometry technique relies on continuous-wave (CW) optical and microwave excitation of the NV. CW green laser excitation continuously pumps the NV spin state to the $|0\rangle$ manifold, and red PL is continuously emitted and collected with a photodetector or camera. MW excitation, also applied continuously, can either be scanned over each NV $|0\rangle \leftrightarrow |\pm 1\rangle$ spin resonance, or parked at the steepest point of the NV ODMR curve for dynamic sensing. When the MW field is on resonance, a dip in collected PL is observed as the NV spin state transitions from the $|\pm 1\rangle$ excited states back to the ground states via the inter-system-crossing, without the emission of a red photon. Effectively, the efficiency of the MW field's ability to transition the NV spin state is mapped to a difference in population

between the $|0\rangle$ and either $|\pm1\rangle$ electron spin levels, and this difference is mapped via the inter-system-crossing to a difference in emitted PL. To compensate for intensity noise from laser instability, MW power instability, sample and focus drift, PL is often collected with MW on and MW off and then divided, normalizing the ODMR spectra and cancelling out slow drift processes.

CW ODMR is a robust and capable technique for magnetic sensing. In the Fu group, CW ODMR was used to image the magnetic field from individual 20 nm super-paramagnetic nanoparticles [18]. However, the scheme has several drawbacks. Laser and MW excitation applied continuously decreases magnetic field sensitivity as continous optical excitation from the NV ground state decreases the effective lifetime of the state and Fourier broadens the ODMR linewidth [19]. Additionally, continuous high-powered laser excitation delivered to a near-surface NV ensemble can cause thermal instabilities or photodamage to the sensing target. To mitigate these, a similar ODMR technique with staggered pulsed laser and MW excitation is often favorable.

2.4.2 Pulsed ODMR

Pulsed ODMR (PODMR) maintains the conceptual and practical simplicity of CW ODMR but introduces a few key benefits by staggering the optical and MW NV control. In the PODMR scheme, an optical pulse is first applied which initializes the spin state to the $|0\rangle$ electron spin state. Then, a MW π-pulse is applied. After, a final laser pulse is used to read out and re-initialize the spin state. In this scheme, the efficiency of the MW at transitioning the spin state is still mapped to differences in emitted PL, but because the MW field is applied in the dark, the observed ODMR linewidth is not subject to optical power broadening. An experimental comparison between the CW and PODMR pulse schemes on ODMR curves measured with fixed MW power is shown in Figure 2.6: the CW ODMR curve has higher optical contrast, but larger ODMR linewidth. Pulsed ODMR enables a reduced linewidth at the cost of a reduction in optical contrast, illuminating the three ^{14}N hyperfine transitions. Simultaneous driving of the three hyperfine transitions with pulsed ODMR results in high optical contrast with narrow ODMR linewidth.

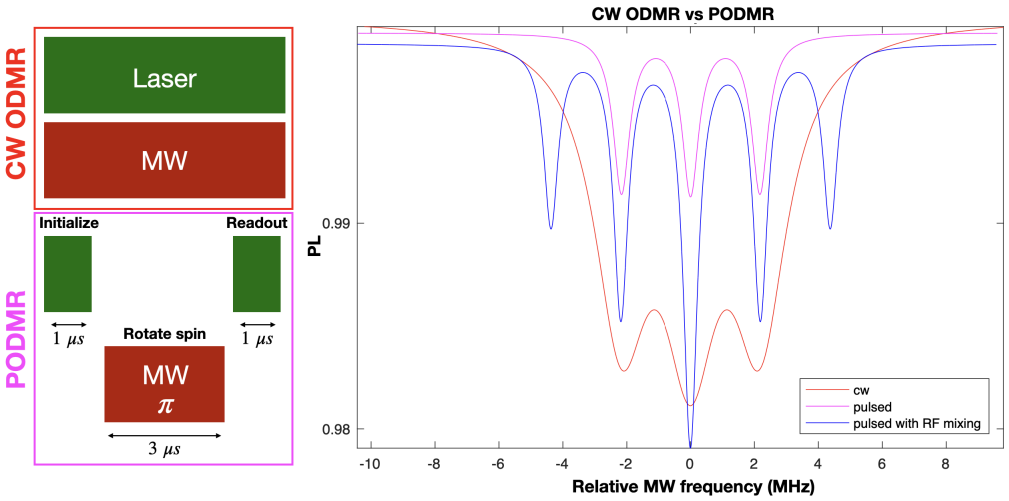

Figure 2.6: **CW ODMR vs PODMR.** Experimental ODMR curves (only fit shown) using CW ODMR, PODMR, and PODMR with ^{14}N hyperfine mixing are compared with fixed MW power. CW ODMR boasts higher optical contrast than PODMR, but with a significantly broadened ODMR linewidth. PODMR reduces this linewidth, and hyperfine mixing combines optical contrast lost to the hyperfine splitting.

Rabi oscillations

To calibrate π pulse times for varying applied MW power, MW pulses of varying duration are applied on resonance with one NV spin transition. A laser pulse initializes the system to the $|0\rangle$ state. A MW pulse with varying duration is applied and PL is collected to measure Rabi oscillations as a function of MW pulse duration. The frequency of these oscillations is called the Rabi frequency Ω_R and represents the temporal frequency of oscillations between the $|0\rangle$ and either $|\pm 1\rangle$ electron spin level. The amplitude $1/e$ decay time of the Rabi oscillations is approximately equal to T_2^*. In general, T_2^* measured with Rabi oscillations is slightly longer than a T_2^* measured by a free-induction-decay (FID) measurement because in the Rabi measurement, the spin is driven during the entire MW pulse duration, for each MW pulse duration. This results in an effective extended coherence compared to the freely precessing wait times used in a Ramsey type measurement.

By understanding Rabi frequency as a function of applied MW field power, specific pulse durations can be chosen to manipulate the spin state in different ways. A pulse with duration $t_\pi = \pi/\Omega_R$ is called a π pulse is used for maximal population transfer from the $|0\rangle$ to the (for example) $|1\rangle$ electron spin level and is used in π-pulsed ODMR as well as dynamical decoupling schemes. A pulse with duration $t_{\frac{\pi}{2}} = \pi/2\Omega_R$ is called a $\pi/2$ pulse and is used to form a superposition state $\frac{1}{\sqrt{2}}(|0\rangle + |1\rangle)$, or in other words, to rotate the electron spin vector into the axial symmetry plane of the Bloch sphere. The $\pi/2$ pulse is used in Ramsey interferometry, spin-echo and other dynamical decoupling pulse sequences.

PODMR, like CW ODMR, is compatible with frequency scanning and limits heating of the diamond sensor and the sensor target. The optimal t_π and thus Ω_R for magnetic sensing is given by $t_\pi \approx T_2^*$. This is due to a balance of two competing mechanisms: on one hand, a short t_π results in a larger population transfer (optical contrast) due to increased MW power and decreased effects of inhomogenous spin dephasing. On the other hand, a short t_π MW pulse is Fourier-broadened, increasing ODMR linewidth. As seen in Equation 2.15, magnetic field sensitivity is proportional to ODMR linewidth and inversely proportional to optical contrast, scaling more strongly with ODMR linewidth. Thus, a longer t_π and spectrally narrower MW pulse is favorable. However, the MW pulse should

not be arbitrarily long as inhomogeous spin dephasing during the application of the MW pulse will degrade optical contrast. For this reason, a $t_\pi \approx T_2^*$ results in the narrowest linewidth for the largest contrast, and thus highest sensitivity ODMR curve. All dynamic magnetic imaging protocols discussed in Chapter 5 are built on the basis of PODMR with MW power tuned such that $t_\pi \approx T_2^*$.

2.4.3 Ramsey sensing

Another dc magnetic sensing scheme relies on Ramsey interferometry, see Figure 2.7. In this pulsed scheme, an optical pulse first initializes the spin to the $|0\rangle$ state. A $\pi/2$ pulse then rotates the spin ensemble into the plane of the Bloch sphere to a state proportional to $\frac{1}{\sqrt{2}}(|0\rangle + |1\rangle)$ (up to a relative phase). The spin ensemble is allowed to precess for a wait time τ and accumulates a relative phase proportional to the external magnetic field, then a second $\pi/2$ pulse is applied which converts the accumulated phase between $|0\rangle$ and $|1\rangle$ levels into a population difference between the $|0\rangle$ and $|1\rangle$) ground state energy levels. A final readout optical pulse is used to map the population population difference between the $|0\rangle$ and $|1\rangle$ states into a difference in emitted PL.

To sense magnetic fields, a fixed free precession time τ is used. Then, magnetic field signals cause a change in detuning, which is proportional to Ramsey contrast and thus collected PL intensity. However, the Ramsey scheme is incompatible with frequency scanning with a fixed free precesssion time, because scanning the MW frequency changes the detuning and thus Ramsey fringe frequency.

Ramsey vs PODMR sensing

In this thesis, PODMR is chosen over Ramsey interferometry for several reasons. First, Ramsey schemes achieve optimal sensitivity when the free precession time $\tau \approx T_2^*$. This is due to the balance of two mechanisms: longer integration times resulting in more accumulated phase, and inhomogenous spin dephasing degrading optical contrast. In dynamic imaging, best imaging sensitivity is related to minimizing the MW pulse sequence duty cycle (time between optical pulses). For Ramsey measurements, minimizing the time be-

tween optical pulses means minimizing the MW $\pi/2$-pulse durations used in the Ramsey measurement. Short $\pi/2$-pulse times require high MW powers which can be difficult to deliver homogenously over an imaging field of view and may cause excessive heating of the sensor and the sensing target. For a PODMR scheme, the t_π time of T_2^* (µs scale in this work) is achievable with moderate MW powers, resulting in an optimal imaging duty cycle and minimal heating. Second, Ramsey schemes are incompatible with frequency scanning. This is disadvantageous because if the shifts of the ODMR resonance are larger than the ODMR linewidth, the Ramsey measurement dynamic range is saturated. The Ramsey sensing scheme would not be able to image large changes in applied external field or dynamic fields larger than the ODMR linewidth. The PODMR scheme with frequency scanning is able to image such changes, though would also be saturated in the intensity shift sensing modality. Finally, multi-MW-tone driving in a single π-pulse for PODMR is straightforward to implement. This could be used for hyperfine driving as detailed above as well as in more complicated pulsed control sequences such as those discussed in Chapter 5. Multi-tone driving in Ramsey schemes requires non-square pulse shaping or phase control of the applied MW fields, significantly complicating the experimental setup.

2.4.4 AC sensing: spin-echo and other dynamical decoupling sequences

A Ramsey-type sequence can also be used to measure ac magnetic fields. As will be seen in the next section, NV center magnetic sensitivity can be primarily limited by dipolar interactions with paramagnetic impurities in the diamond whose contributions sum to an inhomogeneous dc noise bath. When sensing ac fields, the contribution of this bath to the phase accumulation in a Ramsey scheme can be cancelled out using a π-pulse midway through the Ramsey sensing sequence[20]. The π-pulse with equal free precession time on either side undoes phase accumulation due to slowly varying fields. By measuring the amplitude of the echo as a function free precession interval 2τ, the homogenous spin dephasing time T_2 can be measured, see Figure 2.8. Spin echo is an example of a dynamical decoupling sequence, a protocol that applies varying MW manipulations to NV spins to extend spin coherence by isolating the spin from noise due to the environment.

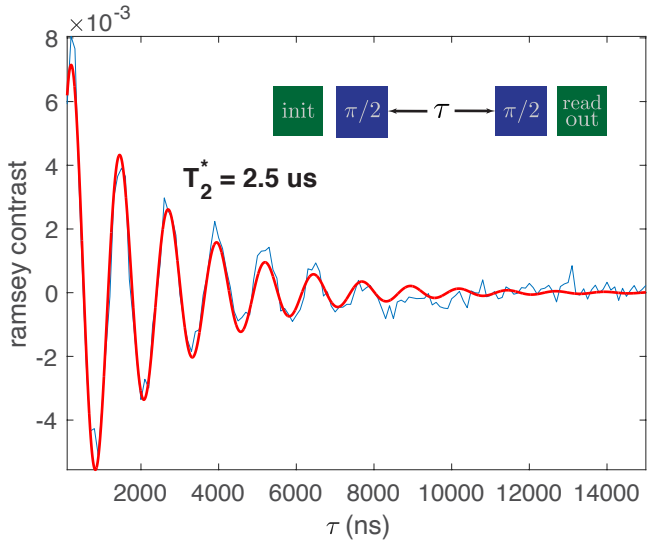

Figure 2.7: **Free-induction-decay (Ramsey) measurement.** A Ramsey measurement is performed with varying free precession time τ and detuning of 600 kHz on a ^{15}NV sample. The normalized data is fit to an exponentially damped sinusoid to extract an amplitude decay time of T_2^* =2.5 µs. The Ramsey pulse sequence is shown in the inset.

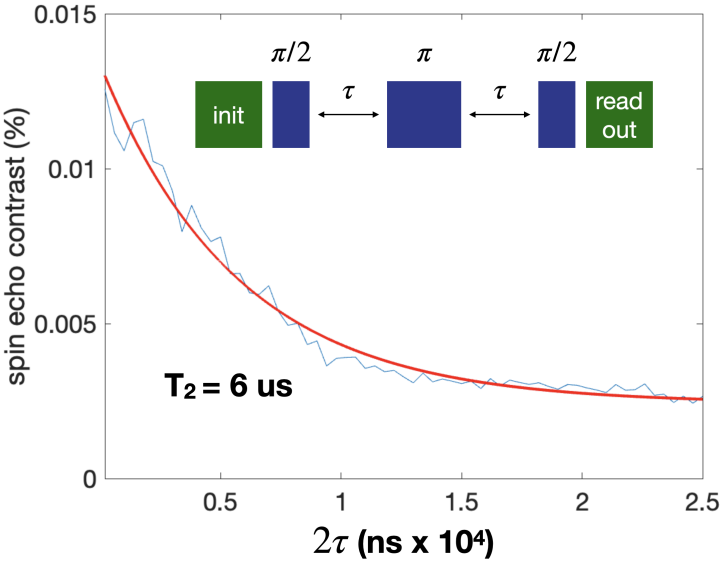

Figure 2.8: **Spin echo decay measurement.** A spin echo decay measurement is performed with varying free precession time 2τ on a ^{15}NV sample. The normalized data is fit to an exponential to extract an amplitude decay time of T_2 =6 µs. The spin echo pulse sequence is shown in the inset.

2.5 Limits to magnetic sensing parameters

In section 2.3.1, the expression for dc shot-noise limited magnetic sensitivity was derived and parameterized by three quantities: ensemble spin coherence time T_2^*, optical contrast C and photon collection rate N. This section details the inter-relation between each of these quantities and their fundamental and practical limitations, as well as their dependence on other relevant sensor parameters like material properties (NV and other paramagnetic impurity densities, strain) and experimental setup parameters (temperature gradients, applied magnetic field gradients).

2.5.1 Optical contrast C

All NV sensing schemes map magnetic field onto a difference in population between the $|0\rangle$ and either $|\pm1\rangle$ electron ground state. As seen above, upon optical excitation this population difference is mapped to a change in relative emitted PL intensity due to a spin-selective inter-system-crossing (ISC). Due to this readout mechanism, optical NV sensing schemes are limited by the amount of spin population that decays down the ISC compared to population that decays with the emission of a photon. This can be quantified by the branching ratio equal to the ratio of the ISC metastable state lifetime to the NV spontaneous emission lifetime. In ensembles, the metastable state lifetime was measured to be approximately 250 ns [21] and the NV emission lifetime was measured to be approximately 10 ns [12]. The measured optical contrast is determined by a complex relationship between these lifetimes and the branching ratio into the intersystem crossing metastable state [7].

Ensemble effects

In ensembles, the measured optical contrast is less than the branching ratio limit because the four crystallographic orientations of NV all emit PL together. Because of this, when the applied MW field is on resonance with one transition, the emitted PL by the on-resonant orientation dips, while the PL emitted by the other orientations is unchanged. This effect can be mitigated by using preferentially oriented samples as discussed later in section 4.2.2.

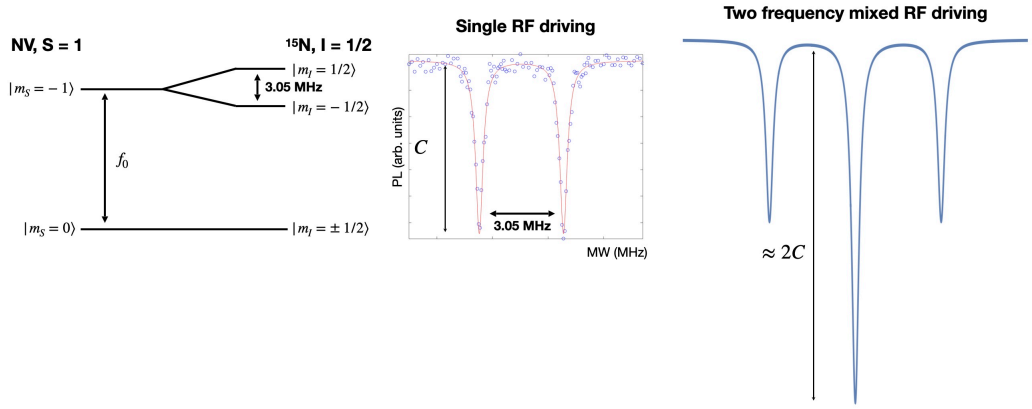

Figure 2.9: **^{15}NV hyperfine RF-mixed driving.** The hyperfine interaction between the NV electron spin and nitrogen nuclear spin splits the electron spin resonance into $2I+1$ levels, where I is the nitrogen nuclear spin. Simultaneous driving of both hyperfine spin levels effectively restores the contrast, allowing for a factor of 2 improvement in sensitivity.

Hyperfine interaction effects

The hyperfine interaction between the NV electron spin and nitrogen nuclear spin also in general reduces optical contrast by splitting the ODMR resonance into either two or three lines for ^{15}NV and ^{14}NV, respectively. This effect is only observable when the ODMR linewidth is less than the hyperfine coupling strength, approximately 3 MHz for ^{15}NV. The reduced optical contrast can be partially restored by simultaneous driving of the two transitions as seen in Figure 2.9.

Charge state dynamics

The negatively-charged NV center (NV^-), the subject of quantum information and sensing studies, can also exist in the neutral (NV^0) charge state at room temperature. The favored charge state of NV is determined by the Fermi energy level at the defect. The Fermi level is dependent on electron donor or acceptor impurity density and proximity to the surface, as the surface may provide many impurities that destabilize the NV charge state.

In general, under optical excitation, the NV is subject to fast ionization and re-ionization,

so that any PL measurement on an NV results in a contribution from both charge states as seen in Figure 2.11. The spectral contribution from distinct charge states can be explicitly isolated using MW modulation as demonstrated in Ref. [22].

This measurement is accomplished in several steps. First, a PL spectrum is collected at fixed laser power without MW excitation:

$$I_{MWoff} = \mathrm{NV}^0 + \mathrm{NV}^-. \tag{2.18}$$

This spectrum comprises PL from both charge states. Next, a spectrum is collected with resonant MW driving:

$$I_{MWon} = \mathrm{NV}^0 + C\mathrm{NV}^-, \tag{2.19}$$

where C is the ODMR optical contrast. Using these two equations, the PL spectrum associated with each charge state can be measured separately:

$$\mathrm{NV}^- = \frac{I_{MWoff} - I_{MWon}}{1 - C}, \tag{2.20}$$

$$\mathrm{NV}^0 = I_{MWoff} - \mathrm{NV}^-. \tag{2.21}$$

This is shown experimentally in Figure 2.10. Using this method, the E1420 magPI sensor diamond $\mathrm{NV}^-/\mathrm{NV}^0$ ratio is measured and shown as a function of excitation laser power in the right panel of Figure 2.11. This data shows that with large excitation laser power the ensemble is mostly in the neutral charge state, caused by the large ionization of NV^- and the relatively low concentration of nearby electron donors ready to donate an electron to NV^0. This result naively points to minimizing excitation laser power for optimal NV charge state, and thus highest optical contrast and best sensitivity. However, lower excitation laser power minimizes photon count rate N, compromising sensitivity. A balance between the charge state fraction and a large photon emission rate must be achieved. This can be accomplished by understanding the electron donor and acceptor environment of the NV sensing layer. Practically, optimal optical intensity is determined by sweeping optical intensity and measuring ODMR to probe the parameters (optical intensity and optical pulse duration) that lead to highest sensitivity.

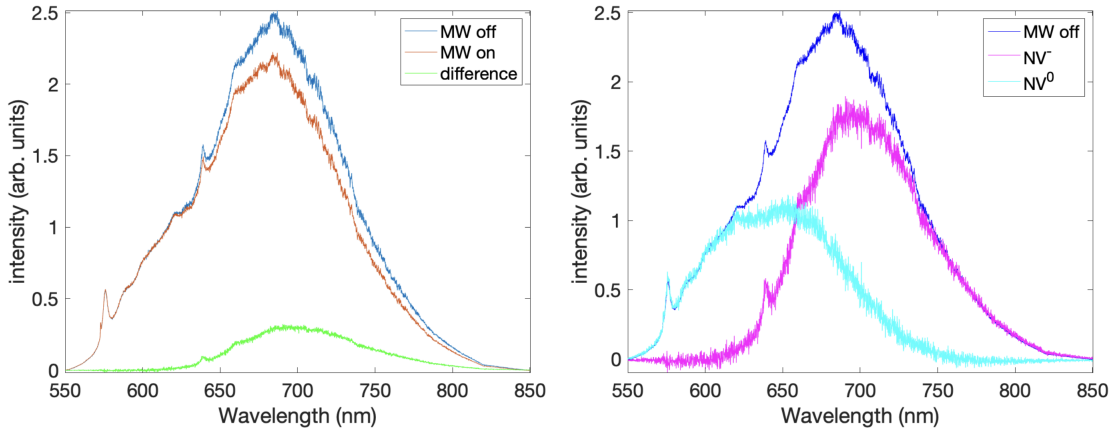

Figure 2.10: **Microwave modulation to isolate distinct NV charge state PL spectra.** (left) NV ensemble PL spectra with MW on and MW off are collected. The difference between off and on is plotted. (right) By scaling the difference spectrum, the NV^- and NV^0 spectra are isolated. The measurement was performed on a ^{15}NV sample with excitation optical intensity 0.1 mW/μ^2.

2.5.2 Photon collection rate N

As in any shot-noise limited measurement, higher photon collection rate N leads to better sensitivity for NV magnetometry. There are several physical mechanisms that limit the amount of photons collected for these schemes.

Diamond index of refraction

The biggest challenge with optical NV sensing is the large index of refraction of diamond, $n_{diamond}$=2.4. This prevents most of the light emitted by NVs from ever escaping the diamond, as the critical angle for total-internal-reflection between a diamond-air interface is $\theta_c \approx 24^\circ$ ($\theta_c \approx 32^\circ$ for a diamond-water interface). Many schemes have been used in order to mitigate this loss, such as integrating near-surface NVs with photonic devices [15] or fabricating nanopillars into the diamond to guide light out [23]. However, most of these schemes are incompatible with ensemble-based sensing, or severely degrade NV spin coherence and

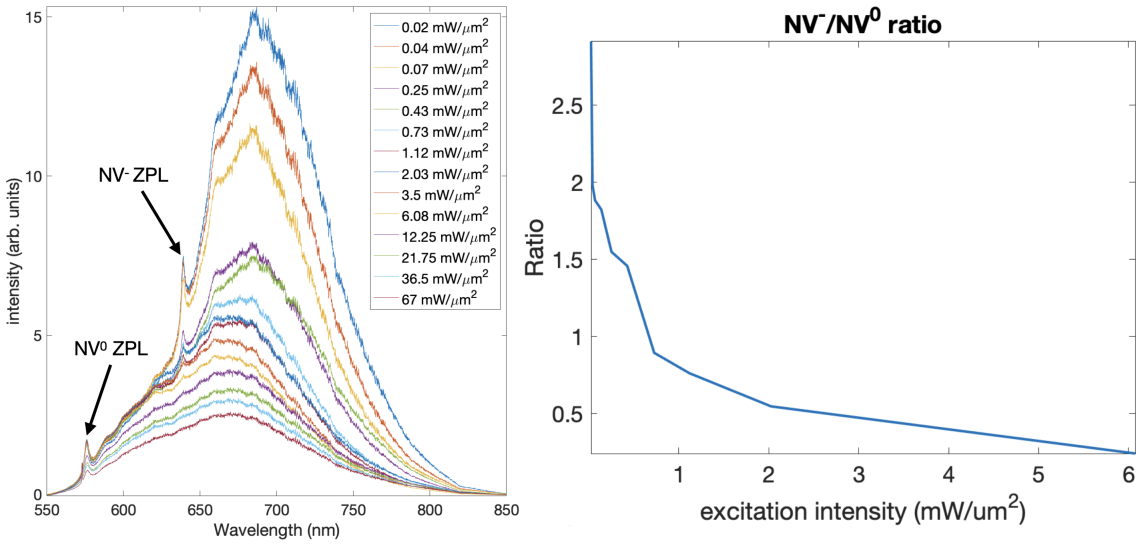

Figure 2.11: **Room temperature (RT) NV PL spectra and charge state ratio as a function of laser power.** (left) PL spectra were taken using a confocal microscope with 1 µm^2 spot size as a function of 532 nm laser power on a ^{15}NV sample. The PL spectrum intensity is normalized by the excitation power intensity. The NV^0 ZPL is observed at approximately 575 nm. The NV$^-$ ZPL is observed approximately 637 nm. (right) Using a MW modulation technique, the PL spectra of NV$^-$ and NV^0 are measured and the total-integrated-spectrum ratio is plotted as a function of excitation power.

optical stability. In this thesis, the large index of refraction issue is mostly unaddressed. TIR excitation and an oil-immersion objective lens are used to maximize counts, but the collection efficiency for NV photons is still on the order of 1%.

NV density

A simple method for increasing NV PL counts is to simply increase NV density. This effect significantly increases sensitivity when the monitoring signals from individual NV centers is not necessary. Multiple NVs in an optically diffraction limited interrogation spot are referred to as an NV ensemble. However, there are several nuanced considerations to arbitrarily increasing NV density in NV ensembles.

Following the discussion in Ref [24], if the NV sensitivity is limited by inhomogenous broadening due to strain or lattice damage, sensitivity increases with increasing NV density. When [NV] increases, [N] increases (typically proportionally), so increasing NV density is advantageous until the dipolar broadening becomes comparable with inhomogenous broadening. In the dipolar broadening limit, increasing NV density and decreasing ensemble spin coherence is still advantageous for sensitivity until ensemble spin coherence time T_2^* becomes comparable with pulsed initialization t_{init} and read out times t_R. Surpassing the duty cycle limit with $T_2^* \approx t_{init} + t_R$ as in this work leads to optimal sensitivities, pointing to a practical limit of NV density for fundamental NV ensemble sensitivity.

Additionally, increasing NV density increases laser and MW power requirements which can have deleterious effects on other aspects of the sensing platform, including compromised optical contrast as seen above, heating and photodamage issues, as well as being cost ineffective.

Excitation laser power

NV centers are typically excited by an off-resonant laser. A simple method for increasing PL count rate is increasing excitation laser power. However, as discussed before, increased laser power increases NV ionization. In this work, to find the optimal optical excitation conditions, PODMR curves as a function of optical intensity and optical pulse duration

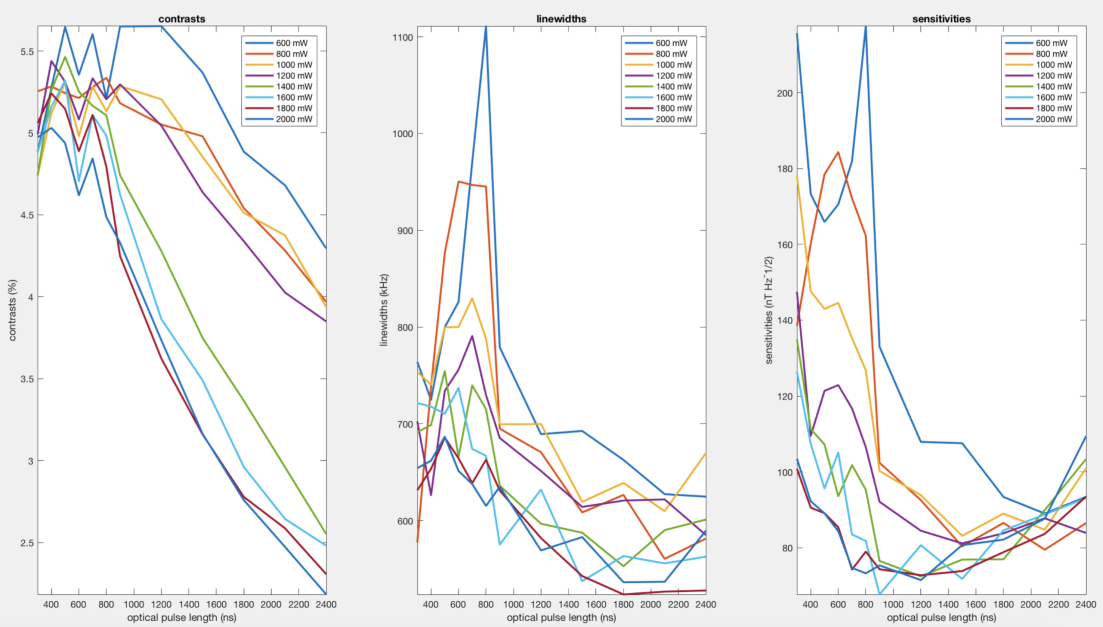

Figure 2.12: **Optical intensity and pulse length sweep.** Laser power (set on 2 W laser) is swept over a range. For each laser power, optical pulse length is swept and PODMR is measured at each parameter setting. ODMR contrast, FWHM linewidth and sensitivity are plotted.

were collected. The fitted optical contrast, FWHM linewidth and dc magnetic sensitivity were plotted, see Figure 2.12. The data points to optimal sensitivity with an optical pulse time of 800 ns with a large range of optical powers, corresponding to approximately 0.1-0.5 mW/µm^2 optical intensity.

2.5.3 Ensemble spin coherence time T_2^*

The parameter with the largest effect on dc magnetic sensitivity is the inhomogenous ensemble spin coherence time T_2^*. It is also the parameter with the largest room for improvement. In an NV ensemble, several physical mechanisms contribute to T_2^*. Following Ref [25], the

various contributions to T_2^* are itemized:

$$\frac{1}{T_2^*} = \frac{1}{T_2^*[NV\text{-}^{13}C]} + \frac{1}{T_2^*[NV\text{-}N]} + \frac{1}{T_2^*[\text{other spins}]} + \frac{1}{T_2^*[\text{strain gradients}]} + \frac{1}{T_2^*[\text{temperature gradients}]} + \frac{1}{T_2^*[\text{magnetic gradients}]} + ... \quad (2.22)$$

In the rest of this section, each of these contributions are addressed. Additionally, practical limits to long T_2^* are discussed.

Spin-spin interactions

In this work, the NV is used to detect classical fields such as temperature and magnetic field. However, NV spin coherence is predominantly limited by dipolar spin-spin interactions with other spins present in the diamond lattice. In the case of two spins $\vec{\mathbf{S}}_1$ and $\vec{\mathbf{S}}_2$ with gyromagnetic ratios γ_1 and γ_2, the dipolar interaction Hamiltonian is given by

$$\hat{H}_{dip} = -\frac{\mu_0 \gamma_1 \gamma_2 \hbar^2}{4\pi r^3}[3(\vec{\mathbf{S}}_1 \cdot \hat{r})(\vec{\mathbf{S}}_2 \cdot \hat{r}) - \vec{\mathbf{S}}_1 \cdot \vec{\mathbf{S}}_2] \quad (2.23)$$

where $\vec{r}$ is the vector connecting the two spins. The dipolar interaction scales linearly with gyromagnetic ratio and diminishes strongly with distance. In a solid state material such as diamond, it is useful to express effective distance between spins by considering the concentration C_S of a certain spin species in the diamond lattice. Effective spacing between spins is given by $d_s = (n_D C_S)^{-\frac{1}{3}}$ where n_D is diamond's number density. With this substitution, the magnitude of the dipolar Hamiltonian can be seen to scale linearly with C_S.

At finite temperatures, nearby like-spins in a diamond can "flip-flop" between up and down spin states with no energy cost and angular momentum conserved, changing the direction of the dipolar magnetic field produced by the spins. This effect for an ensemble of spins creates a spin bath, a spatially inhomogenous magnetic field that causes spin dephasing of NV sensor spins, decreasing T_2^*. The magnitude of the spin bath field for a given species scales linearly with concentration as seen prior. The two most common spins that contribute

to the spin bath in NV ensembles are carbon-13 nuclear spins and electrons localized to substitutional nitrogen defects.

^{13}C

The ^{13}C isotope of carbon comprises 1.1% of all carbon in nature and carries a nuclear spin of $I_{13C} = 1/2$. To mitigate the spin bath due to ^{13}C , advanced growth methods use ^{12}C isotope-purified precursors in chemical-vapor-deposition diamond growth. The spin and optical properties of single NVs placed in a 100 nm thick 99.99% ^{12}C epitaxial diamond layer were shown to be favorable with narrow optical linewidths and long T_2^* [26]. In the current samples, 99.999% ^{12}C diamond is used, significantly damping the effects of the ^{13}C spin bath as will be discussed in Section 4.2.2.

Substitutional nitrogen (P1 centers)

After ^{13}C, the biggest contributor to the spin bath for NV ensembles is substitutional nitrogen defects, also known as P1 centers. These single-lattice-site defects carry an electron spin $S_{P1} = 1/2$. Note that at equal concentrations the contribution of P1 to NV spin dephasing is about 1000× higher than ^{13}C due to the difference in gyromagnetic ratio between electron and nuclear spins. However, P1 center concentrations are typically substantially lower than naturally abundant ^{13}C.

In order for NV center to be engineered in a pure diamond, substitutional nitrogen must be introduced, either by nitrogen ion-implantation or nitrogen doping during diamond growth. After the fabrication protocol, the ratio of [NV$^-$]/[N] is called conversion efficiency. High conversion efficiency is almost always favorable for a smaller spin bath, up to a limit that prohibits NV$^-$ charge state stability. However, the best values of conversion efficiency found in the literature are typically on the order of 10%. This means that in general the concentration of P1 will be 10× the concentration of NV. Further study of diamond growth and processing to increase N to NV conversion warranted and is discussed in Section 4.2.2.

Spin bath driving

Spin bath driving is a technique to mitigate effects of the spin bath by resonantly driving the non-NV spin, rotating it between spin up and spin down at a frequency higher than the interaction frequency such that the NV-spin dipolar coupling given by Equation 2.23 is averaged out [27]. This technique is powerful in its ability to fully eliminate the contribution of the spin bath on NV spin dephasing. However, there are several practical drawbacks to the scheme. Resonant driving of non-NV spins means understanding the level structure of all paramagnetic impurities and applying radio-frequency (RF) tones resonant with each allowed transition, typically on the order of MHz. In general, these resonant frequencies change with magnetic field, so that if the local field changes each resonant frequency must be tuned in order to preserve the positive effects on NV spin coherence. This along with the question of how to deliver high-powered RF fields at different frequencies significantly complicates the experimental sensing setup. For these reasons, spin bath driving is not implemented in the magPI platform. In general, a materials approach may be necessary to eliminate the presence of deleterious spins, as in the case of isotope-purified diamond growth.

Temperature, electric field, strain gradients

Gradients in non-magnetic fields inhomogeneously broaden the NV resonance and decrease spin coherence. The large heat capacity of diamond allows for fast relaxation of any temperature inhomogeneities. In some cases, a thermal heat sink may be used in order to keep the diamond at a stable temperature [28]. Electric field chiefly enters NV sensing with lattice strain which causes shifts in the ODMR energy spectrum [11]. All three of these quantities can be fully eliminated from the ODMR spectrum by measuring each $|0\rangle$ to $|\pm1\rangle$ transition separately and adding, as seen in Equation 2.7 [13, 14]. This "double-quantum" sensing modality will be further discussed in Chapter 5.

Magnetic field gradients

Typical NV sensing requires an applied magnetic field in order to split the degeneracy of the spin transitions for distinct NV orientations. Gradients in the applied field can cause inhomogenous broadening of sensor resonances and limit spin coherence. Care is required when mounting and orienting samples with respect to applied fields, however with inch-scale permanent magnets, applied field gradients can be made extremely small (approx 100 nT/µm), even over 100 µm fields of view. A challenging source of magnetic field degradation on spin coherence is magnetic field gradients due to strong fields from sensing targets. The effect limits sensitivity by decreasing the upper limit on magnetic fields that can be sensed, as seen in Figure 4.10(b). Super-resolution techniques may soften the effects of this mechanism by addressing fewer NVs in an optical spot, decreasing the effects of inhomogenous broadening.

2.5.4 Practical limitations of long T_2^*

As seen prior, T_2^* is related to ODMR linewidth $\delta\nu$ by $\delta\nu_{min} = 1/\pi T_2^*$. The longer T_2^* is, the narrower the ODMR linewidth is. For slope-detection as seen in Figure 2.5, the ODMR linewidth divided by gyromagnetic ratio equals the magnetic dynamic range of the sensor, so a long T_2^* shrinks the sensor dynamic range. In general, the target fields to be sensed must be compatible with the dynamic range given by the T_2^* limited linewidth. In the magPI platform, $T_2^* \approx 2$ µs, so $\delta\nu_{min}/\gamma_{NV} \approx 6$ µT. This dynamic range is compatible with the µT scale fields expected by the magnetic particle fields, further detailed in Chapter 4.

Another challenging effect of long T_2^* is long sensing duty cycles. As seen before, for optimal PODMR, $t_\pi \approx T_2^*$ and for optimal Ramsey, $\tau \approx T_2^*$. These longer duty cycles come with higher sensitivity, but may preclude the application of dc sensing at time scales shorter than T_2^*.

2.6 Other platforms for quantum magnetometry

In this section, two other leading quantum magnetometry platforms are briefly introduced and compared to the diamond NV platform: superconducting quantum interference devices

(SQUIDs) and atomic vapor cells (AVCs).

2.6.1 Superconducting quantum interference devices

Superconducting quantum interference devices (SQUIDs) are loops of superconducting material interrupted by one or more Josephson junctions. SQUIDs measure magnetic field by measuring the induced voltage across the Josephson junctions as a function of magnetic flux through the superconducting loop [29]. SQUIDs readily achieve fT $Hz^{-1/2}$ sensitivities with typically mm-scale sensors and have been used extensively to develop the field of magnetoencephalography [30].

Magnetoencephalography measurements using superconducting quantum interference devices (SQUIDs) have demonstrated live imaging of brain signals during sensory cognition, language perception, motor intention and execution, social interaction, and brain disorders such as epilepsy [31]. SQUID systems require cryogenic temperatures accessed using liquid helium to operate and are contained in a thermally-isolated housing. This housing is one-size-fits-all, preventing a uniform sensor-sample distance for different human subjects. Additionally, SQUID systems require extensive magnetic shielding and room-scale ambient field compensation coils due to their limited dynamic range [30].

SQUIDs have been able to detect low volumes of magnetic nanoparticles in solution [32], but despite their impressive sensitivity, the low ambient magnetic field requirements, cryogenic operation, mm-scale sensor sizes and mm-cm scale sensor-sample distances preclude the application of SQUIDs for single-molecule measurements and individual magnetic nanoparticle imaging.

2.6.2 Atomic vapor cells

More recently, quantum atomic vapor cell (AVC) magnetometers have been established and demonstrate several advantages over SQUIDs [17]. These magnetometers rely on optical detection of the Larmor precession of a spin-polarized ensemble of atoms. AVC sensor nodes can operate at or near room-temperature and can be made compact to cm-scale and can be arranged in a helmet that sits directly on a human subject's head for magne-

teoencephalography [33]. AVCs can operate in various modalities, the most sensitive being spin-exchange-relaxation-free (SERF) which have demonstrated magnetic sensitivities better than SQUIDs [34]. Despite their advantages, SERF AVCs still require a near-zero ambient magnetic field environments, with the most sensitive measurements occuring within multiple layers of magnetic shielding.

Both SQUID and AVC magnetometers have been able to detect bulk ensembles of magnetic nanoparticles tagged to cancer cells [35], but similar to SQUID systems, AVCs cannot are not well suited for single-molecule bio-mechanical measurements due to the cm-scale sensor sizes and and mm-scale sensor-sample distances. The atomic vapor is housed by a cell wall, which limits sensor-sample distances. Additionally, since the atomic vapor is in constant motion with respect to the sensing target, the individual atoms are unable to measure magnetic fields on their own, in contrast to the solid-state NV defect.

2.7 Summary

In this chapter, magnetometry with the diamond nitrogen-vacancy center is discussed in detail, including sensing techniques and the fundamental quantum projection noise and practical shot noise limit of sensitivity. Two other magnetometry platforms, SQUIDs and AVCs are briefly introduced and compared to the NV platform. Chapter 4 builds on this chapter to extend to a wide-field magnetic particle imaging platform that can image the magnetic field produced by individual magnetic nanoparticles.

Chapter 3

SINGLE-MOLECULE DNA BIOPHYSICAL MEASUREMENTS

3.1 Introduction

This chapter introduces the biological motivation for the quantum sensing work detailed in this thesis. Single-molecule bio-mechanical systems are integral to cellular function and have been prior studied using optical microscopy. Relative bio-mechanical orientation is an informative readout of such systems but has historically been difficult to measure, relying on indirect inference measurements of bulk samples [36] or single-molecules [37], or polarization-selective-detection of fluorescent probes [38].

This chapter motivates the diamond-based magnetic particle imaging (magPI) platform used in this work to probe single-molecule bio-mechanical orientation. The primary single-molecule system addressed in this thesis uses a tethered-particle-motion (TPM) assay to probe DNA biophysics. The TPM assay is introduced, and the limits of the TPM assay at sensing bio-mechanical orientation are introduced, motivating the use of magnetic probes in the TPM assay. The rest of the chapter details the standard TPM assay used in the magPI platform to preliminary characterization of the DNA tethering protocols and DNA constructs used in the dynamic orientation imaging in Chapter 5, and the nano-mechanical torque balance in Chapter 6.

3.2 Tethered-particle-motion assay

The TPM assay is a robust experimental technique for measuring the conformal properties of indivdual polymers, including DNA, see Figure 3.1. A DNA molecule is anchored at one end to a surface and a reporter probe of radius R is attached to the other end. By imaging the stochastically fluctuating position vector $\vec{r}$ of the probe, relevant biomechanical quantities such as DNA length L in basepair (bp), tether relaxation time τ and effective spring constant k can be measured [39].

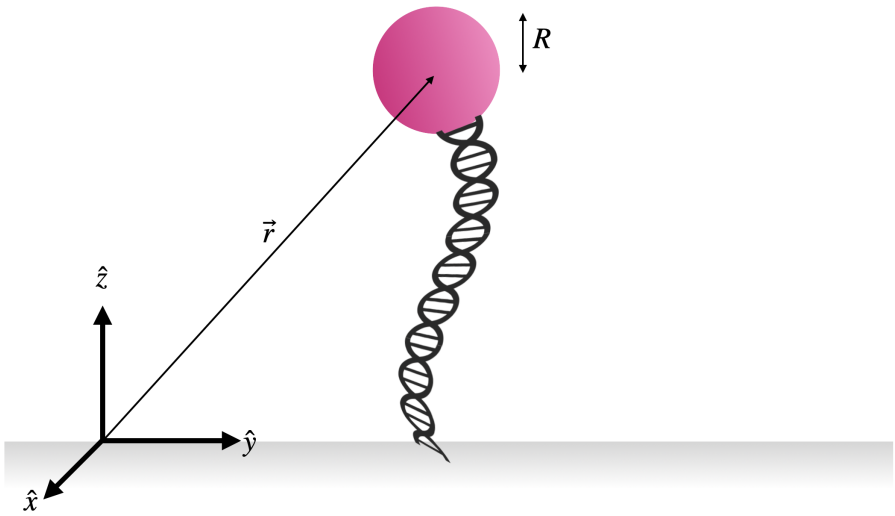

Figure 3.1: **DNA tethered-particle-motion assay.** A particle of radius R is tethered to a surface by a single-molecule of DNA. The position vector $\vec{r}$ of the particle is imaged over time and used to measure biophysical properties of the DNA molecule.

3.2.1 TPM centroid tracking

When the reporter molecule diameter $2R$ is larger than several hundred nanometers, bright-field or phase-contrast microscopy can be used to track probe positions as seen in Figure 3.2. With particles smaller than hundreds of nanometers, dark-field microscopy can be used for the same purpose.

Several hundreds to thousands of images of particle positions are acquired at frame rates commensurate with the tether relaxation time τ, the time scale over which the position fluctuations of the probe are correlated. For each frame, the particle intensity image is fit to a two-dimensional Gaussian. The (x, y) centroids of the fitted Gaussians provide sub-optical-diffraction, sub-pixel resolution of particle position, see Figure 3.3. The time-tagged centroid positions for a given tethered particle comprise a rich data set that can provide informative readouts about the DNA tether.

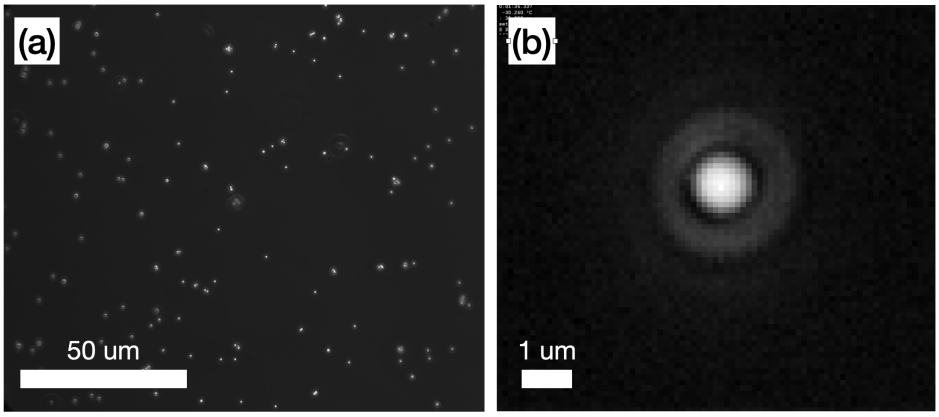

Figure 3.2: **DNA-tethered particles imaged in phase-contrast.** (a) An ensemble of 300 nm polystyrene particles are tethered by 600 basepair DNA molecules to a glass surface. (b) Single particles are localized and tracked to illuminate DNA dynamics.

TPM to measure transcription regulation kinetics

In Ref. [40], the authors used the TPM assay to measure the binding and un-binding of a *lac* repressor, a molecule that inhibits the expression of genes involved with the metabolism of lactose. The *lac* repressor binds DNA at two sites and causes the DNA to loop, prohibiting transcription enzymes from accessing the looped genetic information. Dynamic binding and unbinding of the *lac* repressor was observed by tracking the TPM centroid spread: in the bound configuration, the TPM centroid spread was reduced compared to the unbound configuration.

The *lac* repressor molecule has two operator sites O1 and O3, each of which can attach in two different configurations to binding sites on DNA [41]. With two binding sites, there are a total of four ways in which *lac* can bind to DNA and cause it to loop into four distinct bio-mechanical configurations. Distinguishing between these four distinct bio-mechanical configurations is challenging using solely the TPM centroid spread, and has not been demonstrated thus far.

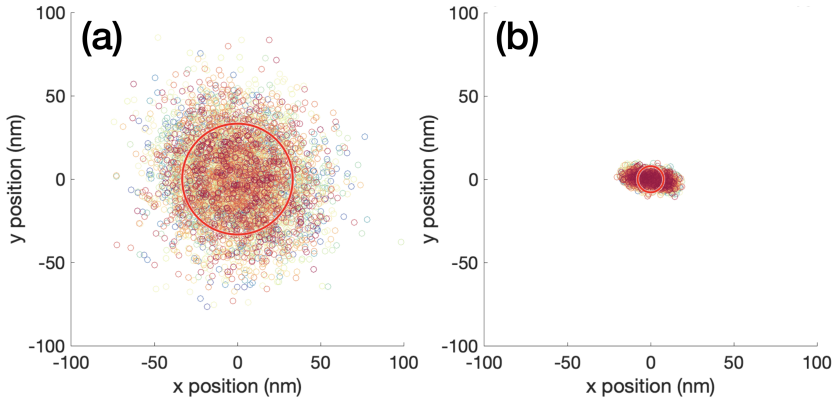

Figure 3.3: **DNA-tethered dark-field centroid traces.** Ferromagnetic nanoparticles are tethered by 600 bp DNA molecules to a diamond surface. (a) Centroid distribution sub-pixel resolution illuminates a symmetric trace with mean excursion shown in red circle. Centroid color (blue to red) indicates increasing time. (b) Centroid distribution for a particle stuck to the diamond surface. Microscope drift leads to an asymmetric centroid distribution with small lateral excursion.

3.2.2 Centroid distribution lateral excursion

A primary readout of the TPM experiment is the lateral excursion $\langle r_\perp^2 \rangle$ of the centroid distribution, given by

$$\langle r_\perp^2 \rangle = \langle (x_i - \bar{x})^2 + (y_i - \bar{y})^2 \rangle \tag{3.1}$$

where $\bar{x}$, $\bar{y}$ are the mean (x_i, y_i) centroid positions. In real tracking experiments, microscope drift is corrected for either by tracking a stuck particle in the same field of view and subtracting the stuck particle centroid positions, or by low frequency filtering the centroid data in time.

$\langle r_\perp^2 \rangle$ is useful because it relates the steady-state centroid distribution to two important length parameters describing a DNA molecule:

$$\langle r_\perp^2 \rangle \approx \frac{4 L_0 L_p}{3} \tag{3.2}$$

where L_0 is the end-to-end contour length (0.34 nm/bp) of the molecule and L_p is the persistence length (typically 50 nm or 150 bp) [39]. Persistence length is a key parameter

that quantifies the length scale over which the end-to-end displacements of a polymer remain correlated [42] and provides information about the bend and twist stiffness of polymer chains.

3.2.3 Centroid distribution symmetry

The symmetry of the centroid distribution is used to characterize the binding character of the DNA-tether. With a single-binding-site tether as in used in Chapter 5, the centroid distribution will be symmetric. One possible symmetry metric is Λ, a dimensionless parameter that is the ratio of the major and minor axes of the lateral centroid distribution:

$$\Lambda = \frac{\lambda_1 - \lambda_2}{\lambda_1 + \lambda_2} \tag{3.3}$$

where λ_i are the eigenvalues of the centroid distribution covariance matrix c where

$$c = \begin{pmatrix} \langle x_i x_i \rangle & \langle x_i y_i \rangle \\ \langle y_i x_i \rangle & \langle y_i y_i \rangle \end{pmatrix} \tag{3.4}$$

where (x_i, y_i) are the time-ordered, mean-subtracted centroid positions and the summation convention is used. To quantify reasonable values of Λ associated with high-symmetry, 10^3 TPM frames distributed by a normal distribution are simulated in 10^7 runs and Λ is calculated for each run, see Figure 3.4(b). Then the simulated Λ values are sorted by p-value and a threshold p-value $p_{threshold}$ selected. This means that centroid distributions with $\Lambda|_{p<p_{threshold}}$ are considered symmetric, see Figure 3.4(a).

3.2.4 Power spectrum and tether-particle relaxation time

A final diagnostic used to understand the tethered particle dynamics relies on auto-correlations of particle position. The frequency or power spectrum of particle correlations can illuminate the relaxation time τ of the tether-particle system, the time scale over which particle positions are correlated:

$$\tau = \frac{8\pi L_0 L_p R \eta}{k_B T} \tag{3.5}$$

where η is the viscosity of the fluid and $k_B T$ is the Boltzmann constant times temperature or thermal energy of the system. The relaxation time τ is a function of both particle radius and

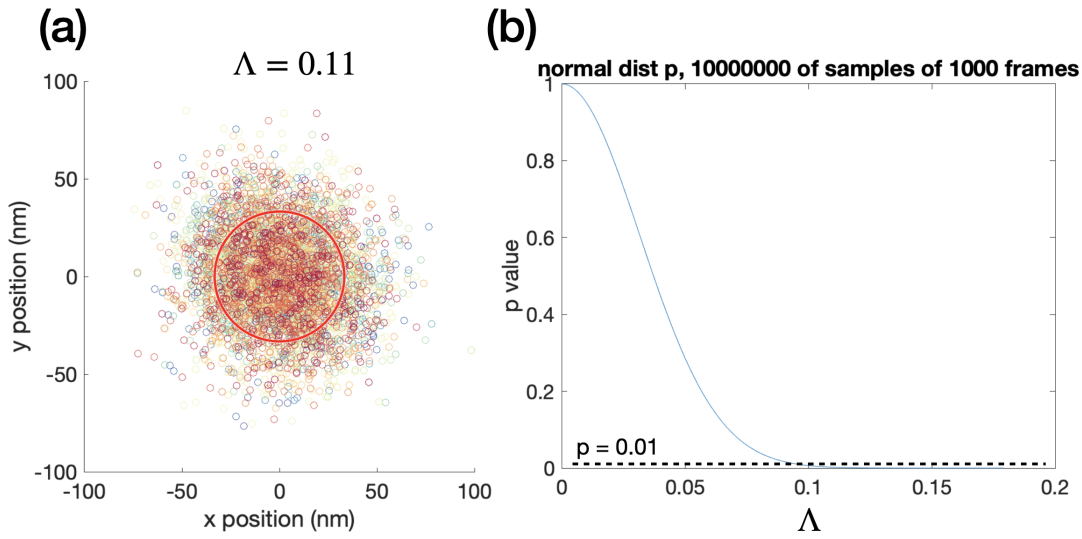

Figure 3.4: **Symmetry metric of TPM centroid traces.** (a) Symmetric TPM centroid trace with Λ=0.11. (b) Simulated symmetric distribution of centroid traces with $p_{threshold}$=0.01.

tether length, providing an empirical measure of both of these quantities. Using a secondary measurement of R such as directly imaging particle size or a secondary measurement of L_0 such as by gel electrophoresis can constrain the other quantity, enabling precise measurement of the both length scales.

In the absence of tethering, the power spectrum of a particle undergoing Brownian motion goes as $\frac{1}{\omega^2}$. With a tethered particle, the low frequency correlations are diminished due to the trapping of the particle and the power spectrum is flat up to a critical frequency $\omega_c = \frac{2\pi}{\tau}$, where the power spectrum "turns over" into standard Brownian motion. This is demonstrated in two examples in Figure 3.5. In these examples, because the DNA length is known, particle size can be estimated from the relation time.

3.3 Summary

In this chapter, the single-molecule DNA tethered-particle-motion (TPM) assay is introduced. This system is the primary bio-mechanical system of interest in this thesis. Stan-

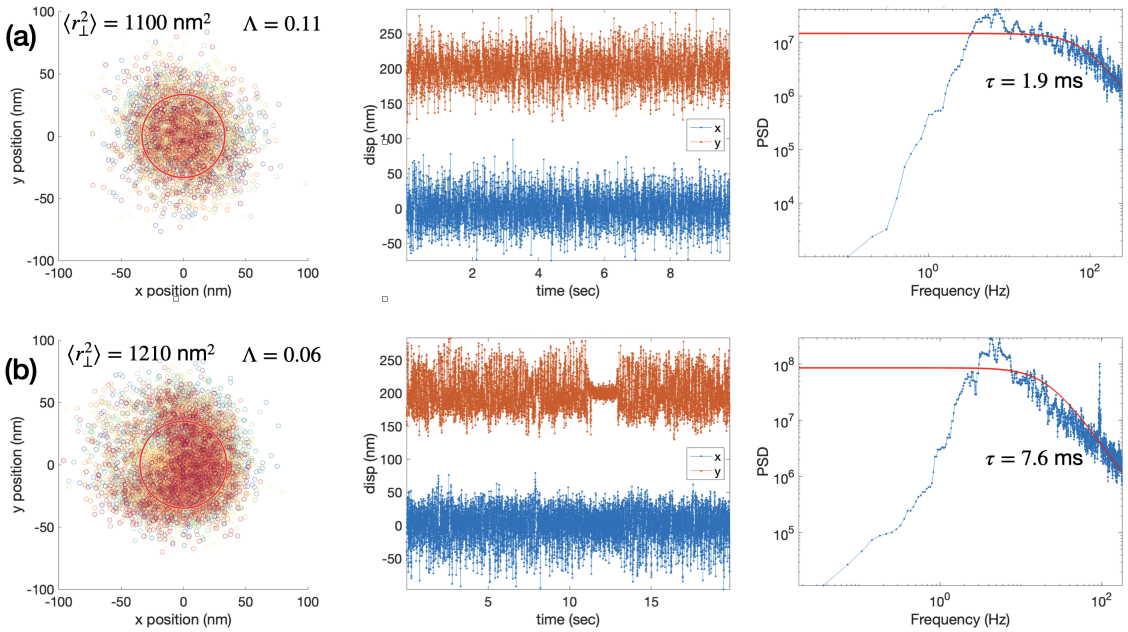

Figure 3.5: **TPM dark-field power spectra.** 2 ms particle position frames are acquired using dark-field microscopy for two different particles (a) and (b) with L_0=600 bp. (left) Centroid distribution lateral excursion and symmetry ratio are calculated. $\Lambda < 0.15$ for both indicates symmetric distribution. (middle) Time traces of particle position are shown, with y promoted by 200 nm for clarity. (b) indicates a transient sticking even around 12 sec. (right) TPM autocorrelation power spectra for both particles with relaxation time inset. For (a), $\tau = 1.9$ ms results in a particle radius of 34 nm. For (b), $\tau = 7.6$ ms results in a particle radius of 138 nm.

dard TPM measurements are introduced, and the limit of TPM to measure distinct biomechanical orientation configurations is discussed, motivating a tethered magnetic particle assay. The next chapter details the quantum sensing platform used to perform tethered magnetic particle imaging.

Chapter 4

DIAMOND-BASED MAGNETIC PARTICLE IMAGING (MAGPI) PLATFORM

4.1 Introduction

One exciting application of quantum NV magnetometry is magnetic field imaging using a diamond sensor comprising a diamond substrate with a high-density layer of NV centers fabricated at the top surface. In this wide-field NV ensemble imaging system, the NV defect photoluminescence can be imaged on to a camera to perform magnetic imaging. Each camera pixel detects emission from an ensemble of NV sensors, typically hundreds to thousands, and the magnetic spatial resolution is optical-diffraction limited, typically on the order of 500 nm. Sensing targets can be brought extremely close to the NV sensing layer, maximizing the field strength at the sensors. In the wide-field system, it is critical that the inhomogeneities across the imaging area are eliminated in order to reach the sensitivity floor given by a single-pixel resonance curve. To this end, the NV community has demonstrated many sensor growth and fabrication methods that increase NV density and homogeneity [8, 43, 44, 45, 46, 24], as well as quantum control methods that suppress non-magnetic field dependence and increase ensemble spin coherence [25, 47, 14, 27].

In this thesis, a near-surface NV ensemble wide-field magnetic particle imaging (magPI) platform is developed and applied. This chapter details the magPI platform experimental design, set up and applications of this platform. Additionally, a six-parameter dipole model used to simulate and fit experimental magPI dipole image data is detailed.

4.2 magPI diamond sensor design

The magPI platform used in this work utilizes a diamond sensor with a near-surface, high density NV ensemble. The relevant parameters in the sensor design are NV layer thickness, NV density, ensemble spin coherence time and nitrogen isotope. The target application for

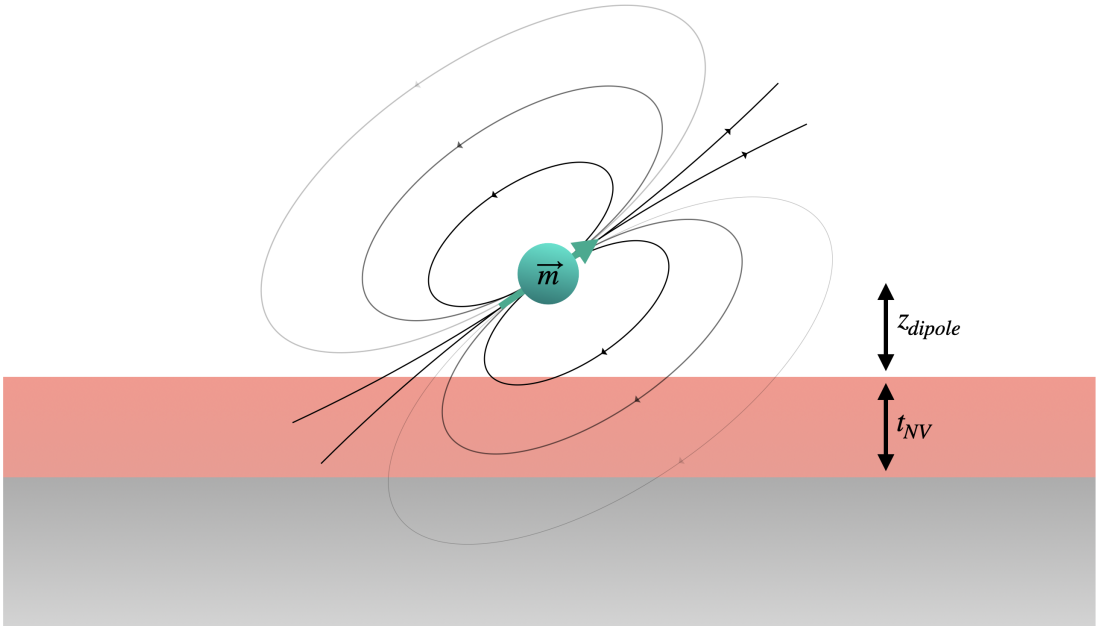

Figure 4.1: **Magnetic particle imaging with a near-surface NV ensemble.** A magnetic particle with magnetic moment $\vec{m}$ is placed at a vertical distance z_{dipole} above a diamond. The diamond has a near-surface NV ensemble of thickness t_{NV}.

the magPI platform is imaging magnetic nanoparticles attached to single-molecule biological systems for bio-mechanical orientation measurements as detailed in the prior chapter.

4.2.1 Sensor thickness

The magnetic field produced by a magnetic nanoparticle can be modeled as a point dipole and is of the form

$$\vec{B}_{\text{dipole}}(\vec{r}) = \frac{\mu_0}{4\pi r^3}(3\hat{r}(\vec{m}\cdot\hat{r}) - \vec{m}) \tag{4.1}$$

where μ_0 is the vacuum permeability, $\vec{m}$ is the point dipole moment vector and $\vec{r}$ is the position vector pointing from the dipole to the field evaluation point. The dipole magnetic field strength falls off quickly as $1/r^3$. Thus, to image a dipole field, it is critical the near-surface NV ensemble used in the magPI platform exists near the surface of the diamond and the thickness of the NV ensemble is tuned for optimal sensitivity. In a wide-field microscopy

system such as the magPI platform, the imaging depth of focus (DOF) is related to numerical aperture and can be approximated by

$$\mathrm{DOF} \approx \frac{\lambda\sqrt{\mathrm{n}^2 - \mathrm{NA}^2}}{\mathrm{NA}^2} \tag{4.2}$$

where λ is the imaging wavelength, n is the imaging index of refraction and NA is the numerical aperture of the microscope objective lens. For a 60X 1.4 NA oil-immersion objective imaging NV fluorescence, the DOF is approximately 0.2 µm. This value increases to approximately 0.4 µm for a 60X air objective. In wide-field microscopy, fluorescence will be collected from NVs throughout the DOF. Having an NV layer that is comparable to imaging DOF can be advantageous for sensing magnetic fields far from the diamond, however, for imaging point dipoles, a bulk NV layer can compromise sensitivity. This is because of the sharp fall-off of dipole magnetic field with distance: NVs within the DOF but far from the dipole will contribute a fluorescence signal but this fluorescence will be absent of magnetic information, contributing noise with no signal. However, the thicker the NV layer, the more fluorescence collected which is favorable for signal-to-noise in the shot-noise limit. Considering these two contrasting SNR contributions, the thickness of the NV layer must be tuned to a balance such that the NV number is high yet the NVs within the layer are sensitive to a dipole magnetic field, but not many extra NVs are emitting fluorescence and compromising signal-to-noise. A rule-of-thumb for optimal sensitivity is to have the NV layer as thick as the dipole is far from the sensor, so $t_{\mathrm{NV}} \approx z_{\mathrm{dipole}}$.

In this work, the target magnetic fields are produced by magnetic particles tethered to DNA molecules. The end-to-end lengths of DNA molecules are typically 75-1000 basepair or 25-300 nm and magnetic particle diameters are typically 30-500 nm. Due to stochastic fluctuations the distance of the magnetic nanoparticle to the diamond is less than the end-to-end length of the DNA molecule. A middle ground value of 150 nm is chosen for the magPI platform, enabling high-sensitivity magnetic imaging of magnetic nanoparticles in the ranges of DNA lengths and particle sizes detailed above.

4.2.2 NV ensemble fabrication

With the target thickness established, there are several avenues for fabricating a thin NV layer with a given NV density[45]. However, the sensor fabrication protocol chosen can affect final magnetic sensitivity as discussed in Section 2.5. For NV ensemble fabrication, the main physical parameters that affect sensitivity are NV density, $[NV^-]/[N]$ conversion efficiency, carbon isotope purity and strain caused by lattice damage.

One method of forming near-surface NV ensembles is by ion-implantation and annealing. High-energy nitrogen ions are bombarded onto a high-purity diamond substrate. The nitrogen ions knock out carbons and form vacancy trails as they embed into the diamond lattice. Subsequent high-temperature vacuum annealing (>800 C) mobilizes vacancies and allows NV centers to form. Nitrogen ion implantation, while a capable technique especially for forming near-surface single NVs for quantum information applications, has several limitations. First, the lattice damage incurred by implanting high-energy nitrogen ions is not fully healed by high-temperature annealing, leading to inhomogenous lattice strain environments that compromise NV spin coherence and charge state stability[48, 46]. Additionally, using a single ion energy results in an inhomogenous, typically Gaussian distribution of nitrogen at the surface of the diamond, and thus an inhomogenous NV density in the final sensing layer. A related scheme relies on high-energy irradiation of nitrogen-rich diamond substrates. In Ref. [8], several diamond substrates with varying intrinsic [N] were subject to either electron or proton irradiation. The best $[NV^-]/[N]$ ratio observed was approximately 10% with 10 ppm NV density and $T_2^* \approx 66$ ns, limited by lattice damage. While the 10% conversion ratio is favorable to limit dipolar interactions between NVs and substitutional nitrogen spins, the low T_2^* significantly limits the dc magnetic sensitivity. Also, high-energy irradiation forms vacancies and thus NVs throughout the bulk of the diamond chip, increasing NV ensemble thickness and limiting the sensitivity for dipole field imaging.

In summary, the NV ensemble formation schemes discussed so far are able to form high densities of NVs with reasonable $[NV^-]/[N]$ conversion ratios, but the spin coherence of near-surface ensembles formed by nitrogen implantation are limited by lattice damage and the NV ensembles formed by high energy irradiation are distributed throughout a large

volume, compromising imaging sensitivity. For these reasons, alternative schemes to high-energy ion implantation or irradiation to form high-sensitivity near-surface NV ensembles for magnetic imaging are of interest.

The method of NV ensemble fabrication used in this work was first demonstrated by the Fu group in Ref. [24]. CVD of a ^{12}C isotope-purified layer of diamond with nitrogen-doping is performed on a commercial substrate, followed by helium ion-implantation and subsequent annealing. This fabrication scheme boasts several advantages to nitrogen implantation. The thin-layer CVD growth allows for carbon isotope purification: in Ref. [24], 99.9% ^{12}C was used, while in this work the isotope purity was increased to 99.999% ^{12}C. Additionally, nitrogen is doped in during the thin-film growth, allowing nitrogen to incorporate into the diamond lattice with relatively low strain compared to ion implantation. The helium ion implantation used to form vacancies is much shallower than electron irradiation, allowing for vacancies to be formed in a thin, near-surface layer while limiting lattice damage compared to heavier ions. Lattice damage would be further decreased by using hydrogen implantation, but the implanted hydrogen's electron spins would add an additional source of spin noise to the NV ensemble.

Using the CVD growth, N-doping, He^+ implantation method, three approximately 100 µm thick diamond samples were prepared, E1419, E1420 and E1421. The relatively-thin thickness of the diamond substrate is used to enable imaging through the back of the diamond and will be discussed in the next section. Growth collaborators at Keio University and AIST in Japan grew 150 nm of ^{15}N doped, isotope-purified (99.999% ^{12}C) layers by chemical vapor deposition on electronic-grade (ppb [N]) diamond substrates from Element Six. After growth, collaborators at Pacific Northwest National Laboratory (PNNL) performed 25 keV helium ion implantation in approximately 10 µm squares with varying doses (1e10, 1e11, 1e12 & 1e13 ions/cm^{-2}), see Figure 4.2(a). The diamonds were then annealed at 900 C for 2 hours. The squares were imaged using confocal microscopy to measure the NV density in each square by comparing the emitted fluorescence to a single NV center. Additionally, the CW ODMR dc magnetic field sensitivity was measured. Based on this dose test, a dose of 5e11 ions/cm^2 was chosen to optimize sensitivity and the samples were blanket implanted in a commercial semiconductor processing facility. The blanket implantation was followed

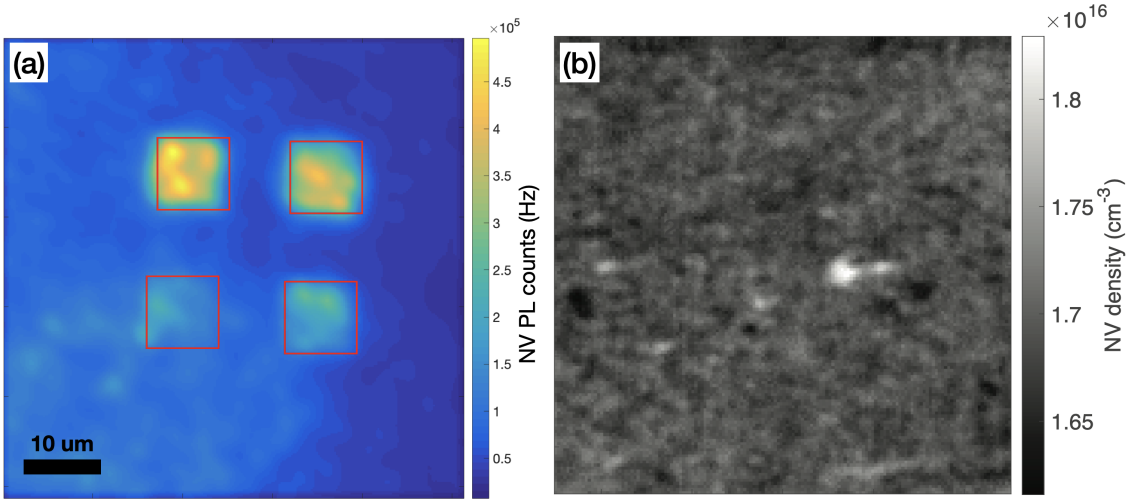

Figure 4.2: **Helium implantation into N-doped isotope purified CVD diamond.** (a) Four squares on sample E1419 with increasing helium ion implantation dose (25 keV, 1e10-1e13 ions/cm^{-2}) are imaged after CVD-N-doped growth, helium ion implantation and vacuum annealing. CW ODMR sensitivity was measured for each square, and an optimal helium ion implantation dose was selected. (b) Image of NV$^-$ density after blanket helium ion implantation. NV PL per confocal spot was compared to single NV PL at the same excitation laser power to measure NV density. An average density of approximately 0.1 ppm is measured for the three samples fabricated in this work.

by a vacuum anneal at 900 ˚ for 2 hours to form NV and an anneal in O_2 at 425 ˚ for 2 hours for charge state stabilization [24], see Figure 4.2(b). The resulting ensembles have NV densities of approximately 1.7×10^{16} cm^{-3} (0.1 ppm). Based on the results of Ref [24, 49], the [N] concentration is estimated to be about 1 ppm and the [NV$^-$]/[N] conversion ratios is estimated to be approximately 10%, comparable to the favorable conversion ratios seen in other methods.

A final alternative NV ensemble fabrication scheme relies on preferential orientation via plasma-enhanced CVD (PECVD) growth with nitrogen doping [44]. When a nitrogen incorporates into the diamond lattice during PECVD, it becomes favorable for a vacancy

to sit directly above it, allowing for preferential formation of the [111] NV orientation. Preferential orientation can be advantageous for certain magnetometry applications when the Zeeman projection along only one NV orientation is desired. Because only one NV orientation is present, the ODMR contrast in preferentially oriented NV samples is higher because the other NV orientations are not contributing a fluorescence background. This can result in higher sensitivity for scalar magnetometry applications.

Because only one NV orientation is present, vector magnetometry cannot be performed in the straightforward manner described later in Section 4.5 for diamonds with an equal concentration of the four NV orientations. That said, vector field magnetic field map reconstruction is possible from the map of a single component in a source-less region [50]. This Fourier-decomposition based total field reconstruction map is of highest fidelity when the component of the field measured is perpendicular to the plane of the map, which can be utilized with [111] preferentially oriented NV ensembles.

Another drawback of preferentially oriented samples is the relatively low $[NV^-]/[N]$ conversion ratios due to the low probability of forming a [111] NV, usually around 0.2% [44]. These low conversion ratios contribute to a low spin coherence time T_2. T_2 was found to increase after high-temperature annealing% [44], suggesting that paramagnetic impurities are formed during PECVD growth and can be annealed out, increasing spin coherence. However, high-temperature annealing mobilizes vacancies and creates NVs in non-[111] orientations, diluting the preferential orientation. Further studies to optimize PECVD growth to minimize these paramagnetic impurities that are introduced during sample growth is warranted.

One preferentially oriented [111] diamond sample was supplied by the Jelezko group at Ulm University, with 150 nm [111] NV ensemble with approximately 10 ppm NV. The CW ODMR contrast saturates around 25%, see Fig. 4.3(a), with approximately 1.5 MHz minimum PODMR linewidths measured in Fig. 4.3(b). The best measured ODMR sensitivity for the preferentially oriented sample was 250 nT $Hz^{-1/2}$ and did not compare favorably to the helium-implantation samples (with best sensitivities closer to 50 nT $Hz^{-1/2}$), so the helium-implantation samples were used as the main imaging samples for the magnetic particle imaging in this thesis.

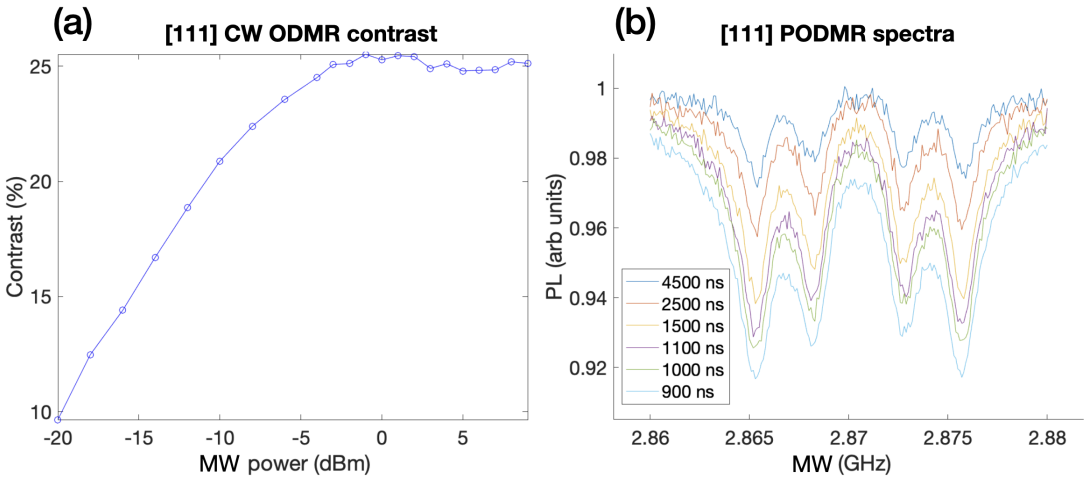

Figure 4.3: **Preferentially oriented sample ODMR.** (a) CW ODMR contrast versus MW power for a [111] oriented NV ensemble. The ODMR contrast saturates near the ISC branching ratio limit due to the elimination of fluorescence noise from off-resonant NV orientations. (b) Pulsed ODMR spectra with varying Rabi frequency, labelled by π-pulse time in the inset. The minimum PODMR linewidth was measured to be about 1.5 MHz.

4.3 magPI experimental set up schematic

The experimental platform used in this work is designed to fully utilize the sensitivity of the fabricated diamond sensors and enable wide-field magnetic particle imaging in a multitude of experimental conditions such as dry samples, samples in aqueous environments, imaging through thin diamond samples, total-internal-reflection (TIR) excitation, excitation via air and oil-immersion objective lenses, with applied external magnetic field, pulsed optical excitation and a variety of microwave control methods.

4.3.1 Optical setup

The magPI optical set up schematic is shown in Figure 4.4. A 532 nm laser (LaserQuantum opus 2W) is used to optically excite the NV ensemble. An acousto-optical-modulator (AOM) (Gooch&Housego) diffracts the laser beam. The first-order diffracted beam is spatially filtered with an iris (not shown) and is used as the excitation laser beam in the rest of the excitation path. Two lenses L1 (AC254-50-A) and L2 (AC254-150-A) in a telescope configuration form a beam expander with magnification of 3. By magnifying the beam at this stage, the illumination area on the sample can be increased. The beam then reflects off a mirror and passes through L3 which focuses the light to the back-focal-plane (BFP) of the objective lens. L3 (AC254-250-A) and its neighboring mirror are put on a Z-stage. By translating the stage parallel to the direction of the incident beam, the beam is translated off-optical-axis at the objective lens, enabling total-internal-reflection (TIR) excitation, see Figure 4.5. The excitation light then reflects off a dichroic mirror (DM) and exits the objective lens collimated. The collimated beam excites NVs in the diamond. The emitted fluorescence is collected by the objective lens and collimated. The collected light passes through the DM and is spectrally filtered by a 640 nm long pass filter. A tube lens focuses the light onto a sCMOS camera (Hamamatsu OrcaFlash). The camera is chosen for its relatively-high frame rate (minimum exposure 4 ms), large sensor size, and low dark counts (<100 cts/s).

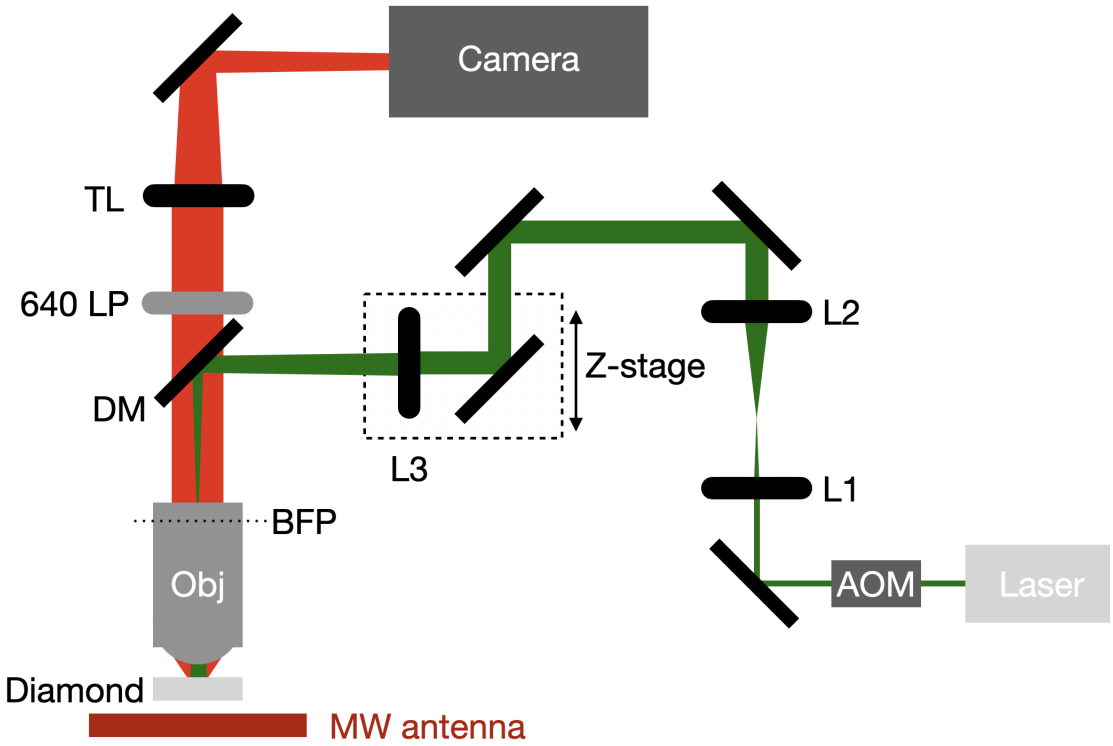

Figure 4.4: **magPI optical schematic.** 532 nm light from a laser passes through an acousto-optic modulator (AOM). The laser beam is expanded by lenses L1 and L2 and reflects off a mirror and passes through lens L3, a lens used to focus the beam in the back focal plane (BFP) of the objective (typically 2 mm from the back aperture for Nikon objectives). The excitation light reflects off a dichroic mirror (DM) and excites the NVs with a collimated beam. As the laser light excites the diamond sample containing NVs, the emitted fluorescence is collected by the objective lens (Obj) and passes through the DM. The light is filtered using a 640 nm long pass (LP) filter, and focused by a tube lens (TL) onto a sCMOS camera.

Total-internal-reflection excitation

In sensing applications where the sensing target is brought within a micron of the diamond sensing surface, it can be advantageous to image through the back of the diamond and use total-internal-reflection (TIR) excitation at the diamond-target interface to minimize excitation laser flux into the sensing target. This can be readily accomplished by translating the excitation beam away from the optical axis defined by the objective lens. In this way, the excitation beam exits the objective at an angle. This angle can be increased until TIR is achieved at the diamond-target interface. Figure 4.5 demonstrates the principle of TIR with DNA-tethered magnetic particles attached to the diamond surface in a fluid-chamber.

4.3.2 Microwave setup

As introduced in Section 2.2.3, MW excitation drives transitions between NV electron spin states. The MW setup used in the magPI platform is designed to apply multi-toned MW pulses simultaneously to the NV ensemble to drive mutliple electron spin transitions and hyperfine transitions simultaneously. This is accomplished by combining the MW signals from three generators, a WindFreak SynthNV (2-channel), a Rhode&Shwarz SMIQ03A and HP Agilent 8644B. Two tones are combined (Minicircuits ZX10-2-42-S+) and switched (Minicircuits ZFSWA2-63DR+) with the switch digital control accomplished by a SpinCore PulseBlaster 100 MHz. The switched two-tone signals are again combined and form the LO of an RF mixer (Pasternack SFM2018) with DigiKey function generator supplying the IF to split the center MW tone into two tones split by 3.05 MHz that can drive both ^{15}NV hyperfine resonances simultaneously [10] and produce one combined resonance for each electron spin transition, see Figure 2.9. The MW signal is then amplified (Minicircuits ZHL-16W-43-S+), passed through a circulator (Fairview SFC2040A) to protect the upstream components from reflections then sent to a broadband MW antenna [51] with transmission resonance at the NV zero-field-splitting D which transmits a z-polarized MW field to the NV spins.

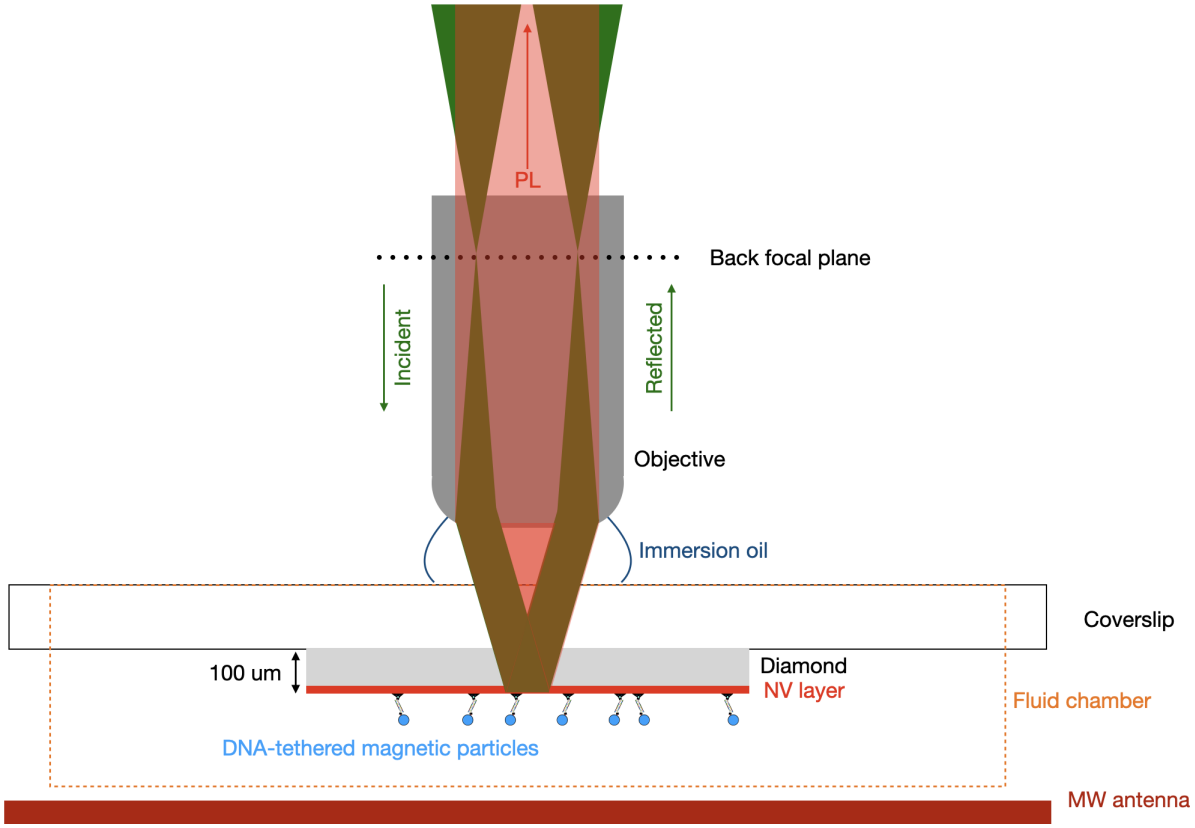

Figure 4.5: **Through-the-lens total-internal-reflection excitation.** (schematic not to scale) Laser excitation is focused to the back-focal-plane of an objective lens and translated off axis in order to achieve total-internal-reflection at the diamond-fluid interface. The emitted fluorescence is collected by the objective lens as normal.

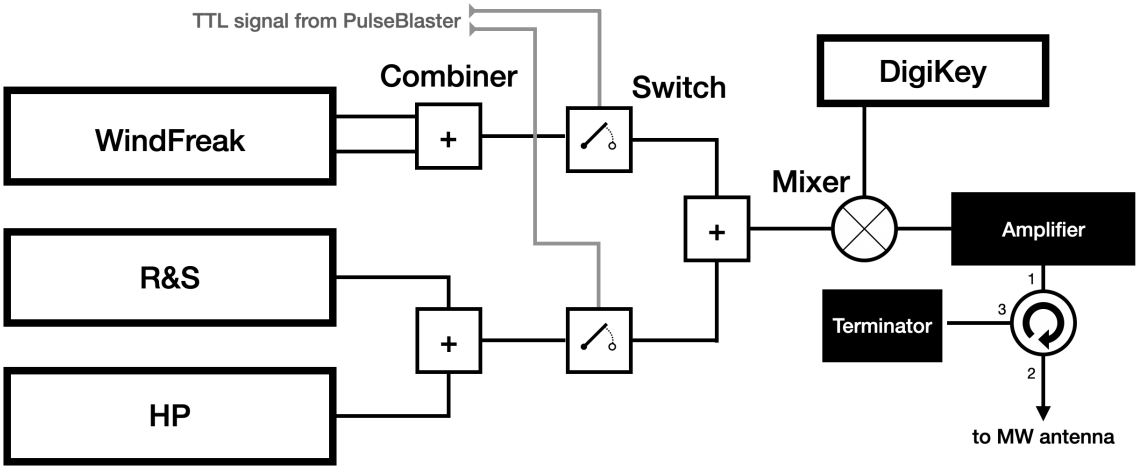

Figure 4.6: **Microwave schematic.** The MW signals from three generators are gated with MW switches and combined. A separate function generator feeds an IF signal into an RF mixer to split the center MW tone into two tones that can drive both NV hyperfine resonances simultaneously. The signal is then amplified, passed through a circulator then sent to a broadband MW antenna.

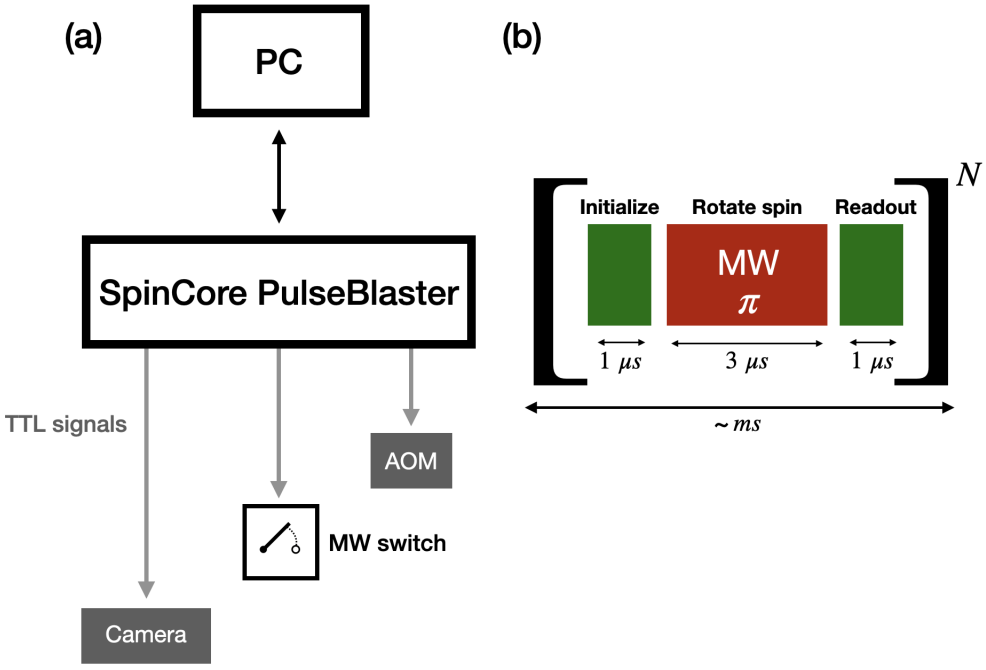

Figure 4.7: **Pulse control compatible with camera imaging.** (a) A SpinCore PulseBlaster TTL generator interfaces with a PC to control the laser pulses via an AOM, MW pulses via a MW switch, and triggers image acquisition directly on a sCMOS camera. (b) Optical and MW pulses (µs scale) are applied repeatedly to fill a millisecond scale exposure.

4.3.3 Pulsed excitation with wide-field imaging

For the Ramsey or Pulsed ODMR magnetometry schemes described in Chapter 2, pulsed optical and MW signals are necessary for NV electron spin manipulation and readout. In the magPI platform, these pulses are generated by using a SpinCore PulseBlaster digital pulse generator that controls the laser pulses via an AOM, MW pulses via MW switches, and triggers image acquisition directly on a sCMOS camera, see Figure 4.7(a). A Python package to independently program PulseBlaster channels was written and is available on GitHub.

Typical optical pulses used for spin initialization and readout are about 1 µs and MW pulses are about 3 µs. The sCMOS camera used in this work has a minimum exposure time of 4 ms. In order to measure with the mismatch in pulse time scales and camera exposure times, roughly one thousand identical optical and MW pulses are applied repeatedly to fill a sCMOS exposure, see Figure 4.7(b). In this way, the PL image collected by one camera exposure measures the effect of one MW pulse with a given MW frequency. To measure the full ODMR curve, the MW frequency is stepped, and a PL image is collected for each MW frequency. The resulting hyperspectral image contains an ODMR spectrum at each camera pixel.

4.4 Static wide-field magnetic imaging using ODMR

Wide-field magnetic imaging is enabled by measuring the NV ODMR across an imaging field of view. As in Figure 4.8, an image of the resonant frequency of the ODMR curve produces a map of local magnetic field projection along the NV symmetry axis. The magPI platform uses a camera, a wide-field illumination area and a microwave antenna to simultaneously interrogate a large area (approx 50x50 μm^2) of NVs in the diamond sensor. This can be done with CW ODMR, PODMR or even Ramsey sensing. The field-of-view is limited by the laser illumination area. Larger illumination areas require higher optical powers, which can be limited by high cost.

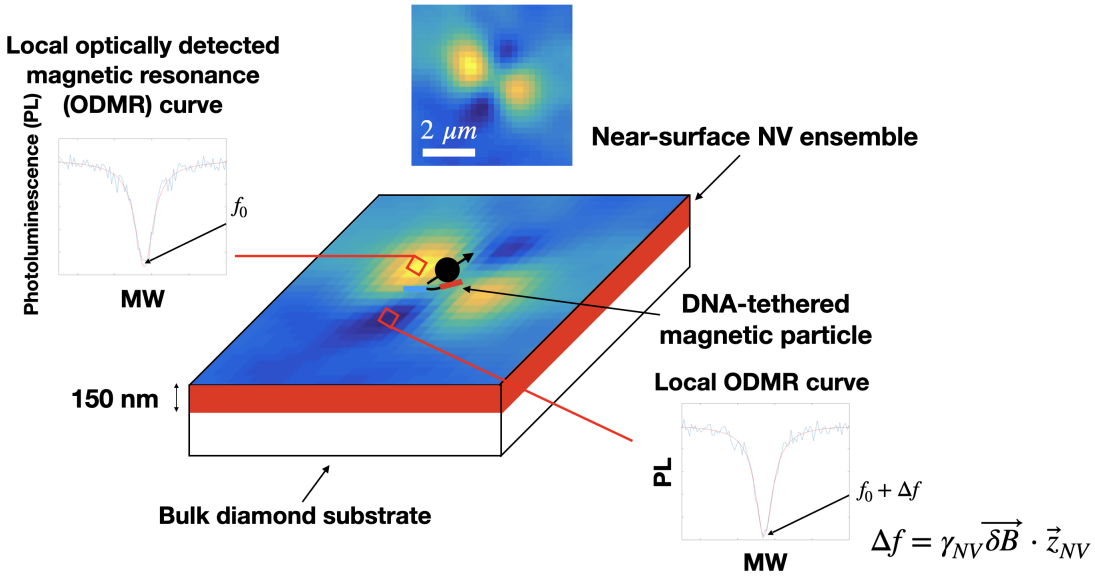

Figure 4.8: **Wide-field magnetic imaging.** A diamond with a near-surface ensemble of NV centers enables wide-field magnetic imaging of a DNA-tethered magnetic particle by measuring NV ODMR across an imaging field of view. Changes in the local ODMR frequency is given by the field $\delta\vec{B}$ produced by the magnetic particle. Making an image of the ODMR frequency results in a map of magnetic field projection along the NV symmetry axis.

4.5 Vector magnetometry with NV ensembles

In diamond, there are four possible crystallographic orientations of NV centers denoted by [111], [$\bar{1}\bar{1}$1], [$\bar{1}$1$\bar{1}$], and [1$\bar{1}\bar{1}$]. The four NV orientations can be parameterized by four unit vectors $\vec{o}_i$:

$$\vec{o}_1 = \frac{1}{\sqrt{3}}(1,1,1), \tag{4.3}$$

$$\vec{o}_2 = \frac{1}{\sqrt{3}}(-1,-1,1), \tag{4.4}$$

$$\vec{o}_3 = \frac{1}{\sqrt{3}}(-1,1,-1), \tag{4.5}$$

$$\vec{o}_4 = \frac{1}{\sqrt{3}}(1,-1,-1). \tag{4.6}$$

With an arbitrarily oriented magnetic field $\vec{B}$, the four Zeeman projections $Z_i = 2\gamma_{NV}\vec{o}_i \cdot \vec{B}$ are measured by measuring the full PODMR spectrum comprising eight resonances: two of each $|0\rangle \leftrightarrow |\pm 1\rangle$ transition for each of four orientations as seen in Figure 4.9.

In the magPI platform, because of the ^{15}NV hyperfine-mixed driving, each hyperfine ODMR doublet becomes a triplet with additional sidebands. To account for these extra sidebands, the normalized ODMR spectrum is fit to a multi-dip Lorentzian function:

$$L(a, b_{jk}, g_{jk}, Z_j, D, M_j, A_{hyp}, f) = a - \sum_{j=1}^{8}\sum_{k=0}^{2} b_{jk}\frac{g_{jk}^2}{(f-(D+M_j+Z_j \pm kA_{hyp}))^2 + g_{jk}^2} \tag{4.7}$$

where a is the off-resonant vertical offset, b_{jk} is the contrast for each ODMR dip, g_{jk} is HWHM linewidth for each ODMR dip, D is the zero-field-splitting, A_{hyp} is the diagonalized hyperfine interaction strength (approx 3.05 MHz), M_j is the on-axis strain coefficient, and Z_j is the Zeeman projection along each NV orientation. Note that $Z_j|_{j<4} = Z_j$ and $Z_j|_{j>4} = -Z_{5-j}$ and $M_j|_{j>4}=M_{(5-j)}$ so that there are four total of each quantity Z_i and M_i, one for each NV orientation. Using Equation 4.7, the ODMR spectrum is fit and the four Zeeman projections are extracted.

In order to transform the Zeeman projections into the lab frame, a linear mapping from

Z_i to lab frame is used:

$$\begin{pmatrix} B_x \\ B_y \\ B_z \end{pmatrix} = \frac{\sqrt{3}}{8} \begin{pmatrix} 1 & -1 & -1 & 1 \\ 1 & -1 & 1 & -1 \\ 1 & 1 & -1 & -1 \end{pmatrix} \begin{pmatrix} Z_1 \\ Z_2 \\ Z_3 \\ Z_4 \end{pmatrix}. \tag{4.8}$$

This method is fully compatible with the static magnetic field imaging protocol described in section 4.4. The full PODMR spectrum is measured in wide-field, and four Zeeman projection maps are constructed after fitting the spectrum at each camera pixel. Using Equation 4.8, the Zeeman maps are converted to magnetic field maps with respect to lab-frame coordinates. Wide-field vector magnetometry is used in Chapter 6 to image the magnetic field produced by ferromagnetic nanoparticles under differing applied field magnitudes and directions.

4.6 Dipole model of magnetic particle images

To extract magnetic dipole moment orientation from magPI images, a six-parameter dipole model is used. A point dipole with magnetic moment $\vec{m}$ is at a position $\vec{r}$ above a diamond sensor. The magnetic field at a uniform grid of NV centers throughout a 150 nm layer on the top surface of the diamond sensor spaced according to NV density ρ_{NV} is calculated using Equation 4.1. The average NV-NV spacing $\langle d \rangle_{NV}$ is given by $\rho_{NV} \langle d \rangle_{NV}^3 = 1$. With 10^{16} cm^{-3} NV density, $\langle d \rangle_{NV} \approx 45$ nm, so three NV layers are simulated in a 150 nm thick ensemble. The signal at each NV is then Gaussian filtered with σ given by the optical resolution of the system, which is close to 500 nm in the magPI platform. The contributions from NVs throughout the three vertical layers are summed together, then the magnetic fields at each NV are then binned to camera pixels, typically 560 nm.

This magnetic field imaging system is limited in the magnetic gradient it can image due to inhomogenous broadening of NVs within one camera pixel. Multiple NVs contribute to the ODMR signal in a single pixel, so if there is a large magnetic field gradient across the pixel the individual ODMR signals do not constructively sum together, see Figure 4.10(b). Thus, in the dipole model, after the the gradient of the dipole magnetic field along each

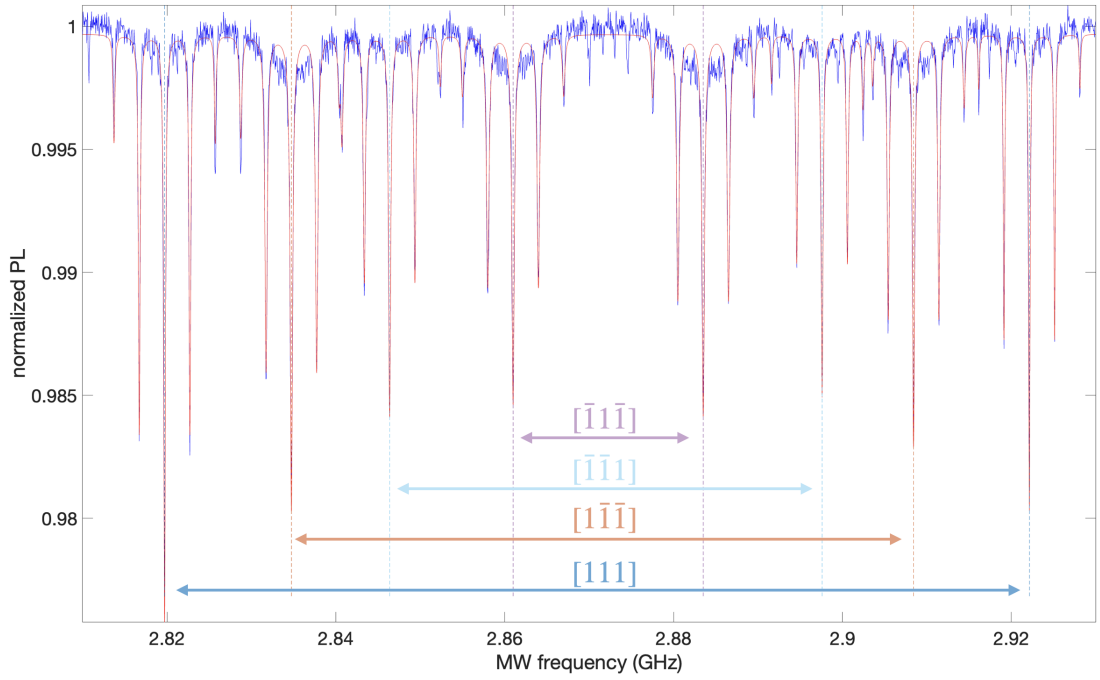

Figure 4.9: **ODMR for vector magnetometry.** Eight resonances associated with four NV crystallographic orientations are measured. By transforming the Zeeman projections along each orientation, the vector magnetic field in the lab frame can be measured. Each individual resonance is associated with approximately 5 dips due to simultaneous hyperfine driving which promotes the ^{15}NV hyperfine doublet into a triplet. Due to sidebands in the RF mixing, higher order resonance sidebands are observed. Each resonance is fit to five Lorentzian dips.

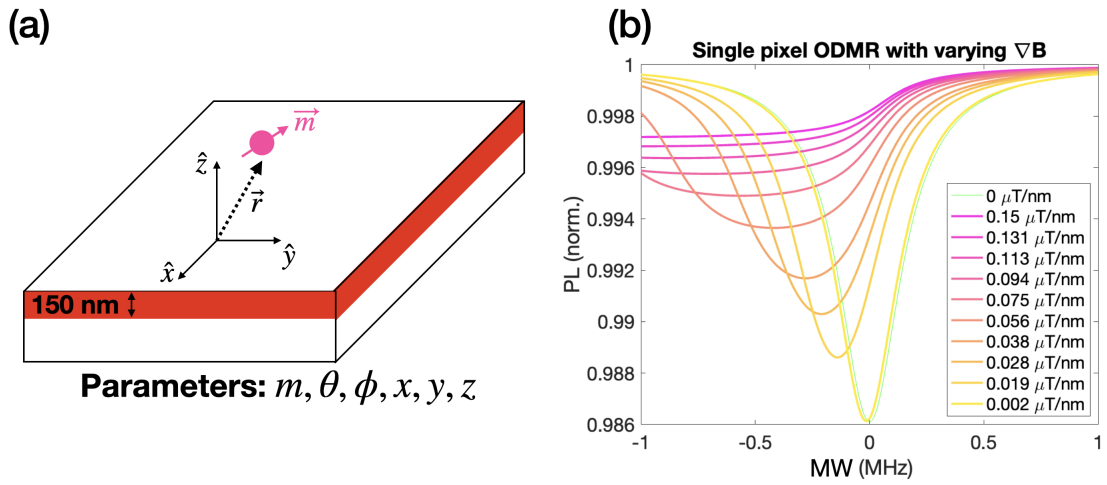

Figure 4.10: **magPI dipole model and magnetic field gradient induced inhomogenous broadening.** (a) Schematic of dipole model used to simulate magnetic particle images. Six parameters are used in the model: magnetic dipole moment magnitude, magnetic moment polar and azimuthal angles, and three dimensional position vector. (b) Magnetic field gradients inhomogenously broaden the ODMR curve in a single pixel, limiting the range of magnetic field gradients that can be measured.

NV orientation in a single pixel is calculated, pixels with magnetic field gradient higher than a threshold value are nulled. Using a least-squares algorithm, this model is able to fit magPI dipole images and extract the magnetic moment vector. This is used in Chapter 5 to measure the dynamic reorientation of a DNA-tethered magnetic particle, and in Chapter 6 to measure the magnetic moment vector of DNA-tethered magnetic nanoparticles in a nano-mechanical torque balance.

4.7 Ferromagnetic particle types

Several types of ferromagnetic particles with bio-compatible surface coatings for use in the magPI platform are commercially available, see Figure 4.11. Depending on the application, different particles can be chosen. Above the single domain limit, magnetic moment scales linearly with particle volume. However, as particle diameter increases, distance to the sensor

increases resulting in an approximately constant magnetic field at the sensor with particle diameter.

Single domain ferromagnets have small magnetic moments (around 10^{-18} Am^2) and are on the order of 10 nm [52, 53], requiring extraordinary sensitivity to detect. Also, due to the high moment to size ratio, single domain magnets tend to aggregate, requiring specific techniques to separate individual particles. Additionally, the roughly 10 nm single domain magnet sizes are always less than optical resolution, requiring dark-field or scanning-electron-microscopy (SEM) to localize. Single domain particles are used in the nano-mechanical torque balance in Chapter 6.

Multi-domain ferromagnetic particles can have moderate sizes (50-4000 nm), making them ideal for optical microscopy as well as compatible with magnetic imaging. However, in magnetic imaging care must be taken to make sure the applied external field is not larger than the coercive field of the magnet, else the magnet will behave as a paramagnetic particle, meaning the magnetic moment of the particle will align parallel to the applied magnetic field and the moment magnitude will scale with the amplitude of the applied field. Multi-domain particles are used in the dynamic reorientation experiment in Chapter 5 with an applied field lower than the coercive field.

Coated multi-domain ferromagnetic particles can have large sizes (500-10000 nm) and very large magnetic moments (10^{-14} Am^2), making them ideal for proof-of-principle experiments where localizing single particles with high magnetic field signal is necessary. Individual coated particles are straightforward to separate from aggregates and can easily confirmed to be single particles via bright-field microscopy. The magPI platform aims to measure the reorientation of magnetic particles caused by biological mechanisms. The torques exerted by biological systems are typically on the order of pN nm. A typical coated ferromagnetic particle with moment 10^{-14} Am^2 in a 1 mT field would experience a 10^4 pN nm torque, dominating the bio-orientation torque. For this reason, bio-orientation cannot be readily imaged using coated ferromagnetic nanoparticles.

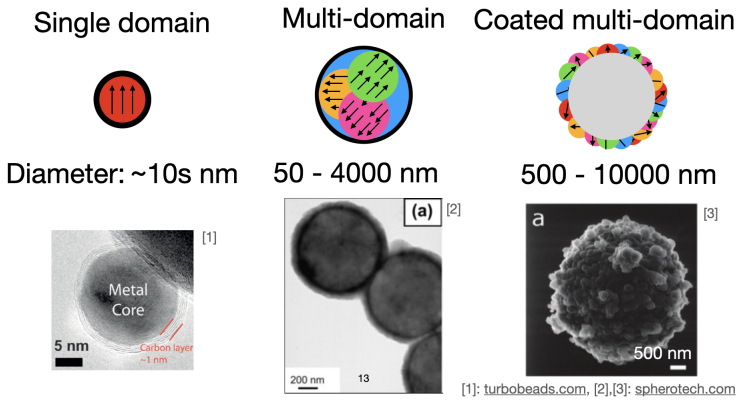

Figure 4.11: **Ferromagnetic particle types.** Three particle types of varying sizes and magnetic character. Transmission electron microscopy (TEM) and scanning electron microscopy (SEM) images provided by the manufacturers are shown.

4.7.1 Application: wide-field imaging of magnetic domains in a thin-film ferromagnet[1]

The near-surface NV ensemble sensing platform described here is also favorable to image condensed matter systems because of the ability to bring the sensor within several microns of the sensing target. In Ref [2], a thin-film ferromagnet (Ta(5 nm)/$Co_{20}Fe_{60}B_{20}$(1 nm)/ Ta(0.08 nm)/MgO(2 nm)/Ta(5 nm) material stack that is grown on a Si/SiO_2 substrate) is placed in close proximity to a diamond sensor, and two complementary imaging modalities are used to image the magnetic material.

The first imaging modality relies on the magneto-optical Kerr effect (MOKE). MOKE images magnetization in a material by measuring the magnetization-induced Kerr rotation of an optical probe beam. The second imaging modality relies on NV ensembles to image the magnetic field produced by the magnetization in the material. In this experiment, MOKE and NV imaging are correlated to image magnetic domains in the ferromagnetic

[1]Section 4.7.1 is a part of work that has been published as:
Till Lenz, Georgios Chatzidrosos, Zhiyuan Wang, Lykourgos Bougas, Yannick Dumeige, Arne Wickenbrock, Nico Kerber, Jakub Zázvorka, Fabian Kammerbauer, Mathias Kläui, **Zeeshawn Kazi**, Kai-Mei C. Fu, Kohei M. Itoh, Hideyuki Watanabe, and Dmitry Budker. Imaging Topological Spin Structures Using Light-Polarization and Magnetic Microscopy. Physical Review Applied, **15**, 024040.

https://doi.org/10.1103/PhysRevApplied.15.024040

material stack, and the magnetic field those domains produce. The reduced spatial resolution in the NV imaging compared to MOKE is attributed to the several-micron standoff distance between the thin-film and the diamond sensor. These complementary modalities can be used to characterize and study ferromagnetic materials and observe effects such as domain boundary and skyrmion formation with magnetization and magnetic field imaging simultaneously in a wide-field configuration.

Summary

In this chapter, a wide-field magnetic particle imaging (maPI) platform based on a near-surface ensemble of diamond NV centers is discussed in detail. This chapter discusses the careful engineering of the sensing platform to enable imaging of the magnetic field produced by individual magnetic nanoparticles, including diamond sensor fabrication and the experimental set up required to perform high sensitivity imaging. In the next chapter, this platform is used with a novel quantum sensing technique to dynamically image the orientation of a DNA-tethered magnetic nanoparticle. In the following chapter, the magPI platform is used to measure the static orientation of a DNA-tethered magnetic nanoparticle and an external applied field in a nano-mechanical torque balance to measure the bend stiffness of single DNA molecules.

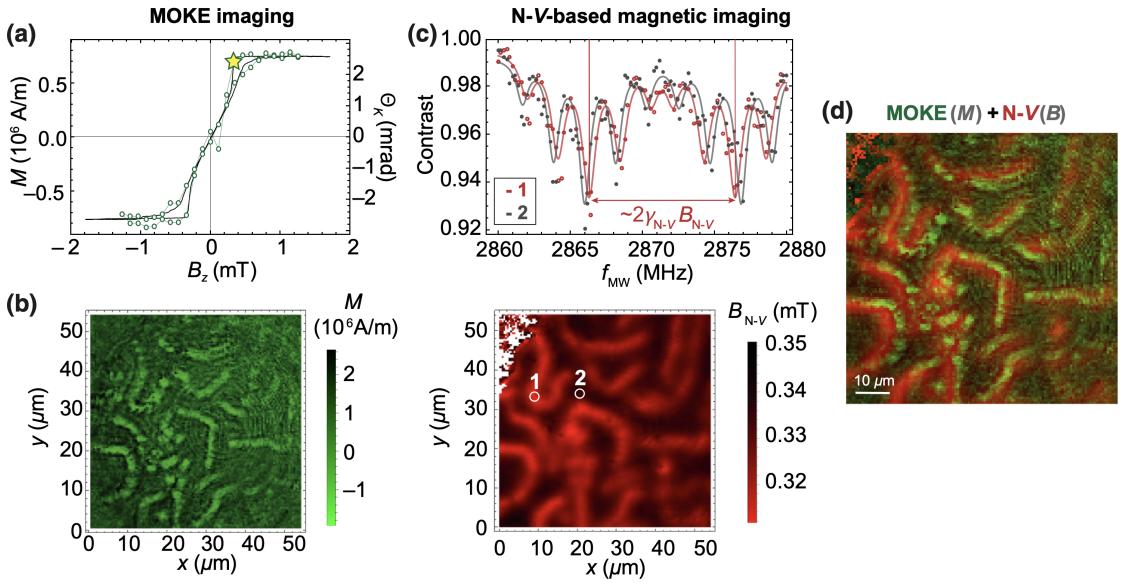

Figure 4.12: **Correlated magnetization and magnetic field imaging of a thin-film ferromagnet.** (a) Out-of-plane magnetization curve of a magnetic sample using a magneto-optical-Kerr-effect (MOKE) system and a commercial magnetization measurement system. The starred point is the applied field at which the images in (b) and (c) are obtained. (b) Magnetization map of the thin-film ferromagnet at an applied field of 0.329 mT. (c) NV ODMR at 0.329 mT applied field at two different positions on the sensor showing the effect of changing magnetic field on ODMR splitting. A map of fitted sample field is shown below. (d) Correlated MOKE and NV ODMR images showing alignment of magnetic domains with magnetic field maps. Figure originally published in Ref. [2]

Chapter 5

DYNAMIC MAGNETIC FIELD IMAGING WITH MAGPI FOR BIO-MECHANICAL ORIENTATION MEASUREMENTS

Wide-field magnetometry can be realized by imaging the optically-detected magnetic resonance of diamond nitrogen vacancy (NV) center ensembles. However, NV ensemble inhomogeneities significantly limit the magnetic-field sensitivity of these measurements. In this chapter, we demonstrate a novel microwave control technique called double-double quantum (DDQ) driving to facilitate wide-field magnetic imaging of dynamic magnetic fields at a micron scale. DDQ imaging employs four-tone microwave pulses to suppress inhomogeneity-induced variations of the NV resonance response. As a proof-of-principle, we use the DDQ technique to image the reorientation of a ferromagnetic particle tethered by a single DNA molecule under the influence of an applied fluid flow with ms-scale frame rates. This experiment is the first demonstration of dynamic magnetic microscopy using the diamond NV platform, demonstrating the efficacy of the diamond NV ensemble system in high-frame-rate magnetic microscopy, as well as single-molecule biophysics applications.[1]

5.1 Introduction

In NV ensemble ODMR, magnetic fields can be imaged by characterizing the photoluminescence of optically-excited NV centers after probing the NV spin ground states with microwave (MW) π-pulses. The resonant MW depends on magnetic field because of the Zeeman splitting of the $|m_s = \pm 1\rangle$ NV electronic spin states. However, in addition to sensitivity to magnetic field, the resonances are also perturbed by inhomogeneities in electric field, temperature, and crystal strain [54, 55, 21, 56]. Due to the symmetry of the

[1] A version of this chapter has been published as:
Zeeshawn Kazi, Isaac M. Shelby, Hideyuki Watanabe, Kohei M. Itoh, Vaithiyalingam Shutthanandan, Paul A. Wiggins, and Kai-Mei C. Fu 2021. Wide-Field Dynamic Magnetic Microscopy Using Double-Double Quantum Driving of a Diamond Defect Ensemble. Physical Review Applied, **15**, 054032.

https://doi.org/10.1103/PhysRevApplied.15.054032

NV center, these non-magnetic perturbations affect the two NV electron spin resonances ($|m_s = 0\rangle \leftrightarrow |m_s = \pm 1\rangle$) in the same way and can be eliminated by characterizing both resonances [14, 13].

5.2 Dynamic magnetic microscopy with diamond NV ensembles

For wide-field magnetic imaging of time-varying fields, the full characterization of the NV resonance curves is too slow to capture the magnetic-field dynamics in many applications. In these dynamic applications, shifts of one resonance curve can instead be mapped to changes in emitted NV PL intensity by applying single-frequency MW excitation [57, 58, 59]. This "single-quantum" (SQ) imaging modality enables partial reconstruction of the local magnetic field with a higher frame-rate than the "gold-standard" frequency scanning modality.

The double-quantum (DQ) modality, which drives both NV electron spin transitions simultaneously by applying a two-tone MW pulse, eliminates pixel-to-pixel non-magnetic perturbations of the transition resonance frequencies [14, 13]. However, variations of the shape of the resonance curve also cause changes in the emitted PL intensity and therefore generate spurious contrast which limits the magnetic sensitivity. These variations arise from inhomogeneities in NV and other paramagnetic spin densities as well as external fields [25], and as shown in this work, can severely limit the utility of the DQ modality for wide-field imaging applications. By expanding to a four-tone DDQ driving scheme, we suppress anomalous contrast due to resonance-curve-shape variations pixel-by-pixel across the field of view. This enables high-frame-rate imaging of time-dependent magnetic fields. We first demonstrate the SQ, DQ, and DDQ imaging modalities by imaging static fields, and show the DDQ signal is linearly proportional to the magnetic field projection along the NV symmetry axis.

First, the magPI platform is used to image the static dipolar magnetic field produced by a 50 nm dextran coated $CoFe_2O_4$ ferromagnetic nanoparticle (micromod Partikeltechnologie) deposited and dried onto the diamond sensor surface. These bio-compatible particles produce nano-scale magnetic fields which lie in the dynamic range of the NV sensing ensemble defined by $\delta\nu$ of the resonance curves. For other imaging applications, the sensor

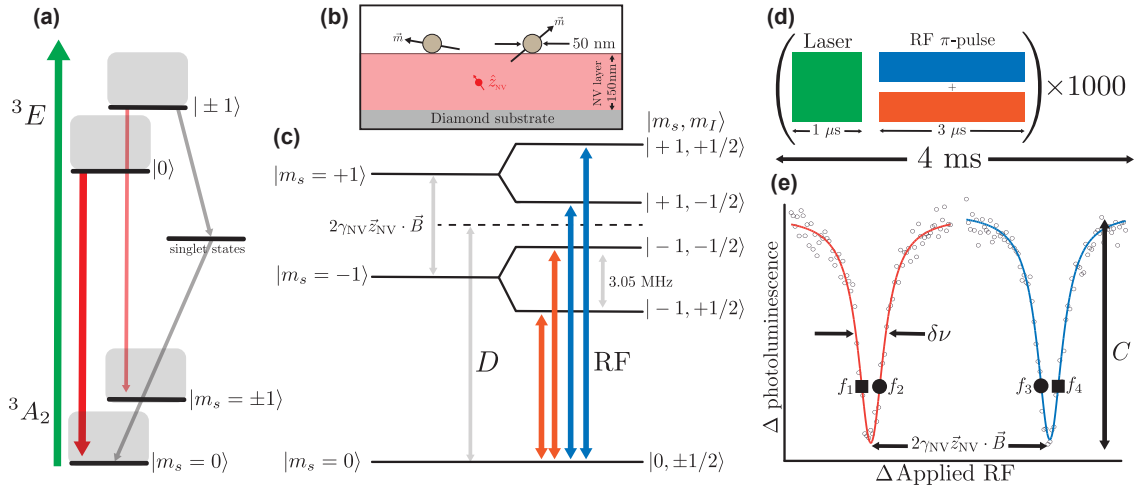

Figure 5.1: Wide-field pulsed magnetic imaging using an NV ensemble. (a) NV electronic energy level diagram showing the ground, excited spin states ($|m_s = 0\rangle$,$|m_s = \pm 1\rangle$), singlet states, optical excitation (green arrow), emitted photoluminescence (red arrows), and spin-selective, non-radiative inter-system-crossing (gray arrows). (b) Schematic showing 50 nm ferromagnetic nanoparticles adhered to the diamond surface. The magnetic moments of the particles are oriented randomly. The 150 nm NV layer (pink) is fabricated on top of the diamond substrate (gray), and a single NV pointed along the [111] orientation is shown (red). (c) NV ground state energy level diagram showing the zero-field splitting (D), Zeeman splitting of the $|m_s = \pm 1\rangle$ states ($2\gamma_{NV}\hat{z}_{NV}\cdot\vec{B}$), and ^{15}N-NV hyperfine splitting (3.05 MHz). RF excitation (orange and blue arrows) rotates the NV spin between the $|m_s = 0\rangle$ and $|m_s = \pm 1\rangle$ states. Two-tone RF excitation is simultaneously driven over the two ^{15}N-NV hyperfine transitions to produce a single combined resonance for each NV electron spin state ($|m_s = \pm 1\rangle$). (d) Laser and multi-tone RF π-pulses are repeated throughout the camera exposure to facilitate wide-field imaging. (e) A Lorentzian-shaped reduction in NV PL is observed when a RF scan is performed through each spin-transition frequency. The resonances are Zeeman split by the external magnetic field. The outer (inner) inflection points f_1, f_4 (f_2, f_3) are denoted by black squares (circles). For the resonance curves shown, the FWHM linewidth $\delta\nu = 300$ kHz and fractional optical contrast $C = 0.03$, with optical pulse = 500 ns, RF pulse = 3500 ns, photon collection rate = 1.1×10^7Hz from a 1 µm^2 pixel (0.15 µm^3 voxel), and integration time per data point = 144 ms.

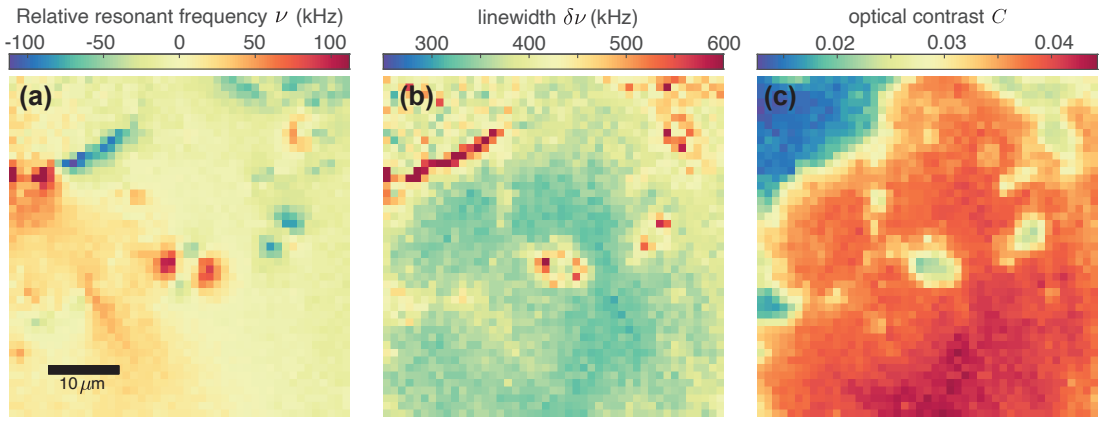

Figure 5.2: Multiple mechanisms lead to changes in NV ODMR on a micron scale when imaging static magnetic dipole and strain fields. (a) Resonance frequency ν shifts due to magnetic field and crystal strain. (b) The FWHM linewidth $\delta\nu$ varies due to gradients of magnetic and strain fields that inhomogenously broaden the NV ODMR in each pixel. (c) Optical contrast C also varies due to due to inhomogenous broadening of the NV ODMR.

dynamic range can be increased at the expense of magnetic sensitivity by RF broadening the resonance curve.

Then, dynamic magnetic imaging using the DDQ technique is demonstrated using a tethered-particle-motion (TPM) assay [40]. 500 nm streptavidin coated ferromagnetic nanoparticles (micromod Partikeltechnologie 05-19-502) were tethered by 940 bp single DNA molecules to the diamond surface. The diamond-DNA-particle tethering protocol follows Ref. [39]. Fluid flowed through the sample chamber alters the orientation of the nanoparticle magnetic moment, and the changing magnetic field is imaged at video frame-rates.

Static magnetic imaging

To measure static fields, the full NV resonance curve can be measured in wide-field with arbitrarily long acquisition times. Taking a series of PL images over a range of applied MW frequencies allows fitting of the entire resonance response in the measured range. Mapping the fitted resonance frequency at each pixel results in a partial reconstruction of the magnetic

field as seen in Fig. 5.2(a). Taking the difference between the $|m_s = 0\rangle \leftrightarrow |m_s = \pm 1\rangle$ resonance frequency maps eliminates shifts of the resonance due to non-magnetic fields and enables imaging of the absolute magnetic field projection along the NV symmetry axis [60], as seen in Fig. 5.3(a).

For quickly-varying magnetic fields, imaging via the static magnetic imaging procedure may not capture the dynamics of the magnetic field. We thus require a dynamic imaging modality that reproduces the absolute magnetic field across the imaging field of view without prior per-pixel calibration and is compatible with high-frame-rate imaging.

Dynamic magnetic imaging

Single quantum difference imaging

The simplest dynamic imaging modality uses RF excitation applied at one inflection point of one of the NV resonance curves [Fig. 5.1(e)]. PL images taken with MW π-pulses applied are subtracted from PL images taken without MW to detect changes in emitted NV PL [59]. We define a SQ difference image (DI) as

$$\mathrm{SQ}(f_1) = \frac{I_{\mathrm{off}} - I_{\mathrm{on}}(f_1)}{I_{\mathrm{off}}}, \tag{5.1}$$

in which $I_{\mathrm{on}}(f_1)$ is the intensity image taken with applied MW π-pulses at f_1 and I_{off} is the image taken with no applied MW. We assume the NV ensemble is operating in the linear-response regime of the resonance curve, i.e. $\gamma_{\mathrm{NV}} \hat{z}_{\mathrm{NV}} \cdot \vec{B} < \delta\nu$. The per-pixel signal is then given by

$$\mathrm{SQ}^{\mathrm{pp}}(f_1) = \frac{9}{8}C - \frac{3\sqrt{3}}{4}\frac{C}{\delta\nu}(\nu(\vec{E}, \vec{B}, T, ...) - f_1). \tag{5.2}$$

As discussed above, the resonance frequency ν depends on the magnetic field $\vec{B}$ and also varies with local electric field $\vec{E}$, temperature T, and crystal strain.

Additionally, variations in curve-shape, and thus C [Fig. 5.2(b)] and $\delta\nu$ [Fig. 5.2(c)], cause variations of the resonance curve inflection point, contributing to the SQ signal. Microscopic and mesoscopic strain inhomogeneities result in inhomogeneous broadening of the resonance curve [61]. Also, dephasing due to dipolar interactions between sensing NV centers and other paramagnetic impurities (e.g. P1 and ^{13}C) fundamentally limit the NV ensemble coherence, and thus, ODMR linewidth [24, 25].

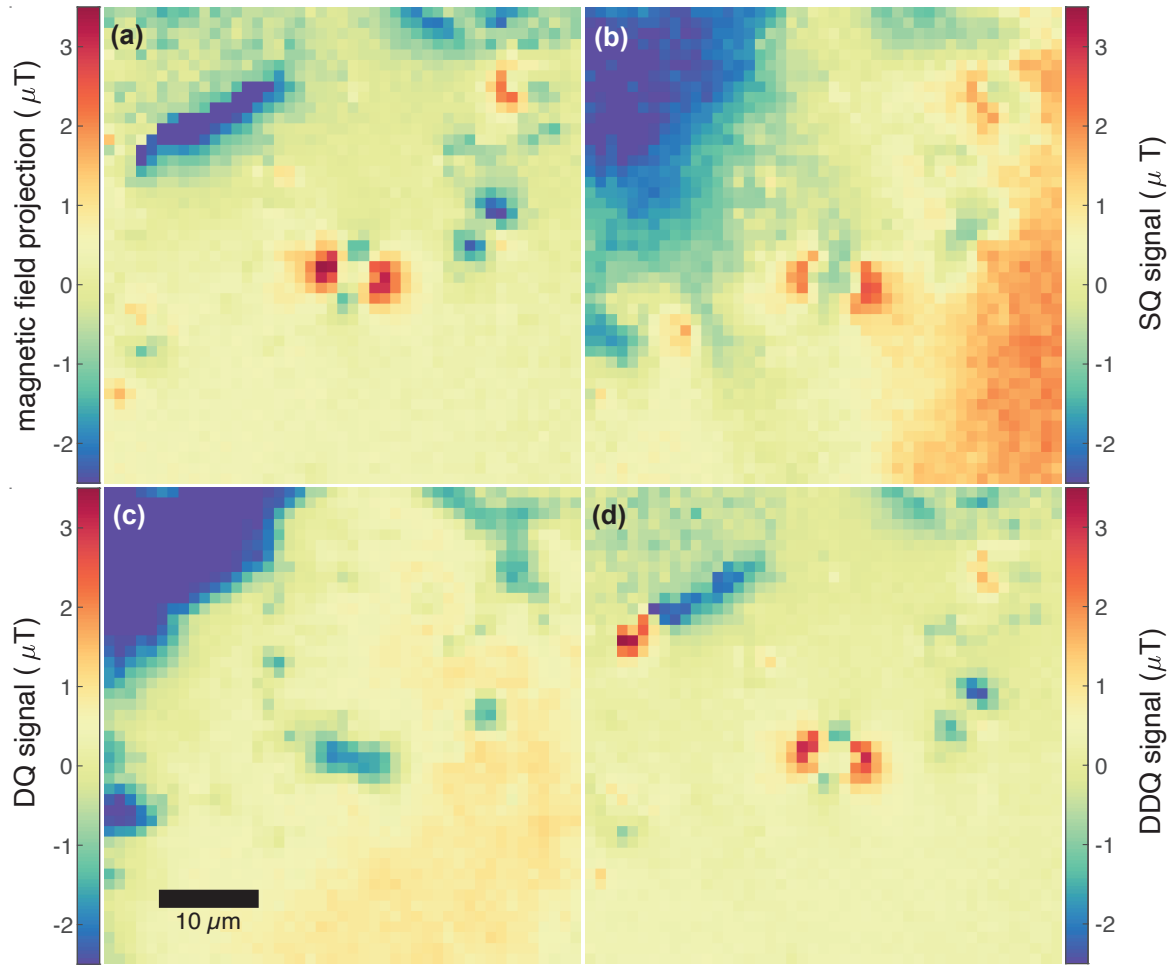

Figure 5.3: **Competing magnetic imaging modalities.**(a) 'True' static magnetic field projection map generated with the frequency scanning technique outlined in the above Static Magnetic Imaging Modality section (acquisition time 12 s). (b) Single quantum difference imaging (2.4 s). The signal measured with the SQ DI modality is a convolution of the magnetic and strain fields, which are impossible to separate with a single measurement. (c) Double quantum difference imaging (2.4 s). While the DQ DI modality has reduced the impact from the fields that homogeneously shift the NV centers, the DQ signal is more sensitive to the local contrast and linewidth variations of the NV sensing curves. (d) Double-double quantum difference imaging (2.4 s). An inspection of the competing dynamic imaging schemes (b-d) reveals that both the SQ (b) and DQ (c) schemes are significantly compromised by spurious contrast caused by strain gradients and curve-shape variation, respectively, while the DDQ scheme (d) faithfully approximates the 'true' magnetic field projection (a) with a decreased acquisition time.

The SQ DI enables imaging of some nano-scale magnetic structure, but the sensitivity of this technique is limited. In Fig. 5.3(b) we show a SQ DI image with its corresponding static magnetic field map in 5.3(a). The SQ DI enables partial mapping of the magnetic field projection, but is limited by contributions to the resonance frequency shift by strain gradients, as seen in the SQ-signal-color-gradient from upper-left to lower-right in Fig. 5.3(b).

Double quantum difference imaging

Temperature, electric field, and strain shift the zero-field-splitting of the NV ground state, causing common-mode shifts of the $|m_s = 0\rangle \leftrightarrow |m_s = \pm 1\rangle$ transitions [11]. Conversely, the magnetic-field-induced Zeeman effect splits the two transitions. Thus, by probing the difference of the two transition resonance frequencies, the common-mode shifts can be subtracted out and the magnetic field projection can be measured directly. We use a DQ driving scheme [13, 47], applying two-tone RF π-pulses at the opposite inflection points of the two resonance curves simultaneously [Fig. 5.1(e)]. We construct a DQ DI by subtracting the PL image taken with DQ RF driving from an image taken with no RF applied

$$\mathrm{DQ}(f_1, f_4) = \frac{I_{\mathrm{off}} - I_{\mathrm{on}}(f_1, f_4)}{I_{\mathrm{off}}}, \tag{5.3}$$

in which $I_{\mathrm{on}}(f_1, f_4)$ is the image taken with applied MW π-pulses at f_1 and f_4 simultaneously, and I_{off} is the image taken with no applied MW. We again assume linear-response of the resonance curves and additionally assume that the two resonance curves have the same shape. The per-pixel DQ signal is

$$\mathrm{DQ}^{\mathrm{pp}}(f_1, f_4) \approx \frac{9}{4}C - \frac{3\sqrt{3}}{4}\frac{C}{\delta\nu}(f_1 - f_4) - \frac{3\sqrt{3}}{4}\frac{C}{\delta\nu}(2\gamma_{\mathrm{NV}}\hat{z}_{\mathrm{NV}} \cdot \vec{B}). \tag{5.4}$$

By defining $\langle\vec{B}\rangle$ as the average magnetic field over the imaging field of view, Eq. 5.4 simplifies to

$$\mathrm{DQ}^{\mathrm{pp}}(f_1, f_4) = \frac{9}{4}C + \frac{3\sqrt{3}}{4}\frac{C}{\delta\nu}2\delta_0 - \frac{3\sqrt{3}}{4}\frac{C}{\delta\nu}\left(2\gamma_{\mathrm{NV}}\hat{z}_{\mathrm{NV}} \cdot \left(\vec{B} - \langle\vec{B}\rangle\right)\right), \tag{5.5}$$

where $2\delta_0 = (f_4 - f_1) - 2\gamma_{\mathrm{NV}}\hat{z}_{\mathrm{NV}} \cdot \langle\vec{B}\rangle$. By applying f_1 and f_4 at the outer inflection points of the NV resonance curves simultaneously [Fig. 5.1(e)], intensity changes induced by non-magnetic, common-mode shifts are cancelled out, while splittings caused by magnetic

signal result in a sum of changes in PL intensity. Hence, for constant C and $\delta\nu$, the DQ DI technique enables absolute magnetic imaging. [13]

Although the contribution of strain-induced-resonance-shifts to the imaging have been eliminated, overcoming the sensitivity limits of the SQ DI, we demonstrate that DQ DI has *increased* the effect of variations in curve-shape on the magnetic imaging. More specifically, variations of C and $\delta\nu$ still cause perturbations of the first two terms in Eq. 5.5. This effect can be seen by comparing the map of C in Fig. 5.2(c) to the DQ DI in Fig. 5.3(c). Thus, for practical applications of the DQ method to wide-field imaging, we find that curve-shape variations dominate and the DQ DI (Fig. 5.3(c)) is ineffective at reproducing a map of the magnetic field projection (Fig. 5.3(a)).

Double-double quantum difference imaging

To suppress the imaging dependence on curve-shape, we apply bias RFs on either side of the resonance curves [18]. We construct a DDQ DI

$$\mathrm{DDQ} = 2\frac{I_{\mathrm{on}}(f_1, f_4) - I_{\mathrm{on}}(f_2, f_3)}{I_{\mathrm{on}}(f_1, f_4) + I_{\mathrm{on}}(f_2, f_3)} \tag{5.6}$$

where $I_{\mathrm{on}}(f_1, f_4)$ ($I_{\mathrm{on}}(f_2, f_3)$) is the image taken with MW applied at the outer (inner) inflection points of the two resonance curves simultaneously, as shown in Fig. 5.1(e). By applying DQ bias MWs on either side of the resonance curves, the effects of variations in the shape of the the ODMR curve and external non-magnetic fields are mitigated. Here, the DDQ DI signal is normalized by dividing by the mean of the individual DQ frames $I_{\mathrm{on}}(f_i, f_j)$.

Because of the choice of MW frequencies, the per-pixel DDQ signal simplifies in a similar manner as the DQ signal in Eq. 5.5 giving

$$\mathrm{DDQ}^{\mathrm{pp}} \approx \frac{3\sqrt{3}}{2}\frac{C}{\delta\nu}\left(2\gamma_{\mathrm{NV}}\hat{z}_{\mathrm{NV}} \cdot \left(\vec{B} - \langle\vec{B}\rangle\right)\right). \tag{5.7}$$

DDQ eliminates the first two terms of the DQ DI signal Eq. 5.5 to obtain a single term which is linearly proportional to $(\vec{B} - \langle\vec{B}\rangle)$. There is still multiplicative dependence on C and $\delta\nu$, but because the shift of the resonance frequency far (>1 µm) from magnetic field sources falls off faster than the impact of spatial variations of curve-shape due to inhomogeneous

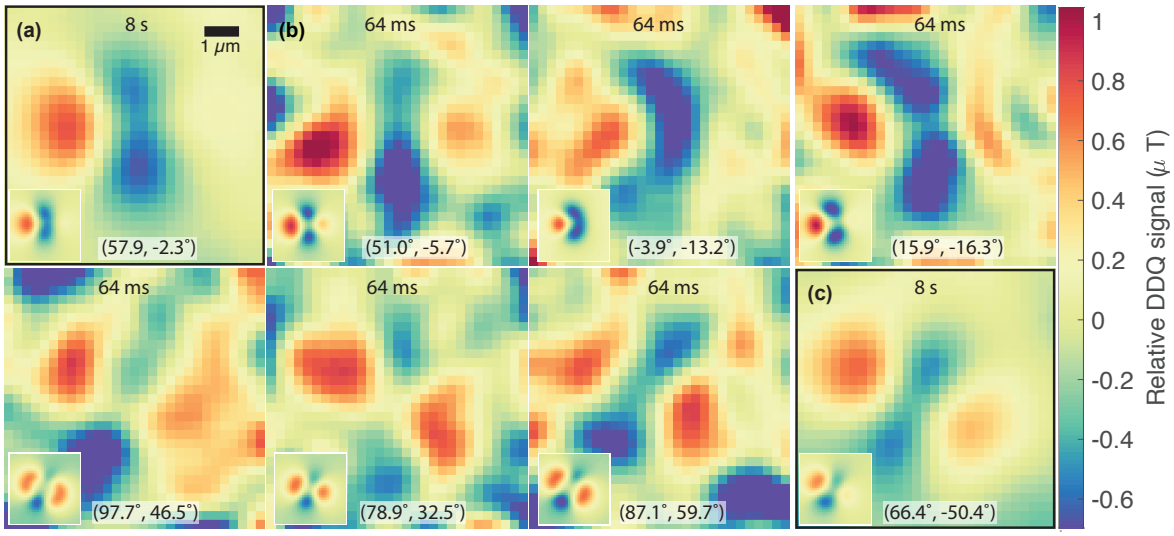

Figure 5.4: DDQ imaging of the reorientation of a DNA-tethered magnetic nanoparticle under applied flow. In each panel, the observed DDQ image is compared with a fitted DDQ image (inset) to estimate the magnetic nanoparticle dipole orientation (θ, ϕ), where the NV ensemble symmetry axis is (54.735°, 0°). For all DDQ DI in this figure, a Gaussian smoothing filter with $\sigma = 533\,\text{nm}$ is applied. (a) A time-averaged DDQ DI (8 s) showing initial magnetic nanoparticle orientation before flow. (b) Representative DDQ frames (64 ms of exposure) showing nanoparticle reorientation in response to an applied flow. (c) A time-averaged DDQ DI (8 s) showing the final magnetic nanoparticle orientation with applied flow.

broadening, there is no DDQ signal generated in regions with no magnetic field. The DDQ DI completely eliminates the large-scale, non-magnetic gradients in the SQ DI [Fig. 5.3(b)] and suppresses the C and $\delta\nu$ dependence [Fig. 5.2(b-c)] of the DQ DI [Fig. 5.3(c)]. As shown in Fig. 5.3(d), DDQ DI provides similar magnetic sensitivity as the static magnetic projection map in Fig. 5.3(a), with a greater than four-fold acquisition-time-reduction. The static imaging modality requires enough images to fit both resonance curves; the DDQ modality instead extracts the magnetic field dependence of the resonances with only two images: $I_{\mathrm{on}}(f_1, f_4)$ and $I_{\mathrm{on}}(f_2, f_3)$. While the integration time of the DDQ image shown in Fig. 5.3(d) was chosen to match the signal-to-noise ratio of the magnetic field map in Fig. 5.3(a), DDQ enables even faster magnetic imaging in general.

The general conditions for applicability for the DDQ method are as follows: (i) the resonance curve shapes of the two NV spin transitions used must be matched by driving each transition with equal Rabi frequency, (ii) non-magnetic inhomogeneities across the imaging field of view must be smaller than the resonance FWHM linewidth in order to be suppressed, and (iii) sensor operation is in the linear regime, i.e. magnetic signals to be imaged are smaller than the resonance FWHM linewidth. We discuss errors associated with condition (i) below, and note criteria (ii) and (iii) are prerequisites for any intensity-based wide-field magnetic imaging involving NV ensembles.

Wide-field dynamic magnetic imaging of ferromagnetic particle reorientation

To demonstrate that DDQ difference imaging can facilitate high-frame-rate imaging of dynamic fields, we image the changing magnetic field produced by a ferromagnetic particle tethered to the diamond sensor surface by a single DNA molecule. The approximate diamond-particle distance is 400 nm. Fig. 5.4a shows an 8 s time-averaged image of the field produced by the magnetic particle. A preferred direction is observed due to the partial alignment of the ferromagnetic particle moment orientation to the 0.35 mT external magnetic-field, oriented along $(\theta, \phi) = (54.735°, 0°)$. Next, phosphate-buffered-saline is pulled from a reservoir through the sample channel by a syringe pump at 4 ml/min. The fluid flow exerts a hydrodynamic force and torque on the tethered-particle, causing it to reorient, changing the magnetic field at the diamond sensor surface. Fig. 5.4b displays char-

acteristic frames, in chronological order, showing time-resolved imaging of the nanoparticle moment reorientation at a 15.6 Hz frame-rate (64 ms per frame), with insets showing fitted DDQ images and associated moment directions displaying the changing magnetic-moment direction in each frame. The fluid-flow-steady-state particle orientation is imaged with an 8 s time-averaged DDQ image in Fig. 5.4c. This experiment represents the novel application of micron-scale dynamic magnetometry to a single-molecule biological system.

Summary

Although the NV community has made significant progress toward eliminating inhomogeneities in NV ensemble-based-sensors through advanced diamond and NV defect fabrication [8], quantum control methods can significantly increase the sensitivity of these systems for magnetometry applications [25]. However, existing wide-field schemes fail to reliably image magnetic fields due to micron-scale variation in the resonance-curve shape. Here, we introduce a novel quantum control technique, double-double quantum difference imaging, that is suitable for mitigating inhomogeneities in wide-field dc magnetometry to enable imaging of time-varying fields. Using four-tone RF pulses and only a two-image sequence, we show both theoretically and experimentally that DDQ difference imaging not only mitigates non-magnetic perturbations of the NV resonance frequency but also variations of resonance curve-shape. Static-field imaging reveals that these resonance shape variations can be the dominant source of imaging noise in a state-of-the-art NV magnetic imaging surface. Finally, we use the DDQ technique to perform wide-field magnetic microscopy of a dynamic, biological system, enabling high frame-rate orientation imaging of a magnetic nanoparticle tethered to the diamond sensor by a single DNA molecule. DDQ difference imaging eliminates the need for per-pixel calibration and enables high-frame-rate magnetic microscopy via NV photoluminescence intensity imaging.

Chapter 6

MEASURE OF DNA BEND STIFFNESS USING QUANTUM MAGNETOMETRY OF A NANO-MECHANICAL TORQUE BALANCE

6.1 Abstract

DNA mechanical flexibility is a key parameter relevant to nucleosome compaction and transcription regulation, however, the bend stiffness of DNA at nucleosome-size length scales has not yet been directly probed. In this work, a nano-mechanical torque balance is formed by constraining individual DNA molecules between a ferromagnetic nanoparticle probe and a diamond quantum magnetic field imager. Using a magnetic tweezer field, a torque is applied to the ferromagnetic probe and the direction of the applied field and magnetic particle moment are read out using quantum magnetic imaging of diamond defect qubits.

6.2 Short DNA bending background

Despite the long history of research into DNA's bio-mechanical properties [62], the energy requirements of bending short, 75-300 base pair (bp) DNA molecules has not been fully understood. DNA flexibility is relevant for transcription regulation [40, 63] and chromosomal packaging [42, 64]. Short DNA molecules are wrapped around histones to form nucleosomes, the basic packaging units used in DNA storage [65]. Long (compared to histone scales) DNA length measurements point to a polymer bend energy model that is quadratic in bend angle called the worm-like-chain (WLC) model [42]. However, cyclization measurements at short length scales demonstrate that bends are significantly more probable than the WLC model predicts [37, 64]. The lack of studies of the bend response of short DNA molecules is in part due the difficulty of measuring torque exerted by individual DNA molecules and the challenge of probing the bend response at the short length scales.

The bending of a polymer is quantified by its persistence length L_p, $L_p = \kappa/k_BT$ and κ is the bend stiffness. For DNA, this number is measured to be 150 lp in experiments on

DNA molecules longer than L_p [42]. Persistence length can be understood as the length scale at which a polymer can be treated as an un-bendable rod. Quantitatively, L_p is defined as either the length scale at which the time-averaged angle between the two ends of a DNA fragment is equal to 1 radian or the distance over which two segments of the DNA molecule are directionally correlated.

6.3 Nano-mechanical torque balance experiment

In this work, a nano-mechanical torque balance is used to measure the bend response of individual DNA fragments, see Figure 6.1. A DNA molecule is attached at multiple sites to a diamond quantum magnetic field sensor. A ferromagnetic nanoparticle is attached at the other end of the DNA molecule. The orientation of the magnetic probe and applied field are measured using quantum magnetic imaging of an NV ensemble in the diamond sensor. The DNA molecules are bent through multiple angles using a magnetic tweezer field. The probe moment direction $\vec{m}$ and the applied magnetic field $\vec{B}_{MT}$ are imaged simultaneously, and the torque exerted by the DNA as a function of bend angle is measured by imaging deflections between the applied field and the nanoparticle moment vectors.

The torque exerted by the magnetic field on the magnetic particle is given by

$$\vec{\tau}_B = \vec{m} \times \vec{B}, \tag{6.1}$$

and the torque exerted by the DNA on the magnetic particle in the WLC model is

$$\vec{\tau}_{DNA} = \frac{\kappa}{L}\vec{\phi}_{DNA} = k_B T \frac{L_p}{L}\phi_{DNA}\hat{\phi}_{DNA}, \tag{6.2}$$

where ϕ_{DNA} is the bend angle of the DNA molecule. In the torque balance experiment, $\vec{\tau}_B = \vec{\tau}_{DNA}$. In the case of out-of-plane torques, the in-plane magnetic moment direction ϕ_m is modelled by

$$\phi_m - \phi_0 = \frac{(\vec{m} \times \vec{B}) \cdot \hat{z}}{\kappa/L \ \mathrm{dir}(\vec{B} \times \vec{m}) \cdot \hat{z}} \tag{6.3}$$

where the bend angle of the DNA molecule is assumed to be equal to the magnetic particle direction minus a constant offset given by the stochastic binding of the magnetic particle to the DNA molecule, so $\phi_{DNA} = \phi_m - \phi_0$.

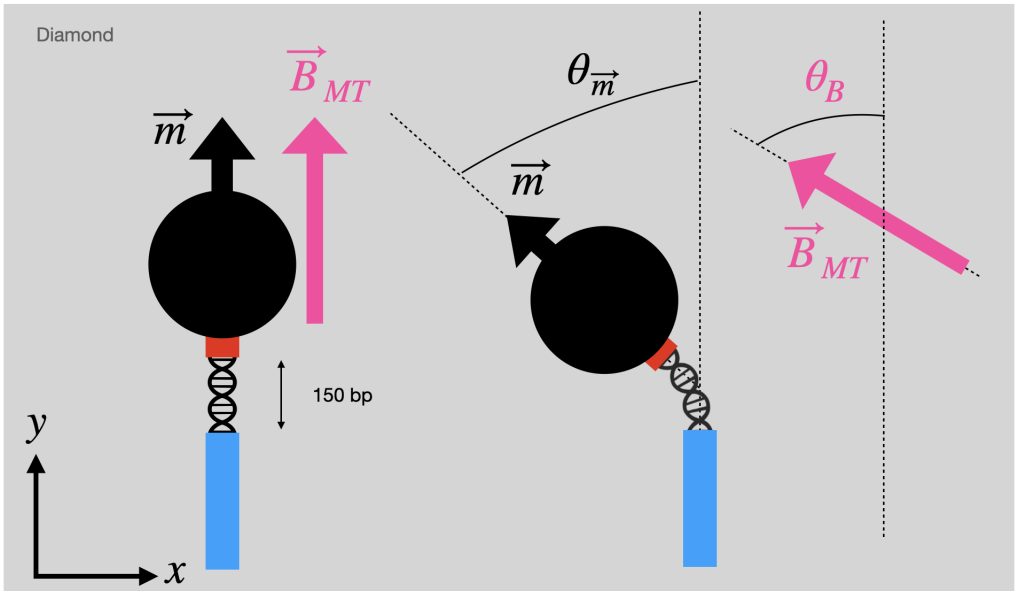

Figure 6.1: **Nano-mechanical DNA torque balance schematic.** A short (150 bp) DNA molecule is sandwiched between a ferromagnetic particle at one end and diamond magnetic field imager at the other. An applied field $\vec{B}_{MT}$ is used to exert a torque on the ferromagnetic particle. The ferromagnetic particle dipole moment $\vec{m}$ and applied magnetic field $\vec{B}_{MT}$ vectors are imaged using NV defects in the diamond. Torque exerted by DNA on the particle causes angular displacements between the vectors $\vec{m}$ and $\vec{B}_{MT}$.

6.3.1 Dipole vector magnetic field imaging

To image the applied magnetic field and the ferromagnetic probe moment, wide-field vector magnetometry is performed as discussed in Section 4.5. Fluorescence images are collected as the applied MW is swept over a range of frequencies, and PODMR of the NV ensemble is recorded. The mean fluorescence count at each MW is fit to a multi-dip Lorentzian. The four Zeeman splittings associated with each NV orientation are then linearly transformed to magnetic field components in the lab frame. Because the magnetic particle dipole field averages to zero over a field of view, the mean ODMR spectrum over an imaging field-of-view measures the applied magnetic field. This mean spectrum fit is used as a guess for each individual pixel's ODMR spectrum. The variations across the imaging field of view are given by the ferromagnetic probe dipole field. In this way, vector magnetometry of the applied magnetic field and probe field vectors is performed simultaneously.

The magnetic particle field components as a function of applied field angle are then fit using least-squares to a six-parameter dipole model as described in Section **??**. An example of the results of this fitting is show in Figure 6.2.

An individual single domain cobalt ferromagnetic particle is tethered by a 600 bp DNA molecule in the torque balance configuration. Vector images of the particle magnetic field are fit to a point dipole model with six-parameters, the dipole magnetic moment and position vectors. The three columns show B_x, B_x, and B_z. The first row shows the measured vector images using the PODMR vector magnetometry method. The second row shows the measured images with a gradient mask. The gradient mask is necessary to match the magnetic dipole fit with the experimental data because of the limit of magnetic field gradient observable in the NV platform as mentioned in Section **??**. The mask is constructed by examining inhomogenous broadening of the NV ODMR and masking pixels with inhomogenous broadening above a cutoff threshold. The third row shows the fitted images using the six-parameter dipole model with the empirically-determined gradient mask. The fourth row shows the dipole model fit without mask. The dipole model predicts high field strengths which produce large magnetic field gradients that are unobservable by the magPI platform, thus the gradient mask is necessary. The fifth row shows the residual between

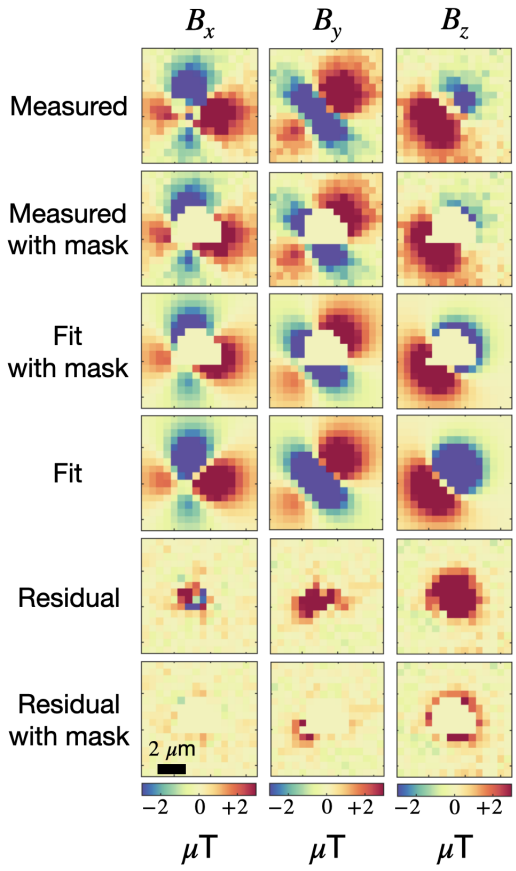

Figure 6.2: **Magnetic particle moment direction determined by quantum vector magnetometry.** An individual single domain cobalt ferromagnetic particle is tethered by a 600 bp DNA molecule in the torque balance configuration. Vector images of the particle magnetic field are fit to a point dipole model with six-parameters, the dipole magnetic moment and position vectors. The three columns show B_x, B_x, and B_z. The first row shows measured vector images, second row shows the measured images with a gradient mask, third row shows the fitted images using the six-parameter dipole model with gradient mask, fourth row shows the fit without mask, fifth is the residual between the measured data and the fit with mask, and sixth shows the residual between the measured data with mask and the fit with mask. The magnetic moment vector of the particle is fit and the magnitude of the moment 5×10^{-18} Am^2 is consistent with a prediction for an individual 50 nm cobalt single domain ferromagnetic particle.

the measured data and the fit with mask, and large residuals appear between the fit and measured data due to the large field gradients that are not resolved in the experimental data. The sixth row shows the residual between the measured data with mask and the fit with mask. This residual is the most important to minimize as it compares the dipole model and experimental data on equal footing. The magnetic moment vector of the particle is fit and the magnitude of the moment $\approx 5 \times 10^{-18}$ Am^2 is consistent with a prediction for an individual 50 nm cobalt single domain ferromagnetic particle. In this way, fitting magnetic dipole images measures the magnetic moment vector magnitude and direction.

6.3.2 Dipole orientation illuminates qualitative differences in DNA binding character

To demonstrate the ability of the nano-mechanical torque balance to probe DNA bending, magnetic particles were used in three distinct bio-mechanical constructs. In the first case, the magnetic particle was tethered by a "free" DNA tether in which the particle-DNA and DNA-surface binding is accomplished by a single binding site. The free DNA tethered magnetic particle is free to align to the applied field. In the second configuration, the magnetic nanoparticle was stuck to the diamond sensor surface. In this case, the particle magnetic moment is fixed by the surface interaction, no matter the direction of the applied field. In the final case, a single domain ferromagnetic particles were tethered by 600 bp DNA molecules with multiple binding sites at the particle-DNA and DNA-surface interfaces. In the torque balance case, both the applied field and DNA are able to exert a torque on the magnetic nanoparticle. The measured distinctions between these cases are shown in images with overlaid measured moment and applied field vectors in Figure 6.3 and only with measured moment and applied field vectors in Figure 6.4.

These three distinct bio-mechanical configurations result in qualitatively different magnetic dipole orientations. Two configurations are control experiments for the nano-torque balance, the free DNA tether and the stuck particle. In Figure 6.3(a), the dipole moment projection along the magnetic moment vector is shown for a free DNA tether. The dipole moment points along the applied field direction. The discrepancy between the applied field and magnetic moment in Figure 6.4(a) is given by uncertainty in the fitted magnetic mo-

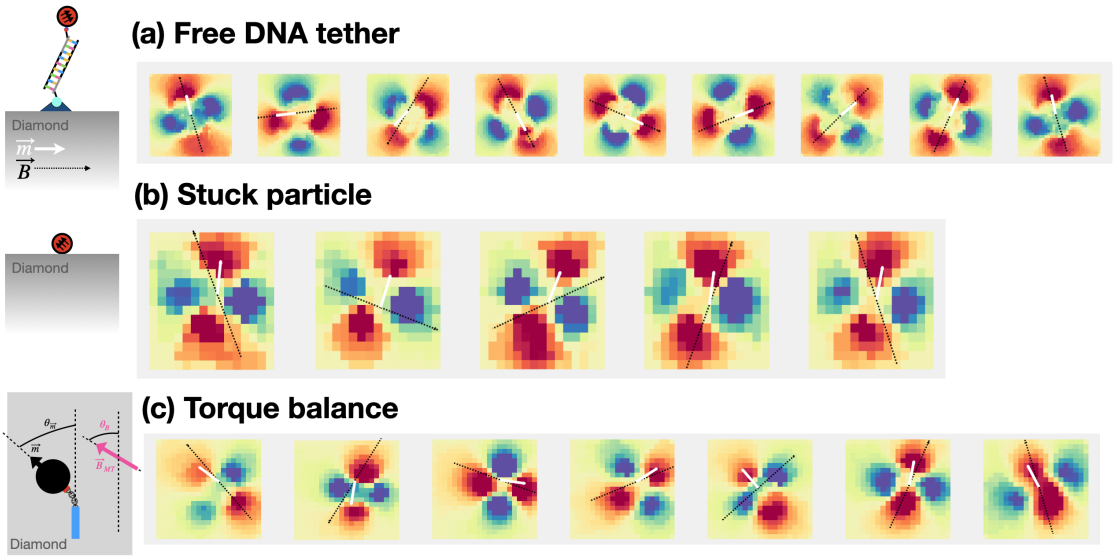

Figure 6.3: **Dipole orientation illuminates qualitative differences in DNA binding character, image comparison.** Ferromagnetic dipole images with changing applied field angle are shown for three different biomechanical configurations in the three rows, and different applied field direction in the different columns. In each series, the dipole image is shown, overlaid with the fitted moment direction vector in white and the applied field direction vector in dashed black. (a) Particle tethered by an free DNA tether. The dipole moment is free to re-orient and points along the applied field direction. (b) Particle stuck to the diamond sensor surface. The dipole moment direction is independent of applied field angle and points in a constant direction. (c) Particle in a nano-mechanical torque balance. The dipole moment direction is balanced by a torque from the applied field and a torque from the DNA. The particle aligns with the field for certain angles of the magnetic field and deviates from the applied field from other angles due to the torque applied by the DNA.

ment direction. In Figure 6.4(b) the particle stuck to the diamond sensor surface is seen to maintain its orientation no matter the direction of the applied field. In general, varying stuck magnetic particles are oriented randomly and maintain their orientation in changing applied fields.

After the two control experiments, a particle in a nano-mechanical torque balance is examined. The dipole moment direction is balanced by a torque from the applied field and a torque from the DNA. In Figure 6.4(a), the particle is seen to align with the field for certain angles of the magnetic field and deviates from the applied field from other angles due to the torque applied by the DNA. Depending on the bend angle, the DNA exerts a torque Measured magnetic moment and applied field vectors are plotted for three distinct biomechanical configurations. Colors indicate differing directions of the applied field vector, and the associated magnetic moment response vector is colored the same. (a) Particle tethered by an free DNA tether. The free DNA-tethered particle is free to align with the applied field and the magnetic moment vector tracks with the applied field vector. (b) Particle stuck to the diamond sensor surface. The dipole moment direction is independent of applied field angle and points in a constant direction. (c) Particle in a nano-mechanical torque balance. The dipole moment nutates about a "home" orientation. The amount of nutation is related to the strength of the applied field and the bending stiffness.

6.3.3 Bend stiffness measurement

To measure bend stiffness, the applied field is reoriented and the magnetic particle moment vector is imaged. Fine angle steps allow for high resolution comparison of the measured magnetic moment directions to the WLC prediction given by equation 6.3. Figure 6.5(b) shows the torque balance response for 600 bp DNA molecules. Three different particles with three different moment magnitudes m_i are shown, and the model in equation 6.3 is overlayed. These three experiments show consistency with the WLC model with persistence length 150 bp.

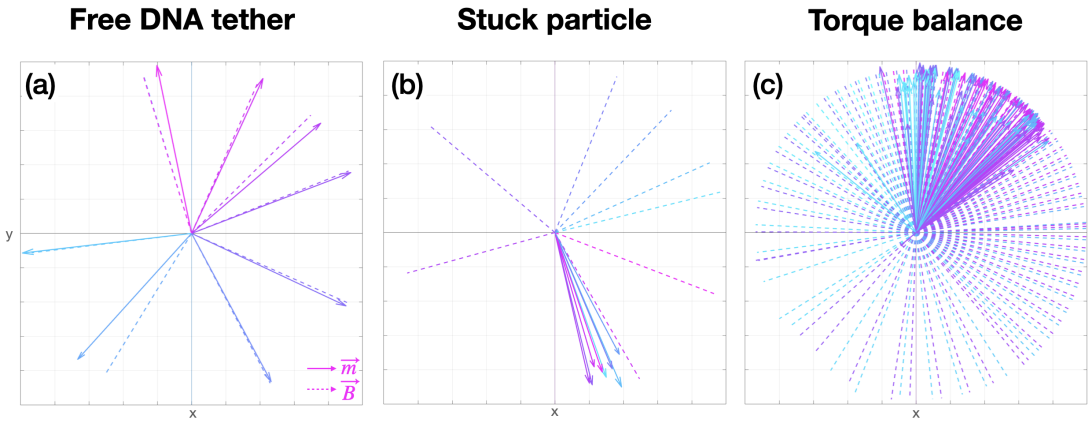

Figure 6.4: **Dipole orientation illuminates qualitative differences in DNA binding character, vector comparison.** Measured magnetic moment and applied field vectors are plotted for three distinct biomechanical configurations. Colors indicate differing directions of the applied field vector, and the associated magnetic moment response vector is colored the same. (a) Particle tethered by an free DNA tether. The free DNA-tethered particle is free to align with the applied field and the magnetic moment vector tracks with the applied field vector. (b) Particle stuck to the diamond sensor surface. The dipole moment direction is independent of applied field angle and points in a constant direction. (c) Particle in a nano-mechanical torque balance. The dipole moment nutates about a "home" orientation. The amount of nutation is related to the strength of the applied field and the bending stiffness.

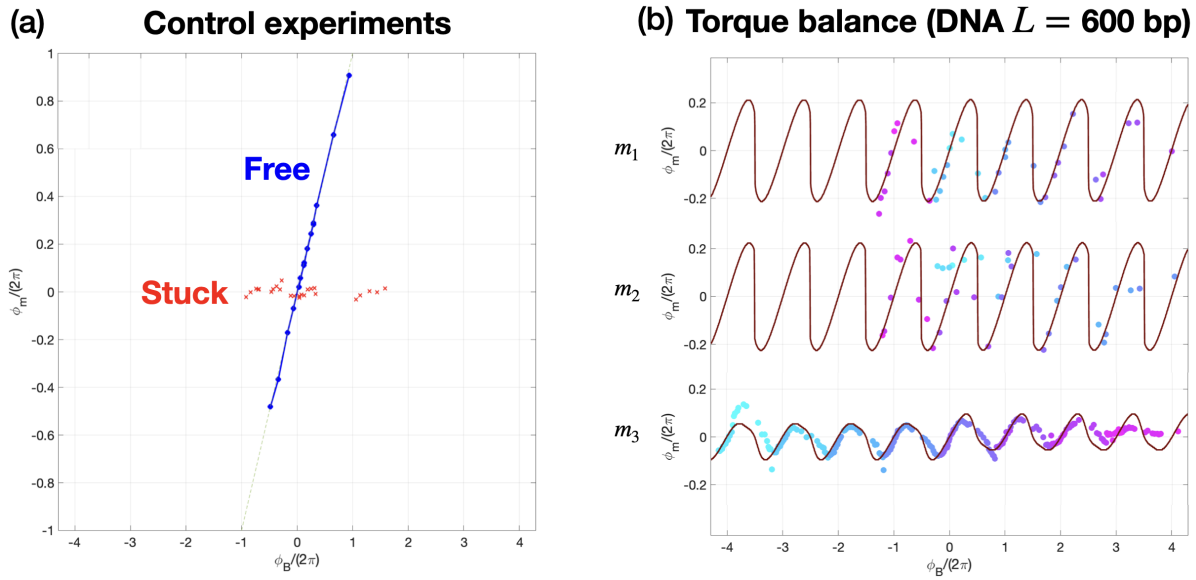

Figure 6.5: **Response of dipole to applied field measures bend stiffness.** (a) Control experiments: stuck and free particles. The measured magnetic moment in plane angle ϕ_m is plotted as a function of applied field angle ϕ_B . In the stuck case, the dipole direction is constant and independent of applied field direction. In the free case, the dipole direction tracks with applied field. (b) Torque balance response for 600 bp DNA molecules. Three different particles with three different moment magnitudes m_i are shown. The data is consistent with a WLC sinusoidal model with L_p=150 bp.

6.4 Summary

In this chapter, a nano-mechanical torque balance is constructed to measure the bend stiffness of individual DNA molecules. The wide-field quantum magnetic particle imaging platform is used to measure the vector magnetic field produced by ferromagnetic nanoparticles in three distinct configurations: free DNA tether, stuck magnetic particle and nano-torque balance. The dipole magnetic field images are fit to measure the dipole moment vector, and the three configurations are distinguished in examining the dipole magnetic moment vector response to the applied field. In the torque balance case, the magnetic moment vector is imaged under a range of applied field directions, and the in-plane magnetic moment angle response is consistent with the WLC model with the nominal value of persistence length. This work demonstrates the viability of the nano-torque balance to measure DNA bend stiffness and opens the door for single-molecule bend stiffness measurements of sub-nucleosome-scale DNA molecules as well as sequence-dependent bending stiffness of individual DNA molecules.

Chapter 7
SUMMARY AND OUTLOOK

In this thesis, a new imaging platform is developed to study bio-mechanical orientation based on a near-surface ensemble of diamond nitrogen-vacancy (NV) quantum defects. Magnetic nanoparticles are attached to individual DNA molecules, and the diamond quantum imaging platform is used to image the magnetic nanoparticle orientation to infer underlying biophysics. The operating principles of NV magnetometry and sensitivity limits are discussed. Then, the DNA tethered-particle-motion (TPM) assay is introduced, and the novel magnetic particle TPM assay is motivated. The details of the magnetic particle imaging (magPI) platform are outlined. Two imaging modalities are discussed: dynamic magnetic orientation tracking using a novel double-double quantum (DDQ) imaging technique and static magnetic orientation imaging that illuminates DNA bend stiffness. This collection of work comprises the application of quantum sensing to enable single-molecule biophysics measurements that have not been prior possible.

This work can be extended in both the dynamic and static imaging modalities using Fourier optical processing [66]. Using this technique, the ODMR signal from the four distinct NV crystallographic orientations can be measured separately. Using Fourier imaging, the DDQ imaging technique can be extended to all four NV orientations, enabling wide-field vector magnetometry at video frame rates. This advancement would further advance the dynamic orientation tracking developed in this thesis and enable tracking in arbitrarily low ambient magnetic field environments which are currently inaccessible due to the effects of a necessary applied magnetic field that lifts the degeneracy of the four NV orientations. In the torque balance experiment, Fourier optical processing will allow for a uniform magnetic tweezer field magnitude that will simplify the DNA bending model. Additionally, the nano-torque balance technique can be extended to measure the bend stiffness of short DNA molecules, and sequence dependent DNA bending rigidity.

BIBLIOGRAPHY

[1] Srivatsa Chakravarthi, Christian Pederson, Zeeshawn Kazi, Andrew Ivanov, and Kai-Mei C Fu. Impact of surface and laser-induced noise on the spectral stability of implanted nitrogen-vacancy centers in diamond. *Phys. Rev. B Condens. Matter*, 104(8):085425, August 2021.

[2] Till Lenz, Georgios Chatzidrosos, Zhiyuan Wang, Lykourgos Bougas, Yannick Dumeige, Arne Wickenbrock, Nico Kerber, Jakub Zázvorka, Fabian Kammerbauer, Mathias Kläui, and Others. Imaging topological spin structures using light-polarization and magnetic microscopy. *Physical Review Applied*, 15(2):024040, 2021.

[3] C L Degen, F Reinhard, and P Cappellaro. Quantum sensing. *Rev. Mod. Phys.*, 89(3):035002, July 2017.

[4] Pieter Zeeman. The effect of magnetisation on the nature of light emitted by a substance. *Nature*, 55(1424):347, 1897.

[5] J R Maze, A Gali, E Togan, Y Chu, A Trifonov, E Kaxiras, and M D Lukin. Properties of nitrogen-vacancy centers in diamond: the group theoretic approach, 2011.

[6] Eisuke Abe and Kento Sasaki. Tutorial: Magnetic resonance with nitrogen-vacancy centers in diamond—microwave engineering, materials science, and magnetometry. *J. Appl. Phys.*, 123(16):161101, April 2018.

[7] M L Goldman, M W Doherty, A Sipahigil, N Y Yao, S D Bennett, N B Manson, A Kubanek, and M D Lukin. State-selective intersystem crossing in nitrogen-vacancy centers. *Phys. Rev. B Condens. Matter*, 91(16):165201, April 2015.

[8] V M Acosta, E Bauch, M P Ledbetter, C Santori, K-M C Fu, P E Barclay, R G Beausoleil, H Linget, J F Roch, F Treussart, S Chemerisov, W Gawlik, and D Budker. Diamonds with a high density of nitrogen-vacancy centers for magnetometry applications. *Phys. Rev. B Condens. Matter*, 80(11):115202, September 2009.

[9] S Felton, A M Edmonds, M E Newton, P M Martineau, D Fisher, D J Twitchen, and J M Baker. Hyperfine interaction in the ground state of the negatively charged nitrogen vacancy center in diamond. *Phys. Rev. B Condens. Matter*, 79(7):075203, February 2009.

[10] Marcus W Doherty, Neil B Manson, Paul Delaney, Fedor Jelezko, Jörg Wrachtrup, and Lloyd C L Hollenberg. The nitrogen-vacancy colour centre in diamond. *Phys. Rep.*, 528(1):1–45, July 2013.

[11] Edlyn V Levine, Matthew J Turner, Pauli Kehayias, Connor A Hart, Nicholas Langellier, Raisa Trubko, David R Glenn, Roger R Fu, and Ronald L Walsworth. Principles and techniques of the quantum diamond microscope. *Nanophotonics*, 8(11):1945–1973, November 2019.

[12] A T Collins, M F Thomaz, and M I B Jorge. Luminescence decay time of the 1.945 ev centre in type ib diamond. *J. Phys. C: Solid State Phys.*, 16(11):2177, April 1983.

[13] Kejie Fang, Victor M Acosta, Charles Santori, Zhihong Huang, Kohei M Itoh, Hideyuki Watanabe, Shinichi Shikata, and Raymond G Beausoleil. High-sensitivity magnetometry based on quantum beats in diamond nitrogen-vacancy centers. *Phys. Rev. Lett.*, 110(13):130802, March 2013.

[14] H J Mamin, M H Sherwood, M Kim, C T Rettner, K Ohno, D D Awschalom, and D Rugar. Multipulse double-quantum magnetometry with near-surface nitrogen-vacancy centers. *Phys. Rev. Lett.*, 113(3):030803, July 2014.

[15] Michael Gould, Emma R Schmidgall, Shabnam Dadgostar, Fariba Hatami, and Kai-Mei C Fu. Efficient extraction of Zero-Phonon-Line photons from single Nitrogen-Vacancy centers in an integrated GaP-on-Diamond platform. *Phys. Rev. Appl.*, 6(1):011001, July 2016.

[16] S B van Dam, M Walsh, M J Degen, E Bersin, S L Mouradian, A Galiullin, M Ruf, M IJspeert, T H Taminiau, R Hanson, and D R Englund. Optical coherence of diamond nitrogen-vacancy centers formed by ion implantation and annealing. *Phys. Rev. B Condens. Matter*, 99(16):161203, April 2019.

[17] Dmitry Budker and Michael Romalis. Optical magnetometry. *Nat. Phys.*, 3(4):227–234, April 2007.

[18] Michael Gould, Russell Barbour, Nicole Thomas, Hamed Arami, Kannan M Krishnan, and Kai-Mei Fu. Room-temperature detection of single 20 nm super-paramagnetic nanoparticles with an imaging magnetometer. March 2014.

[19] A Dréau, M Lesik, L Rondin, P Spinicelli, O Arcizet, J-F Roch, and V Jacques. Avoiding power broadening in optically detected magnetic resonance of single NV defects for enhanced dc magnetic field sensitivity. *Phys. Rev. B Condens. Matter*, 84(19):195204, November 2011.

[20] J R Maze, P L Stanwix, J S Hodges, S Hong, J M Taylor, P Cappellaro, L Jiang, M V Gurudev Dutt, E Togan, A S Zibrov, A Yacoby, R L Walsworth, and M D Lukin. Nanoscale magnetic sensing with an individual electronic spin in diamond. *Nature*, 455(7213):644–647, October 2008.

[21] V M Acosta, E Bauch, M P Ledbetter, A Waxman, L-S Bouchard, and D Budker. Temperature dependence of the nitrogen-vacancy magnetic resonance in diamond. *Phys. Rev. Lett.*, 104(7):070801, February 2010.

[22] D P L Aude Craik, P Kehayias, A S Greenspon, X Zhang, M J Turner, J M Schloss, E Bauch, C A Hart, E L Hu, and R L Walsworth. Microwave-assisted spectroscopy technique for studying charge state in nitrogen-vacancy ensembles in diamond. *Phys. Rev. Appl.*, 14(1), July 2020.

[23] P Maletinsky, S Hong, M S Grinolds, B Hausmann, M D Lukin, R L Walsworth, M Loncar, and A Yacoby. A robust scanning diamond sensor for nanoscale imaging with single nitrogen-vacancy centres. *Nat. Nanotechnol.*, 7(5):320–324, April 2012.

[24] Ed E Kleinsasser, Matthew M Stanfield, Jannel K Q Banks, Zhouyang Zhu, Wen-Di Li, Victor M Acosta, Hideyuki Watanabe, Kohei M Itoh, and Kai-Mei C Fu. High density nitrogen-vacancy sensing surface created via he+ ion implantation of 12C diamond. *Appl. Phys. Lett.*, 108(20):202401, May 2016.

[25] Erik Bauch, Connor A Hart, Jennifer M Schloss, Matthew J Turner, John F Barry, Pauli Kehayias, Swati Singh, and Ronald L Walsworth. Ultralong dephasing times in Solid-State spin ensembles via quantum control. *Phys. Rev. X*, 8(3):031025, July 2018.

[26] Toyofumi Ishikawa, Kai-Mei C Fu, Charles Santori, Victor M Acosta, Raymond G Beausoleil, Hideyuki Watanabe, Shinichi Shikata, and Kohei M Itoh. Optical and spin coherence properties of nitrogen-vacancy centers placed in a 100 nm thick isotopically purified diamond layer. *Nano Lett.*, 12(4):2083–2087, April 2012.

[27] Gijs de Lange, Toeno van der Sar, Machiel Blok, Zhi-Hui Wang, Viatcheslav Dobrovitski, and Ronald Hanson. Controlling the quantum dynamics of a mesoscopic spin bath in diamond. *Sci. Rep.*, 2:382, April 2012.

[28] John F Barry, Matthew J Turner, Jennifer M Schloss, David R Glenn, Yuyu Song, Mikhail D Lukin, Hongkun Park, and Ronald L Walsworth. Optical magnetic detection of single-neuron action potentials using quantum defects in diamond. *Proc. Natl. Acad. Sci. U. S. A.*, 113(49):14133–14138, December 2016.

[29] R L Fagaly. Superconducting quantum interference device instruments and applications. *Rev. Sci. Instrum.*, 77(10), 2006.

[30] Matti Hämäläinen, Riitta Hari, Risto J Ilmoniemi, Jukka Knuutila, and Olli V Lounasmaa. Magnetoencephalography—theory, instrumentation, and applications to noninvasive studies of the working human brain. *Rev. Mod. Phys.*, 65(2):413–497, April 1993.

[31] Riitta Hari and Riitta Salmelin. Magnetoencephalography: From SQUIDs to neuroscience. neuroimage 20th anniversary special edition. *Neuroimage*, 61(2):386–396, June 2012.

[32] Keiji Enpuku, Tadashi Minotani, Takemitsu Gima, Yukinori Kuroki, Yuzuru Itoh, Makiko Yamashita, Yoshinori Katakura, and Satoru Kuhara. Detection of magnetic nanoparticles with superconducting quantum interference device (SQUID) magnetometer and application to immunoassays. *Jpn. J. Appl. Phys.*, 38(10A):L1102, October 1999.

[33] Ethan J Pratt, Micah Ledbetter, Ricardo Jiménez-Martínez, Benjamin Shapiro, Amelia Solon, Geoffrey Z Iwata, Steve Garber, Jeff Gormley, Dakota Decker, David Delgadillo, Argyrios T Dellis, Jake Phillips, Guhan Sundar, Jerry Leung, Jim Coyne, Mike McKinley, Gilbert Lopez, Scott Homan, Lucas Marsh, Mary Zhang, Vincent Maurice, Benjamin Siepser, Teresa Giovannoli, Brandon Leverett, Gabriel Lerner, Scott Seidman, Vicente DeLuna, Kayla Wright-Freeman, Julian Kates-Harbeck, Teague Lasser, Hooman Mohseni, T J Sharp, Anthony Zorzos, Antonio H Lara, Ali Kouhzadi, Alejandro Ojeda, Pronoy Chopra, Zachary Bednarke, Michael Henninger, and Jamu K Alford. Kernel flux: a whole-head 432-magnetometer optically-pumped magnetoencephalography (OP-MEG) system for brain activity imaging during natural human experiences. In *Optical and Quantum Sensing and Precision Metrology*, volume 11700, pages 162–179. SPIE, March 2021.

[34] M P Ledbetter, I M Savukov, V M Acosta, D Budker, and M V Romalis. Spin-exchange-relaxation-free magnetometry with cs vapor. *Phys. Rev. A*, 77(3):033408, March 2008.

[35] Cort Johnson, Natalie L Adolphi, Kimberly L Butler, Lovato Debbie M, Richard Larson, Peter D D Schwindt, and Edward R Flynn. Magnetic relaxometry with an atomic magnetometer and SQUID sensors on targeted cancer cells. *J. Magn. Magn. Mater.*, 324(17):2613–2619, August 2012.

[36] Chongli Yuan, Huimin Chen, Xiong Wen Lou, and Lynden A Archer. DNA bending stiffness on small length scales. *Phys. Rev. Lett.*, 100(1):018102, January 2008.

[37] Reza Vafabakhsh and Taekjip Ha. Extreme bendability of DNA less than 100 base pairs long revealed by single-molecule cyclization. *Science*, 337(6098):1097–1101, August 2012.

[38] Long Chen, Xingye Chen, Xusan Yang, Chao He, Miaoyan Wang, Peng Xi, and Juntao Gao. Advances of super-resolution fluorescence polarization microscopy and its applications in life sciences. *Comput. Struct. Biotechnol. J.*, 18:2209–2216, June 2020.

[39] Daniel T Kovari, Yan Yan, Laura Finzi, and David Dunlap. Tethered particle motion: An easy technique for probing DNA topology and interactions with transcription factors. *Methods Mol. Biol.*, 1665:317–340, 2018.

[40] L Finzi and J Gelles. Measurement of lactose repressor-mediated loop formation and breakdown in single DNA molecules. *Science*, 267(5196):378–380, January 1995.

[41] David Swigon, Bernard D Coleman, and Wilma K Olson. Modeling the lac repressor-operator assembly: the influence of DNA looping on lac repressor conformation. *Proc. Natl. Acad. Sci. U. S. A.*, 103(26):9879–9884, June 2006.

[42] Paul A Wiggins and Philip C Nelson. Generalized theory of semiflexible polymers. *Phys. Rev. E Stat. Nonlin. Soft Matter Phys.*, 73(3 Pt 1):031906, March 2006.

[43] Kenichi Ohno, F Joseph Heremans, Charles F de las Casas, Bryan A Myers, Benjamín J Alemán, Ania C Bleszynski Jayich, and David D Awschalom. Three-dimensional localization of spins in diamond using 12C implantation. *Appl. Phys. Lett.*, 105(5):052406, 2014.

[44] Christian Osterkamp, Martin Mangold, Johannes Lang, Priyadharshini Balasubramanian, Tokuyuki Teraji, Boris Naydenov, and Fedor Jelezko. Engineering preferentially-aligned nitrogen-vacancy centre ensembles in CVD grown diamond. *Sci. Rep.*, 9(1):5786, April 2019.

[45] Tim R Eichhorn, Claire A McLellan, and Ania C Bleszynski Jayich. Optimizing the formation of depth-confined nitrogen vacancy center spin ensembles in diamond for quantum sensing. *Phys. Rev. Mater.*, 3(11):113802, November 2019.

[46] J-P Tetienne, R W de Gille, D A Broadway, T Teraji, S E Lillie, J M McCoey, N Dontschuk, L T Hall, A Stacey, D A Simpson, and L C L Hollenberg. Spin properties of dense near-surface ensembles of nitrogen-vacancy centers in diamond. *Phys. Rev. B Condens. Matter*, 97(8):085402, February 2018.

[47] B A Myers, A Ariyaratne, and A C Bleszynski Jayich. Double-Quantum Spin-Relaxation limits to coherence of Near-Surface Nitrogen-Vacancy centers. *Phys. Rev. Lett.*, 118(19):197201, May 2017.

[48] Roman A Khmelnitsky, Valeriy A Dravin, Alexey A Tal, Evgeniy V Zavedeev, Andrey A Khomich, Alexander V Khomich, Alexander A Alekseev, and Sergey A Terentiev. Damage accumulation in diamond during ion implantation. *J. Mater. Res.*, 30(9):1583–1592, May 2015.

[49] K-Mc Fu, C Santori, P E Barclay, and R G Beausoleil. Conversion of neutral nitrogen-vacancy centers to negatively charged nitrogen-vacancy centers through selective oxidation. *Appl. Phys. Lett.*, 96(12):121907, 2010.

[50] Eduardo A Lima and Benjamin P Weiss. Obtaining vector magnetic field maps from single-component measurements of geological samples. *J. Geophys. Res. [Solid Earth]*, 114(B6), 2009.

[51] Kento Sasaki, Yasuaki Monnai, Soya Saijo, Ryushiro Fujita, Hideyuki Watanabe, Junko Ishi-Hayase, Kohei M Itoh, and Eisuke Abe. Broadband, large-area microwave antenna for optically detected magnetic resonance of nitrogen-vacancy centers in diamond. *Rev. Sci. Instrum.*, 87(5):053904, May 2016.

[52] A C Gossard, A M Portis, M Rubinstein, and R H Lindquist. Ferromagnetic nuclear resonance of Single-Domain cobalt particles. *Phys. Rev.*, 138(5A):A1415–A1421, May 1965.

[53] E P Wohlfarth. Magnetic properties of single domain ferromagnetic particles. *J. Magn. Magn. Mater.*, 39(1):39–44, November 1983.

[54] F Dolde, H Fedder, M W Doherty, T Nöbauer, F Rempp, G Balasubramanian, T Wolf, F Reinhard, L C L Hollenberg, F Jelezko, and J Wrachtrup. Electric-field sensing using single diamond spins. *Nat. Phys.*, 7(6):459–463, April 2011.

[55] T Mittiga, S Hsieh, C Zu, B Kobrin, F Machado, P Bhattacharyya, N Z Rui, A Jarmola, S Choi, D Budker, and N Y Yao. Imaging the local charge environment of nitrogen-vacancy centers in diamond. *Phys. Rev. Lett.*, 121(24):246402, December 2018.

[56] D A Broadway, B C Johnson, M S J Barson, S E Lillie, N Dontschuk, D J McCloskey, A Tsai, T Teraji, D A Simpson, A Stacey, J C McCallum, J E Bradby, M W Doherty, L C L Hollenberg, and J-P Tetienne. Microscopic imaging of the stress tensor in diamond using in situ quantum sensors. *Nano Lett.*, 19(7):4543–4550, July 2019.

[57] L M Pham, D Le Sage, P L Stanwix, T K Yeung, D Glenn, A Trifonov, P Cappellaro, P R Hemmer, M D Lukin, H Park, A Yacoby, and R L Walsworth. Magnetic field imaging with nitrogen-vacancy ensembles. *New J. Phys.*, 13(4):045021, April 2011.

[58] Julia M McCoey, Robert W de Gille, Babak Nasr, Jean-Philippe Tetienne, Liam T Hall, David A Simpson, and Lloyd C L Hollenberg. Rapid, high-resolution magnetic microscopy of single magnetic microbeads. *Small*, 15(18):e1805159, May 2019.

[59] Adam M Wojciechowski, Mürsel Karadas, Alexander Huck, Christian Osterkamp, Steffen Jankuhn, Jan Meijer, Fedor Jelezko, and Ulrik L Andersen. Contributed review: Camera-limits for wide-field magnetic resonance imaging with a nitrogen-vacancy spin sensor. *Rev. Sci. Instrum.*, 89(3):031501, March 2018.

[60] Ilja Fescenko, Abdelghani Laraoui, Janis Smits, Nazanin Mosavian, Pauli Kehayias, Jong Seto, Lykourgos Bougas, Andrey Jarmola, and Victor M Acosta. Diamond magnetic microscopy of malarial hemozoin nanocrystals. *Phys Rev Appl*, 11(3), March 2019.

[61] P Kehayias, M J Turner, R Trubko, J M Schloss, C A Hart, M Wesson, D R Glenn, and R L Walsworth. Imaging crystal stress in diamond using ensembles of nitrogen-vacancy centers. *Phys. Rev. B Condens. Matter*, 100(17):174103, November 2019.

[62] A A Travers and J M T Thompson. An introduction to the mechanics of DNA. *Philos. Trans. A Math. Phys. Eng. Sci.*, 362(1820):1265–1279, July 2004.

[63] Stephanie Geggier and Alexander Vologodskii. Sequence dependence of DNA bending rigidity. *Proc. Natl. Acad. Sci. U. S. A.*, 107(35):15421–15426, August 2010.

[64] Aleksander V Drozdetski, Abhishek Mukhopadhyay, and Alexey V Onufriev. Strongly bent Double-Stranded DNA: Reconciling theory and experiment. *Frontiers in Physics*, 7, 2019.

[65] B Simpson, C Tupper, and N M Al Aboud. Genetics, DNA packaging. `https://europepmc.org/article/nbk/nbk534207`. Accessed: 2023-6-22.

[66] Mikael P Backlund, Pauli Kehayias, and Ronald L Walsworth. Diamond-Based magnetic imaging with fourier optical processing. *Phys. Rev. Appl.*, 8(5):054003, November 2017.

Appendix A

DIAMOND FLOW CHAMBER CONSTRUCTION AND TPM ASSAY WITH TURBOBEADS ON DIAMOND PROTOCOL

All DNA experiments in this work rely on the TPM assay. Here is the protocol with notes with the highest sucess rate for TPM events. The protocol was adapted from Ref. [39] with modifications based on concentration testing and direct communication with Dylan Collette, a previous postdoc in the Finzi group at Emory. The diamonds used in this work are approximately 100 µm thick and thus are extremely sensitive. Care must be used so that the diamonds don't fly away and get lost.

Flow chamber construction:

1. **Clean diamond**

    - Place diamond on paper Kimwipe
    - Scrub diamond with acetone and q-tip
    - Sonicate diamond in 1% volume diluted Hellmanex cuvette cleaner in milQ for 30 mins
    - Sonicate diamond in milQ for 30 mins

2. **Mount diamond on coverslip**

    - Carefully place diamond on cleaned coverslip (see Figure A.1(a))
    - Check using 10X optical microscope that diamond is face up. The CVD growth artifacts are visible on the NV side, while striated polishing marks are on the back side. If upside down, push diamond to edge of coverslip and tip over to flip rightside up.
    - Slice 2x (0.5 mm x 0.3 cm) tape pieces, use to secure diamond to coverslip (see Figure A.1(b))

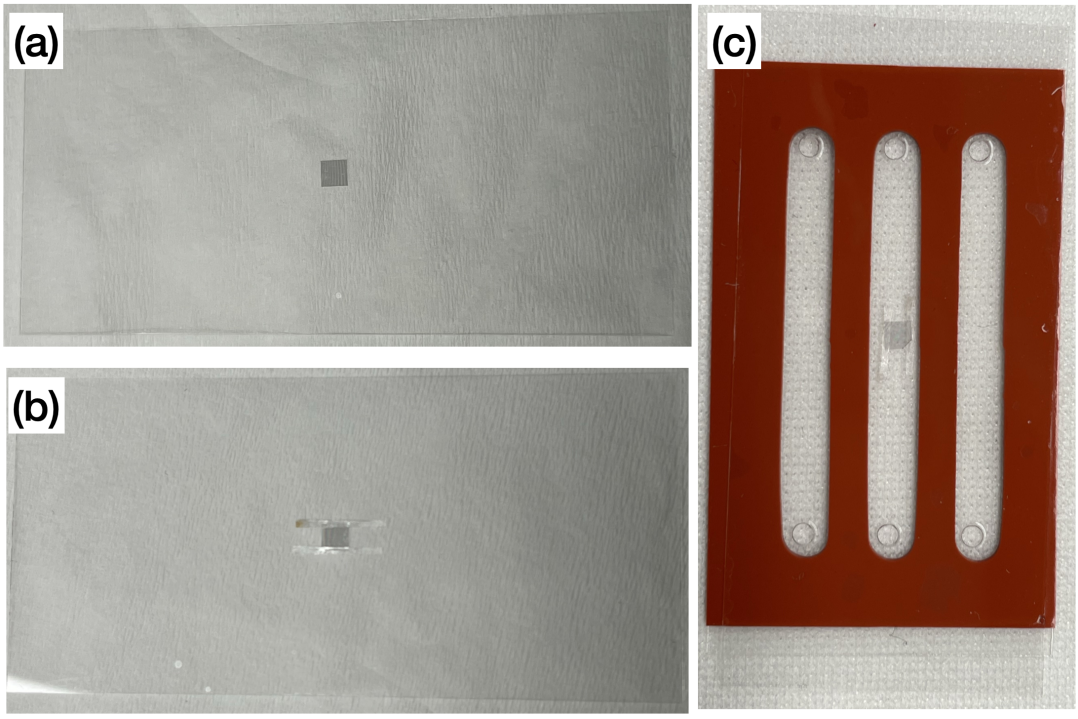

Figure A.1: **Diamond flow chamber construction.** (a) Diamond sensor on coverglass. (b) Diamond sensor with two pieces of tape securing it to coverglass. (c) Diamond sensor taped to coverglass with perfusion chamber adhered to coverglass.

- Place Grace Bio Labs CoverWell perfusion chamber (622103) over diamond, press gently to seal removing any air pockets between chamber and coverslip (chamber volume approx 100 uL) (see Figure A.1(c))

3. **TPM construction protocol**

- In empty chamber, flow 200 µL 1X phosphate buffered saline (PBS) (Millipore-Sigma 806552-1L)
- Dilute anti-dig in PBS to 100 µg/mL
- Centrifuge anti-dig solution for 5 mins at 10,000 rpm
- Flow 90 uL into cell. Pipette gently and uniformly to fill cell (use folded paper Kimwipe at other side to draw fluid and exchange liquids in chamber)
- Start sonicating 30 pM Turbobead solution
- Wait 60 mins
- Flush cell with 200 µL PBS
- Flush cell with casein buffer (100 µL) (WestEz Casein buffer)
- Wait 30 mins
- Flush cell with 200 µL DNA buffer (λ-buffer from [39])
- Flow 100 uL of DNA buffer
- Wait 15 mins
- Flush cell with 200 µL DNA buffer
- Flow beads (10 µL, using P20 with 10 µL pipette tip). While still sonicating beads, use small pipetter to draw bead solution. Pipette "up and down" approximately 10 times before introducing beads into chamber. The beads clump very quickly!
- Wait 15 mins. This is a crucial wait as long wait times here enable more clumping of the TBs.
- Flush cell with DNA buffer after wait (800 µL, 4 x 200 µL)

- Apply caps to Grace Bio Labs flow chamber

Flow chambers typically last up to about a week. The limit is bubbles forming from air leaking slowly out of the chamber.